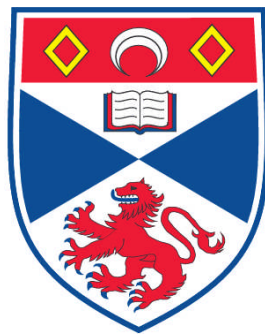


THEORETICAL MAGNETIC FLUX EMERGENCE

David MacTaggart

**A Thesis Submitted for the Degree of PhD
at the
University of St. Andrews**



2011

**Full metadata for this item is available in
Research@StAndrews:FullText
at:**

<https://research-repository.st-andrews.ac.uk/>

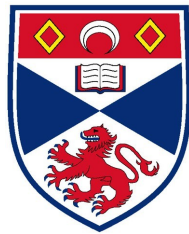
Please use this identifier to cite or link to this item:

<http://hdl.handle.net/10023/1692>

This item is protected by original copyright

**This item is licensed under a
Creative Commons License**

Theoretical Magnetic Flux Emergence



David MacTaggart
School of Mathematics and Statistics
University of St Andrews

A thesis submitted for the degree of

Doctor of Philosophy

July 2010

Declaration

I, David MacTaggart, hereby certify that this thesis, which is approximately 30,000 words in length, has been written by me, that it is the record of work carried out by me and that it has not been submitted in any previous application for a higher degree.

Candidate: David MacTaggart Signature:..... Date:.....

I was admitted as a research student in September 2007 and as a candidate for the degree of Doctor of Philosophy in September 2008; the higher study for which this is a record was carried out in the University of St Andrews between 2007 and 2010.

Candidate: David MacTaggart Signature:..... Date:.....

I hereby certify that the candidate has fulfilled the conditions of the Resolution and Regulations appropriate for the degree of Doctor of Philosophy in the University of St Andrews and that the candidate is qualified to submit this thesis in application for that degree.

Supervisor: Alan Hood Signature:..... Date:.....

In submitting this thesis to the University of St Andrews I understand that I am giving permission for it to be made available for use in accordance with the regulations of the University Library for the time being in force, subject to any copyright vested in the work not being affected thereby. I also understand that the title and abstract will be published, and that a copy of the work may be made and supplied to any bona fide library or research worker, that my thesis will be electronically accessible for personal or research use, and that the library has the right to migrate my thesis into new electronic forms as required to ensure continued access to the thesis. I have obtained any third-party copyright permissions that may be required in order to allow such access and migration.

Name: David MacTaggart Signature:..... Date:.....

The following is an agreed request by candidate and supervisor regarding the electronic publication of this thesis:

Access to Printed copy and electronic publication of thesis through the University of St Andrews.

Candidate:..... Supervisor:..... Date:.....

Acknowledgements

Many people have helped shape the course of my PhD. First and foremost, I must thank my supervisor, Professor Alan Hood. It has been my privilege to work with one of the leading authorities on solar MHD.

Eleven o'clock in St Andrews means coffee time and this has been the setting for many fruitful conversations. Particular thanks goes to Professors Thomas Neukirch and Bernie Roberts, and Doctors Stéphane Réginer, Tibor Török and Vasilis Archontis.

I thank STFC for funding my studies. I also thank the Solaire Network for organizing various schools and conferences, from which I've benefited greatly.

Finally, I thank my family for their constant love and support. I dedicate this thesis to my brother and best friend, Michael.

Abstract

Magnetic flux emergence is the subject of how magnetic fields from the solar interior can rise and expand into the atmosphere to produce active regions. It is the link that joins dynamics in the convection zone with dynamics in the atmosphere. In this thesis, we study many aspects of magnetic flux emergence through mathematical modelling and computer simulations. Our primary aim is to understand the key physical processes that lie behind emergence.

The first chapter introduces flux emergence and the theoretical framework, magnetohydrodynamics (MHD), that describes it. In the second chapter, we discuss the numerical techniques used to solve the highly non-linear problems that arise from flux emergence. The third chapter summarizes the current literature. In the fourth chapter, we consider how changing the geometry and parameter values of the initial magnetic field can affect the dynamic evolution of the emerging magnetic field. For an initial toroidal magnetic field, it is found that its axis can emerge to the corona if the tube's initial field strength is large enough. The fifth chapter describes how flux emergence models can produce large-scale solar eruptions. A 2.5D model of the breakout model, using only dynamic flux emergence, fails to produce any large-scale eruptions. A 3D model of toroidal emergence with an overlying magnetic field does, however, produce multiple large-scale eruptions and the form of these is related to the breakout model. The sixth chapter is concerned with signatures of flux emergence and how to identify emerging twisted magnetic structures correctly. Here, a flux emergence model produces signatures found in observations. The signatures from the model, however, have different underlying physical

mechanisms to the original interpretations of the observations. The thesis concludes with some final thoughts on current trends in theoretical magnetic flux emergence and possible future directions.

Contents

1	Basics of flux emergence	1
1.1	Introduction	1
1.2	Magnetohydrodynamics	3
1.2.1	Basic equations	3
1.2.2	Is MHD a suitable theory for flux emergence?	4
1.3	Magnetic buoyancy	6
1.4	Summary	12
2	Numerical techniques	14
2.1	Introduction	14
2.2	The Lagrangian step	16
2.2.1	1D predictor-corrector step	17
2.2.1.1	Predictor step	18
2.2.1.2	Corrector step	19
2.2.2	Shock viscosity	20
2.3	The remap step	22
2.3.1	The density remap	23
2.3.2	The specific energy density remap	24
2.3.3	The velocity remap	26
2.3.4	Flux limiters	26
2.4	The LARE steps	27
2.4.1	The LARE Lagrangian step	28
2.4.2	The LARE remap step	30
2.5	The Riemann problem	31
2.6	Summary	35

3	Literature review	36
3.1	Review	36
3.1.1	2D and 2.5D simulations	36
3.1.2	3D simulations	41
4	Toroidal flux emergence	50
4.1	Introduction	50
4.2	Initial equilibrium	51
4.2.1	Hydrostatic atmosphere	51
4.2.2	Initial magnetic field	52
4.2.2.1	Cylindrical flux tube	53
4.3	Toroidal flux tube	54
4.4	Parameter study	57
4.4.1	Varying B_0 with fixed α : general dynamics	57
4.4.2	$B_0 = 5, 7$ comparison	60
4.4.3	Plasma drainage	68
4.4.4	Varying α with fixed B_0	72
4.4.4.1	Rise and emergence	72
4.4.4.2	Sunspot drift	75
4.5	Summary	76
5	Coronal eruptions	79
5.1	Introduction	79
5.2	Modelling magnetic breakout with flux emergence	82
5.2.1	Quadrupolar initial condition	83
5.2.1.1	Photospheric conditions	83
5.2.1.2	Current densities	86
5.2.1.3	Three tubes	88
5.2.2	Breakout summary	93
5.3	Eruptions from toroidal flux emergence	95
5.3.1	3D model	95
5.3.2	Eruption mechanisms	96
5.4	Summary	103

6 Signatures of flux emergence	105
6.1 Introduction	105
6.2 Model setup	106
6.3 First signature: ‘Sliding doors’	107
6.4 Second signature: Horizontal vector directions	111
6.5 Other signatures	112
6.5.1 Unsigned flux	112
6.5.2 Shear flows	113
6.6 Summary	115
7 Final thoughts	117
7.1 Trends and fashions	117
7.2 Future directions	119
References	128

List of Figures

1.1	A schematic showing the upper layers of the Sun. Approximate heights are included to convey the scale of the region. The solar exterior begins at 0 km. Temperature and density magnitudes are given for the photosphere and the corona to indicate the vast range of scales. Numerical values are taken from Carroll & Ostlie (1996) .	2
2.1	The LARE code split into its component parts.	16
2.2	The staggered grid.	17
2.3	The change in mass of a cell after a timestep.	23
2.4	The energy change in mass coordinates.	25
2.5	The 3D staggered grid in LARE.	28
2.6	The profiles for u and ρ at $t = 0.0188$. Shock viscosity and flux limiters have been used in the construction of these solutions. . .	33
2.7	The profiles for u and ρ at the contact discontinuity and the shock.	34
2.8	The closeup profiles for u and ρ with no shock viscosity.	34
4.1	The model temperature and associated hydrostatic density as a function of height. Key: temperature (solid), density (dash). . . .	52
4.2	The height-time profiles for axes with different B_0 traced in the $y = 0$ plane. Key: $B_0 = 1$ (solid), $B_0 = 3$ (dot), $B_0 = 5$ (dash), $B_0 = 7$ (dot-dash) and $B_0 = 9$ (triple dot-dash).	58
4.3	The height-time profiles in the solar interior rescaled to time $\bar{t} = tB_0$. Key: $B_0 = 1$ (solid), $B_0 = 3$ (dot), $B_0 = 5$ (dash), $B_0 = 7$ (dot-dash) and $B_0 = 9$ (triple dot-dash).	58

LIST OF FIGURES

4.4	This diagram illustrates some of the main dynamical features of the emergence of a toroidal flux tube. The outline represents the outermost field line of the emerging arcade. See the text for more details.	59
4.5	The density deficit at the tube axis (in the $y = 0$ plane) as a fraction of the initial unsigned density deficit against height. Time moves from left to right. Key: $B_0 = 5$ (dash), $B_0 = 7$ (solid). . . .	61
4.6	The vertical velocity, u_z , (in the $y = 0$ plane) as a function of height. u_{ph} is the photospheric velocity scale and H_{ph} is the photospheric scale height. Time moves from left to right. Key: $B_0 = 5$ (dash), $B_0 = 7$ (solid).	61
4.7	The ‘square well’ profile for the deficit in the total pressure. This deficit exists for a finite range of heights (see text) and plasma draining from above flows into it. This figure is for the $B_0 = 7$ case at $t = 100$ and $(y, z) = (0, 3)$	63
4.8	The $B_0 = 5$ case at $t = 100$. The original tube axis is represented by a red field line. Some surrounding field lines are traced in grey. A simulation magnetogram is placed at the bottom of the photosphere ($z=0$) and shows B_z	63
4.9	The $B_0 = 7$ case at $t = 100$. The original tube axis is represented by a red field line. Some surrounding field lines are traced in grey. A simulation magnetogram is placed at the bottom of the photosphere ($z=0$) and shows B_z	64
4.10	Shearing profiles at $t = 100$ and $(y, z) = (0, 3)$ for $B_0 = 5$ (dash) and $B_0 = 7$ (solid).	64
4.11	Inflow profiles at $t = 100$ and $(y, z) = (0, 3)$ for $B_0 = 5$ (dash) and $B_0 = 7$ (solid). There are clear inflow profiles for both cases. However, when the flows meet in the centre of the pressure deficit zone, they produce more complex behaviour.	65

LIST OF FIGURES

4.12	The $B_0 = 5$ case at $t = 100$. The red field line represents the original tube axis. The green field line represents the axis of a new flux rope. The surrounding field line structure at the new axis is demonstrated by some field lines traced in grey. The original axis is pinned down in the photosphere whereas the new rope is at the base of the corona. The simulation magnetogram of B_z is at $z = 0$.	66
4.13	The $B_0 = 7$ case at $t = 100$. The red field line represents the original tube axis. The green field line represents the axis of a new flux rope. The surrounding field line structure at the new axis is demonstrated by some field lines traced in grey. Reconnection occurs where the grey field lines cross. An upward jet from this pushes the original axis higher. The simulation magnetogram of B_z is at $z = 0$.	67
4.14	The evolution of $\Phi_h(y = 0, t)/\Phi_h(y = 0, t = 0) \times 100\%$ for $B_0 = 5$ (dash) and $B_0 = 7$ (solid) in the atmosphere ($z > 0$).	68
4.15	The evolution of $\Phi_h(y = 0, t)/\Phi_h(y = 0, t = 0) \times 100\%$ for $B_0 = 5$ (dash) and $B_0 = 7$ (solid) in the interior ($z < 0$).	69
4.16	The vertical velocity profile through a cut in one of the legs of the toroidal tube at $t = 40$ and $(x, y) = (0, -13)$. The vertical velocity in the cut is positive since the tube is buoyantly rising.	70
4.17	The vertical velocity profile through a cut in one of the legs of the toroidal tube at $t = 50$ and $(x, y) = (0, -13)$. The sign of the velocity in the cut has now changed since plasma drains down the leg, creating a downflow.	70
4.18	The geometry of the cylinder model with the buoyancy profile $n \exp(-y^2/\lambda^2) - (n - 1)$ exhibits a toroidal-like shape. This snapshot is at $t = 86$ and shows an isosurface of $ \mathbf{B} = 0.5$ in blue and a field line in red indicating the axis.	71
4.19	The axis height-time profiles for the cases $\alpha = 0.2$ (solid), $\alpha = 0.3$ (dot) and $\alpha = 0.4$ (dash) in the solar interior.	73
4.20	The height-time profiles of the tops of the magnetic fields of tubes with different twists. Key: $\alpha = 0.2$ (solid), $\alpha = 0.4$ (dash).	74

LIST OF FIGURES

4.21	The evolution of the vertical flux through $z = 10$, Φ_v , for tubes with different twists. Key: $\alpha = 0.2$ (solid), $\alpha = 0.4$ (dash).	74
4.22	The y -separation in time of the maximum and minimum B_z at the base of the photosphere ($z=0$). The higher the twist, the slower the separation. Key: $\alpha = 0.2$ (solid), $\alpha = 0.3$ (dot-dash), $\alpha = 0.4$ (dash).	75
5.1	Meridional projections of magnetic field lines throughout the magnetic breakout eruption process at six different times. (a) shows the initial quadrupolar structure. (b) and (c) show the expanding inner region due to increased magnetic pressure from shearing at the photosphere. The null point is deformed into a current sheet and external reconnection takes place. (d) and (e) show continued expansion and the pinching off of a flux rope through internal reconnection. (f) shows the outer expansion of the new flux rope. This diagram is from Lynch <i>et al.</i> (2008) . Spatial units are in solar radii.	80
5.2	The resulting quadrupole from experiment (i) where the tubes have an initial lateral separation of 20. The colourmap shows $ \mathbf{B} $ and some field lines are traced in black.	84
5.3	The solid line shows $(\mathbf{j} \times \mathbf{B})_x$ and the dashed line, $\partial p/\partial x$. Both cuts are taken at the photosphere at time $t = 275$ for experiment (i).	85
5.4	The horizontal speed at the photosphere at $t = 275$ for experiment (i).	86
5.5	The solid line shows $(\mathbf{j} \times \mathbf{B})_x$ and the dashed line, $\partial p/\partial x$. Both cuts are taken at the photosphere at time $t = 338$ for experiment (iv).	87
5.6	The horizontal speed at the photosphere at $t = 338$ for experiment (iv).	88
5.7	The variation of current density with height for experiment (ii) at time $t = 278$. The cut is taken through $x = 200$	89
5.8	The logarithmic variation of $ \mathbf{j} / \mathbf{B} $ with height for experiment (ii) at time $t = 278$. The cut is taken through $x = 200$	90

LIST OF FIGURES

5.9	The quadrupolar configuration with the middle tube at the photosphere at time $t = 300$ for experiment (iv). The colourmap is of $ \mathbf{B} $	91
5.10	The horizontal speed profile at the photosphere at $t = 300$	92
5.11	The magnetic field of experiment (iv) at time $t = 450$. The colourmap is of $ \mathbf{B} $	92
5.12	The horizontal speed profile at the photosphere at $t = 450$	93
5.13	The solid curve shows the vertical velocity through the central arcade at $t = 360$. The dashed curve shows the same cut but at $t = 450$	94
5.14	As the arcade of the emerging tube expands into the magnetized corona, the continued weakening of the overlying restraining field results in faster reconnection.	98
5.15	The field line structure of the corona after external reconnection. Red and green coronal lines are traced from opposite sides of the box, $x = -50$ and $x = 50$, respectively, at $z = 22$ and $t = 70$. A simulation magnetogram shows B_z at $z = 0$	99
5.16	The field line configuration just before the eruption of the second rope. Coronal field lines (cyan) are traced from the sides of the box (along the y -axis) at $z = 40$. The red field line is the axis of the newly formed flux rope. Some field lines surrounding this are traced in green. A simulation magnetogram is displayed at $z = 0$	100
5.17	The height-time profiles for the two eruptions of the simulation. The curve for the first eruption is solid and the second is dashed.	101
5.18	The second flux tube eruption of the simulation at $t = 132$. The colour map shows $\log \rho$ in the $y = 0$ plane with field line arrows to show the direction (but not the magnitude) of the magnetic field. Dense plasma can clearly be seen to be carried upwards into the corona with the erupting flux tube.	101
5.19	The vertical forces carrying the flux rope upwards at $t = 130$. The cut is taken at $(x, y) = (0, 0)$. Key: All forces (solid), $(\mathbf{j} \times \mathbf{B})_z$ (dash), $-\partial p / \partial z$ (dot-dash).	102

LIST OF FIGURES

6.1	The initial condition. The magnetogram of B_z at the base of the photosphere shows the opposite polarities of the arcade (blue - negative, red - positive and green - horizontal field). Some of the arcade field lines are traced in purple from the base of the photosphere. An isosurface ($ \mathbf{B} = 3$) shows the initial location of the twisted flux rope in the solar interior.	108
6.2	Slices in the $(x, 0, z)$ plane. Dashed contours and colours identify regions of strong (relative) B_z . (B_x, B_z) arrows and a black dot indicate the position of the flux tube axis. Each slice represents a different time: (a) $t = 38$, (b) $t = 48$, (c) $t = 58$ and (d) $t = 78$. . .	109
6.3	Time-slice image showing the ‘sliding doors’ effect. The slices from the simulation are taken at $y = 0$ and from $x = -20$ to $x = 20$. The time difference between the slices is 2 in non-dimensional units. Colours are as indicated in Figure 1.	110
6.4	Time evolution of the horizontal field vector against the PIL for two locations along the tube length. Key: $y = 0$ (solid), $y = 10$ (dash)	111
6.5	The angles between the horizontal magnetic fields and the PIL. Taken from O1, Figures (d1)-(d6).	112
6.6	The evolution of the unsigned vertical flux from negative polarities for the duration of the simulation.	113
6.7	Shear flows at the PIL. (a) displays a slice, showing u_y at $t = 1050$ s, taken at the base of the photosphere in the model. The arrows are horizontal velocity vectors. The colour bar shows non-dimensional speed. (b) shows the shear profiles of a horizontal cut across the PIL at three different times. Key: $t = 900$ s (solid), $t = 1225$ s (single dash) and $t = 2200$ s (dot dash).	114

Chapter 1

Basics of flux emergence

1.1 Introduction

Solar atmospheric activity is driven by the emergence of magnetic flux from within the Sun's interior. The concentrations of strong magnetic field that appear on the surface occur in characteristic time-dependent configurations, known as *active regions*. Such regions can vary in complexity but are generally *bipolar*, with two fairly distinct areas of opposite polarity (Schrijver & Zwaan (2000)). These can combine to form complex active regions and nests. The bipolar active region, however, is the basic building block and holds the key to understanding more complex regions.

The lifetime of active regions can vary from several hours to several months, depending on the size of the region and the strength of the magnetic flux. The emergence process takes only a small fraction of the total lifetime of an active region. It is during this time, however, that a collection of physical mechanisms combine to create an active region. An understanding of how these processes compete or cooperate in the emergence of active regions is the focus of this thesis. The problem has occupied theoreticians for the past sixty years. However, only recently, with the advent of massively parallel computers, has it been possible to study the three dimensional (3D) nature of emergence in detail.

It is currently believed that magnetic flux tubes ¹ form at the tachocline (a

¹In this thesis, magnetic flux tubes and magnetic flux ropes are both twisted magnetic structures. Generally, tubes refer to those in the interior and ropes to those in the atmosphere.

shear layer at the base of the convection zone) and that these rise buoyantly through the convection zone. At the top of the convection zone the tubes encounter the photosphere and their buoyant rise ends. Here, an instability then allows the magnetic flux from the tubes to penetrate far into the atmosphere, producing active regions. Figure 1.1 displays a diagram representing the layers of the Sun through which the flux tubes rise. The idea of buoyant magnetic flux tubes has existed for some time (Parker (1955), Jensen (1955)). Cowling (1946) envisaged a similar theory where flux tubes run as girdles around the Sun and suggested that loops are carried upwards by convection to emerge as sunspot pairs. We shall discuss the theoretical mechanisms of magnetic flux emergence in much more detail throughout the course of the thesis. To do this, however, we require a theoretical framework that will describe the behaviour of emerging flux on appropriate scales.

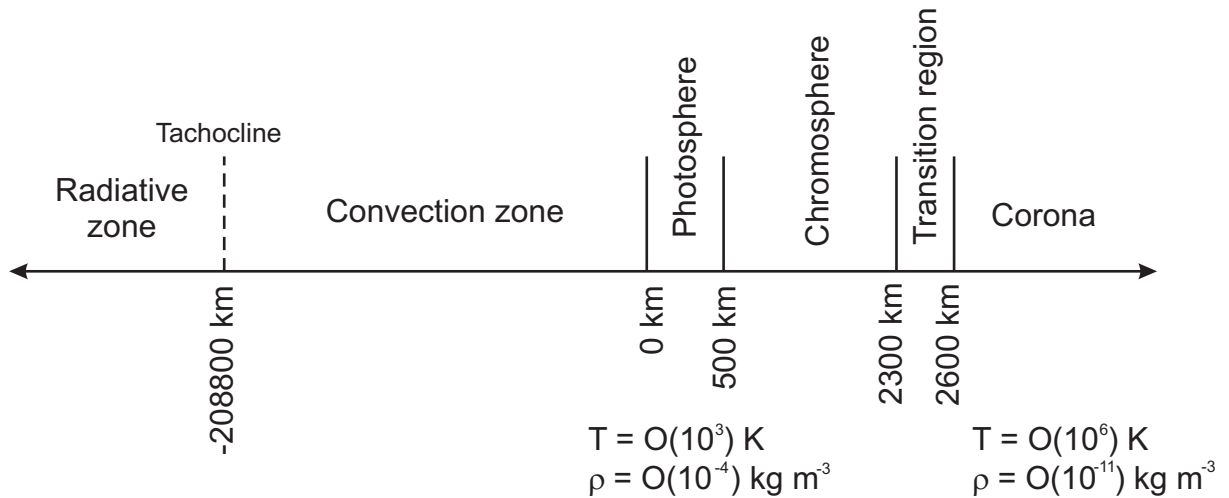


Figure 1.1: A schematic showing the upper layers of the Sun. Approximate heights are included to convey the scale of the region. The solar exterior begins at 0 km. Temperature and density magnitudes are given for the photosphere and the corona to indicate the vast range of scales. Numerical values are taken from Carroll & Ostlie (1996).

1.2 Magnetohydrodynamics

1.2.1 Basic equations

As indicated by Figure 1.1, flux emergence operates on a huge range of scales. In this thesis, we are only interested in the region from the top of the convection zone to the low corona. Even this truncated atmosphere, however, presents us with a daunting range of variables. The typical lengths of emerging active regions are of the order of hundreds of thousands of kilometers and can evolve over periods of days. This suggests a macroscopic, rather than a microscopic, description of the plasma. A continuum (fluid) description of a plasma is provided by *magnetohydrodynamics* (MHD). The conducting medium is treated as a fluid that is threaded by magnetic field lines. This field may be externally applied, produced by current in the fluid or a combination of both. The basic equations of MHD are

$$\frac{\partial \rho}{\partial t} + \nabla \cdot (\rho \mathbf{u}) = 0, \quad (1.1)$$

$$\rho \left(\frac{\partial \mathbf{u}}{\partial t} + (\mathbf{u} \cdot \nabla) \mathbf{u} \right) = -\nabla p + \mathbf{j} \times \mathbf{B} + \nabla \cdot \mathbf{T} + \rho \mathbf{g}, \quad (1.2)$$

$$\rho \left(\frac{\partial \varepsilon}{\partial t} + (\mathbf{u} \cdot \nabla) \varepsilon \right) = -p \nabla \cdot \mathbf{u} + \eta j^2 + Q_{\text{visc}}, \quad (1.3)$$

$$\frac{\partial \mathbf{B}}{\partial t} = \nabla \times (\mathbf{u} \times \mathbf{B}) + \eta \nabla^2 \mathbf{B}, \quad (1.4)$$

$$\nabla \cdot \mathbf{B} = 0, \quad (1.5)$$

$$p = \frac{1}{\tilde{\mu}} R \rho T, \quad \varepsilon = \frac{p}{(\gamma - 1)\rho}, \quad (1.6)$$

where ρ is the density, \mathbf{u} is the velocity, p is the pressure, \mathbf{B} is the magnetic induction (generally referred to as the magnetic field), $\mathbf{j} = \mu_0^{-1} \nabla \times \mathbf{B}$ is the current density (with μ_0 being the magnetic permeability of free space), \mathbf{g} is gravity, η is the (constant) resistivity and T is the temperature. γ is the ratio of specific

heats and $\tilde{\mu}$ is the mean molecular weight ($\tilde{\mu} = 0.5$ for a fully ionized plasma, $\tilde{\mu} = 1$ for a neutral hydrogen gas), $R = k_B/m_p$ and is a constant and ε is the specific internal energy density. The viscosity tensor and viscous contribution to the energy equation are, respectively,

$$\mathbf{T} = \mu \left(\nabla \mathbf{u} + \nabla \mathbf{u}^T - \frac{2}{3} \mathbf{I} \nabla \cdot \mathbf{u} \right), \quad Q_{\text{visc}} = \mathbf{T} : \frac{1}{2} (\nabla \mathbf{u} + \nabla \mathbf{u}^T),$$

where μ is the viscosity and \mathbf{I} is the identity tensor. For a magnetized plasma, one should consider the full Braginskii viscosity (Braginskii (1965)), with parallel and perpendicular components. We only consider the unmagnetized fluid viscosity since, in the work of this thesis, it is used for numerical reasons (e.g. to aid relaxation) rather than physical ones.

The above equations can be derived by taking moments of the kinetic Boltzmann equation and making certain closure assumptions (Boyd & Sanderson (1969), Benz (1993)). We refer to these as the *basic* MHD equations to signify that many extensions to these equations exist. Such extensions include extra terms in the induction equation (1.4). However, these are not directly important for large-scale flux emergence. One that is important for flux emergence is the extension of the adiabatic energy equation (1.3) and the equation of state (1.6) to include effects such as thermal conduction. This, and others, will be discussed later in the thesis. For the moment, however, equations (1.1) to (1.6) will be used to model the basic interactions of the plasma and magnetic field in flux emergence. The induction equation (1.4) is written in resistive form to include the effects of reconnection. If $\eta = 0$, the above equations represent ideal MHD.

1.2.2 Is MHD a suitable theory for flux emergence?

This one-fluid description will only be valid provided the plasma is collision dominated (Dendy (1993)). One condition for collision dominance is that the distribution functions of the particle species are locally Maxwellian. If this is to hold, the MHD time scale τ_{MHD} , by which we mean the minimum time for significant change in the most rapidly fluctuating of the macroscopic variables, must be greater than the collision time τ_c . The ion and electron collision times, τ_i and τ_e , are defined as the times for significant particle deflection. i.e. momentum change.

1.2 Magnetohydrodynamics

For species temperatures $T_i \approx T_e$, it follows that the collision time for each species is inversely proportional to its thermal speed, hence $\tau_i \approx (m_i/m_e)^{1/2}\tau_e$ (Boyd & Sanderson (2003)). Therefore, both ions and electrons will be in local equilibrium provided

$$\tau_i \ll \tau_{\text{MHD}}.$$

However, one-fluid MHD assumes a single temperature, requiring an even stronger collisionality condition. Temperature equilibrium depends on energy exchange between ions and electrons and as the energy exchange per collision is proportional to m_e/m_i , it follows that initially different temperatures will be approximately the same after a time $(m_i/m_e)\tau_e$. This strengthens the collisionality condition to

$$\tau_i \ll (m_e/m_i)^{1/2}\tau_{\text{MHD}}. \quad (1.7)$$

A constraint on the length scales is that the mean free paths of the ions and electrons have to be far smaller than the macroscopic MHD scale L_{MHD} . Since the mean free path λ_c for ions and electrons is the same order of magnitude, the constraint is

$$\lambda_c \ll L_{\text{MHD}}. \quad (1.8)$$

Another important constraint is that large-scale flows are non-relativistic. This follows from the neglect of the displacement current from Maxwell's equations in the derivation of the MHD equations (Boyd & Sanderson (2003)). Therefore, for large-scale flows,

$$L_{\text{MHD}}/\tau_{\text{MHD}} \ll c, \quad (1.9)$$

where c is the speed of light.

For the layers of the solar atmosphere that we are concerned with, the character of the plasma changes drastically. From the upper convection zone to the photosphere, conditions (1.7), (1.8) and (1.9) are satisfied and the large-scale plasma can be modelled using MHD. In the corona, however, we run into difficulties. Based on typical coronal values (e.g. Boyd & Sanderson (2003)), condition (1.9) is satisfied and condition (1.7) requires τ_{MHD} to be of the order of a few

seconds, a resolution that is perfectly acceptable for large-scale flux emergence. The mean free path in the low corona, however, is of the order of 10^5 to 10^6 m, meaning that constraint (1.8) is *not* satisfied for flux emergence on scales we are concerned with ($O(1)$ Mm). This is because the corona is collisionless as opposed to collisional. Does this mean that MHD cannot be applied to this region? For the past sixty years, the corona has been modelled using MHD and there is a large amount of empirical evidence to suggest that the theory is successful in describing macroscopic plasma behaviour in this region. A reconciliation of collisional MHD to the collisionless corona can be made by relaxing the isotropic nature of the theory. Freidberg (1987) proposed a MHD model that takes account of variables parallel and perpendicular to the magnetic field. A consequence of this is the reversal of constraints (1.7) and (1.8) to

$$\tau_i \gg (m_e/m_i)^{1/2} \tau_{\text{MHD}}, \quad \lambda_c \gg L_{\text{MHD}},$$

respectively, which are the constraints for a collisionless plasma. The theory is called *collisionless MHD* and it can be shown that its predictions compare well with those of ideal MHD (Freidberg (1987), Boyd & Sanderson (2003)).

Although this is not a proof for the ‘correctness’ of using MHD in the corona, the similarities in the results of the collisional and collisionless versions of the theory and the body of empirical evidence in favour of MHD suggest that it is the correct way to approach modelling flux emergence in the corona. In addition to this, MHD is well behaved mathematically. Ideal MHD can be written as a set of physical conservation laws (mass, momentum, energy and magnetic flux) and with appropriate boundary conditions, problems in MHD are well-posed. This property is more elusive in complex multi-fluid theories (e.g. Fitt (1996)).

1.3 Magnetic buoyancy

As mentioned previously, it is widely believed that magnetic flux, in the form of flux tubes, rises through the solar interior and emerges at the surface to form active regions. The mechanism by which this happens is a two-stage process, with both stages relating to buoyancy. Proceeding with MHD as our theoretical

framework, we can now model these stages. The first concerns the basic rise of isolated magnetic flux tubes in the convection zone. Consider an isolated horizontal flux tube in pressure equilibrium with its non-magnetic surroundings; thus

$$p_i + \frac{B^2}{2\mu_0} = p_e,$$

where p_i and p_e are the internal and external pressures, respectively, and B is the magnetic field. In this section, for simplicity, we will take the flux tubes to have straight, untwisted magnetic fields. Assuming the tube is in thermal equilibrium with its surroundings it follows from the equation of state for an ideal gas (equation (1.6)) that, since $p_i < p_e$, then $\rho_i < \rho_e$ and so the tube is less dense than its surroundings and will rise under the influence of gravity.

The second stage is concerned with the emergence of magnetic flux into the atmosphere. Since the photosphere is stable to buoyancy, flux tubes cannot continue to rise as they have done in the convection zone. Emergence through the photosphere is achieved via the *magnetic buoyancy instability*, a form of the magnetic Rayleigh-Taylor instability. There have been many studies of this instability, e.g. [Newcomb \(1961\)](#), [Gilman \(1970\)](#), [Acheson \(1979\)](#) and [Hughes & Cattaneo \(1987\)](#), and these include analyses of effects like diffusion and curved geometries. In its simplest form, however, the instability is best understood by neglecting all non-ideal effects and considering modes that do not bend the magnetic field lines (interchange modes). We will now present a simple physical argument for the condition for the interchange instability as an introduction. This will be followed by a more general approach that includes several cases, such as modes which bend the field lines (undular modes).

Consider a horizontal layer of plasma under gravity and in the presence of a horizontal magnetic field. This field varies with height z . Now consider a flux tube being lifted from z to $z + dz$ (here we will write variable changes as $\phi + \delta\phi$ inside the tube and $\phi + d\phi$ outside it). Based on simple mass and flux conservation arguments (e.g. [Murray \(2007\)](#)), B/ρ is approximately conserved for a flux tube. Hence

$$\frac{B + \delta B}{\rho + \delta\rho} = \frac{B}{\rho} \quad \text{i.e.} \quad \frac{\delta B}{B} = \frac{\delta\rho}{\rho}. \quad (1.10)$$

For mechanical equilibrium the tube pressure must adjust itself to the local value, i.e.

$$\delta p + \frac{B\delta B}{\mu_0} = dp + \frac{BdB}{\mu_0}. \quad (1.11)$$

Assuming the tube moves adiabatically, its pressure and density are related by

$$\frac{\delta p}{p} = \frac{\gamma\delta\rho}{\rho}.$$

So using $\delta p = c_s^2\delta\rho$ with equation (1.10), equation (1.11) can be written as

$$(c_s^2 + c_A^2)\delta\rho = dp + \frac{BdB}{\mu_0},$$

where c_s is the sound speed and c_A is the Alfvén speed. The displaced tube will continue to rise, corresponding to the instability of the original configuration, if $\delta\rho < d\rho$, i.e. if

$$dp + \frac{BdB}{\mu_0} < (c_s^2 + c_A^2)d\rho.$$

After dividing through by dz and performing some algebraic manipulation, the above inequality reduces to

$$-\frac{g}{c_s^2} \frac{d}{dz} \log\left(\frac{B}{\rho}\right) > \frac{N^2}{c_A^2}, \quad (1.12)$$

where

$$N^2 = \frac{g}{\gamma} \frac{d}{dz} \log\left(\frac{p}{\rho^\gamma}\right)$$

is the Brünt-Väisälä, or buoyancy, frequency. We are interested in convectively stable atmospheres, where $N^2 > 0$, so that any instability that arises is due to the field stratification. From (1.12) if the field strength falls off faster than the density, the field has to hold up more mass than would be possible in its absence and so instability ensues.

We shall now consider a more general approach for deriving the conditions which determine whether or not the magnetic buoyancy instability is started.

1.3 Magnetic buoyancy

Consider a plasma which is an ideal gas, inviscid and has no magnetic diffusion. Consider also an equilibrium that is at rest and a function of height z only. For density $\rho = \rho_0(z)$, pressure $p = p_0(z)$, temperature $T = T_0(z)$ and magnetic field $\mathbf{B} = B_0(z)\hat{\mathbf{x}}$, the magnetohydrostatic balance is given by

$$\frac{d}{dz} \left(p_0 + \frac{B_0^2}{2\mu_0} \right) + \rho_0 g = 0.$$

We now perturb equations (1.1) to (1.6), with $\eta = 0$, about the equilibrium with perturbations of the form $\phi(z) \exp[i(kx + ly - \omega t)]$, where ϕ represents any of the variables. Our aim here is to derive instability criteria that hold locally, i.e. small modes compared with the scale height in question. Let $\mathbf{u} = u\hat{\mathbf{x}} + v\hat{\mathbf{y}} + w\hat{\mathbf{z}}$ and $\mathbf{B} = (B_0 + a)\hat{\mathbf{x}} + b\hat{\mathbf{y}} + c\hat{\mathbf{z}}$. Then we have

$$i\omega\rho = \rho_0(iku + ilv) + \frac{d}{dz}(\rho_0 w), \quad (1.13)$$

$$-i\omega\rho_0 u = -ikp + \frac{c}{\mu_0} \frac{dB_0}{dz}, \quad -i\omega\rho_0 v = ikb \frac{B_0}{\mu_0} - il \left(p + a \frac{B_0}{\mu_0} \right), \quad (1.14)$$

$$-i\omega\rho_0 w = -\frac{d}{dz} \left(p + a \frac{B_0}{\mu_0} \right) + ikc \frac{B_0}{\mu_0} - \rho g, \quad (1.15)$$

$$i\omega a = B_0 ilv + \frac{d}{dz}(wB_0), \quad -i\omega b = B_0 ikv, \quad -i\omega c = B_0 ikw, \quad (1.16)$$

$$-i\omega p + i\omega \frac{\gamma p_0}{\rho_0} \rho + p_0 \frac{d}{dz} \log \left(\frac{p_0}{\rho_0^\gamma} \right) w = 0, \quad (1.17)$$

$$ika + ilb + \frac{dc}{dz} = 0, \quad p = \rho RT_0 + \rho_0 RT_1. \quad (1.18)$$

We will now consider the particular case of perturbations which are very narrow in the y -direction compared with scales in the x - and z -directions; i.e. $l \rightarrow \infty$. This simplification will allow us to derive a purely algebraic¹ dispersion relation.

¹Converting an ODE to an algebraic equation can be mathematically perilous. This, however, is not a major problem for us as the instability criteria hold only locally and are derived by studying modes much smaller than the local scale height.

From (1.14), as $l \rightarrow \infty$, we must have lateral pressure balance if the perturbations are not to blow up, i.e.

$$p + \frac{aB_0}{\mu_0} = 0. \quad (1.19)$$

It follows from equation (1.19) that the vertical plasma and magnetic pressure gradients cancel in equation (1.15) in this limit. This simplifies it to

$$-i\omega w = ikc \frac{B_0}{\mu_0 \rho_0} - \frac{\rho g}{\rho_0}. \quad (1.20)$$

Similarly, from equations (1.13) and (1.18), the lateral perturbation velocity v and magnetic field b approach zero with $1/l$. Hence the disturbances are confined principally to the (x, z) -plane. Eliminating the finite product lv from (1.16) by using equation (1.13) gives

$$i\omega a + ikB_0 u - i\omega \frac{B_0 \rho}{\rho_0} + \left(B_0 \frac{d}{dz} \log \rho_0 - \frac{dB_0}{dz} \right) w = 0. \quad (1.21)$$

We may now solve the six homogeneous equations, the first in (1.14), the third in (1.16), equation (1.17) and (1.19) - (1.21) for the remaining variables u , w , a , c , p and ρ . By writing the coefficients in matrix form and then taking the determinant, the dispersion relation is found to be

$$\begin{aligned} c_f^2 \omega^4 & - \left[(c_A^4 + 2c_A^2 c_s^2) k^2 + c_A^2 g \frac{d}{dz} \log \left(\frac{B_0}{\rho_0} \right) + c_s^2 N^2 \right] \omega^2 \\ & + k^2 c_A^4 \left[k^2 c_s^2 + g \frac{d}{dz} \log B_0 + \frac{c_s^2}{c_A^2} N^2 \right] = 0, \end{aligned}$$

where c_f is the fast speed with $c_f^2 = c_s^2 + c_A^2$.

We will now consider specific cases that determine different conditions for the instability. For the isothermal case ($\gamma = 1, N^2 = 0$) and no perturbation along the field lines ($k = 0$), the instability condition is found, from the dispersion relation, to be

$$-\frac{d}{dz} \log \left(\frac{B_0}{\rho_0} \right) > 0.$$

The above relation is the same as (1.12) but without the stabilizing effect of buoyancy. For the isothermal case with perturbations that bend the field lines ($k \neq 0$), the instability condition is

$$-\frac{g}{c_s^2} \frac{d}{dz} \log B_0 > k^2.$$

This condition was found by [Gilman \(1970\)](#) where he assumed instantaneous temperature adjustment. He performed a similar analysis to that above but excluded the energy equation. For $\gamma > 1$, the interchange ($k = 0$) instability condition is given by

$$-\frac{g}{c_s^2} \frac{d}{dz} \log \left(\frac{B_0}{\rho_0} \right) > \frac{N^2}{c_A^2}.$$

This is relation (1.12) found earlier by a simple physical argument. The undular ($k \neq 0$) condition is similarly given by

$$-\frac{g}{c_s^2} \frac{d}{dz} \log B_0 > k^2 + \frac{N^2}{c_A^2}. \quad (1.22)$$

From the above relations there are two key points to observe. The first is that stratification has a stabilizing effect. Indeed, [Gilman \(1970\)](#) reasoned that because thermal relaxation is very fast in the solar interior, the magnetic buoyancy instability is a strong candidate for the escape of magnetic flux from the interior.

The second point is that in the interchange relations the derivatives are of $\log(B_0/\rho_0)$, whereas in the undular relations they are of $\log B_0$. This means that the interchange modes require a decrease in B_0/ρ_0 with height for instability and undular modes only require a decrease in B_0 with height. The condition for undular modes is more readily satisfied meaning that they are more easily generated than the interchange modes.

[Hughes & Cattaneo \(1987\)](#) looked at the key differences between the interchange and undular modes to discover precisely why the latter are favoured. For both types of mode the driving source is gravitational potential energy arising from stratification of the field. The density fluctuations necessary for liberating gravitational energy can only be created by doing a certain amount of work against pressure forces. Since interchange modes simply swap, but never bend,

field lines, work must always be done against both plasma and magnetic pressure. This is because for such motions the two are inseparable. By contrast, undular modes, which bend field lines, have strong flows along the field and hence density fluctuations can be attained by doing work principally against the thermodynamic pressure. It is this ability of the undular modes to extract energy from the field stratification while avoiding doing work against the magnetic pressure that causes them to be more readily destabilised.

The review by [Acheson \(1979\)](#) gives many other expressions which include effects such as diffusion and rotation. For the undular modes which we have been discussing, he considers perturbations of the form $\sin lz \exp i(kx + ny - \omega t)$ and derives the expression

$$-\frac{g}{c_s^2} \frac{d}{dz} \log B_0 > k^2 \left(1 + \frac{l^2}{n^2} \right) + \frac{N^2}{c_A^2}. \quad (1.23)$$

When l^2/n^2 is negligible, as in our analysis, this condition reduces to (1.22). Expression (1.23) has been used by [Archontis *et al.* \(2004\)](#) to describe the instability mechanism that causes a flux tube, which is halted at the base of the photosphere, to emerge into the higher atmosphere. This will be discussed further in later chapters.

1.4 Summary

In this chapter we have introduced magnetic flux emergence and magnetohydrodynamics (MHD), the theoretical framework required to describe it. By considering the limits of applicability of MHD, it is shown that parts of the solar atmosphere do not strictly satisfy the required conditions. The theory, however, is still capable of providing us with a qualitative understanding of the large-scale processes of flux emergence as it is essentially a set of physical conservation laws. MHD has been successfully applied to modelling the solar atmosphere for the past sixty years and, as long as results are treated with due caution, will continue to be applied with success.

The rise and emergence of flux tubes are described in terms of buoyancy. In the convection zone, magnetic flux tubes are buoyant and rise towards the

1.4 Summary

photosphere. As the photosphere is stable to buoyancy, the buoyant rise of the tubes ends in this layer. Here, the magnetic buoyancy instability allows flux from the tubes to expand and penetrate the high atmosphere. A linear stability analysis reveals the stability conditions for several limiting cases.

Chapter 2

Numerical techniques

2.1 Introduction

As highlighted in the previous chapter, magnetic flux emergence operates on a vast range of scales. It is also an inherently non-linear process, dictating that a theoretical study of the subject requires a numerical approach. Since we are considering an MHD (fluid) description, there are several techniques one can use to solve the model equations.

Spectral methods have successfully been applied to problems in MHD, such as the geodynamo (e.g. [Rüdiger & Hollerbach \(2004\)](#)), and can solve partial differential equations with high accuracy. By this we mean a high convergence rate compared to more standard finite difference/volume and finite element methods. For a grid size N , as N increases, the error in a finite difference or finite element scheme typically decreases like $O(N^{-m})$ for some constant m that depends on the order of the approximation and the smoothness of the solution. For a spectral method, we find convergence at the rate $O(N^{-m})$ for *every* m , provided the solution is infinitely differentiable. The convergence is even faster at a rate $O(c^N)$ ($0 < c < 1$) if the solution is suitably analytic ([Trefethen \(2000\)](#)). Unfortunately, these conditions on the solutions are not appropriate for flux emergence experiments. The solar atmosphere is a veritable nursery for ‘badly behaved’ solutions such as shocks (discontinuous flows). Spectral methods fail to accurately resolve such solutions and lose their convergence benefits. Thus, different schemes must be considered for this problem.

Finite element methods have not been used extensively in the modelling of solar phenomena. Their main advantage is the ability to deal with complex geometries. e.g. airflow over an aeroplane. In solar applications, the computational domain is usually geometrically simple, a box or a sphere or their 2D equivalents, and since finite element methods are computationally intensive, the main focus for the past thirty years has been on the use of finite difference and volume schemes. In particular, finite volume schemes take advantage of the integral formulation of the fluid equations and are able to admit weak solutions (e.g. shocks). This is a particularly rich field and an excellent review is presented in [Laney \(1998\)](#).

In relation to the task at hand, there is a problem which applies to any method that solves the equations in conservative form. By solving for the total energy such approaches conserve energy to machine precision. This itself is not a problem, however, when the pressure is calculated it must be found by the subtraction of the magnetic and kinetic energies from the total energy. In the low-beta plasma of the corona, the magnetic energy density dwarfs that of the thermal energy density by a factor of approximately 10^3 . With $\beta = 10^{-3}$, a 0.1% error in the magnetic field leads to a 200% error in calculating the pressure and temperature. This is unacceptable and in some pathological cases leads to a negative pressure. There exist practical solutions to this problem. e.g. [Cargill *et al.* \(2000\)](#). However, we shall now introduce another scheme that bypasses this problem by not enforcing exact energy conservation, although keeping the associated error bounded and convergent with the other difference errors. This allows for an accurate and physical result for the temperature.

The scheme referred to here is called *LARE* and solves the MHD equations via a LAgrangian REmap technique to second order accuracy ([Arber *et al.* \(2001\)](#)). It is designed specifically for problems in low-beta plasmas and has been used, successfully, in the past for studies of flux emergence (e.g. [Leake & Arber \(2006\)](#), [Archontis & Török \(2008\)](#)). For the rest of this chapter we will dissect and examine the key components of LARE. It can be thought of as containing two main parts - the Lagrangian step and the remap step. The Lagrangian step solves the MHD equations in a frame that moves with the fluid. This distorts the mesh, so to put the variables back into physical co-ordinates, the geometrical procedure of

a remap is used. These two main sections can be broken down into smaller components as shown in Figure 2.1. We shall begin our analysis with an exploration of the simple 1D Euler version of the scheme. This is followed by an extension to 3D MHD. The chapter concludes with a demonstration of the effectiveness of the scheme - an application of the 1D Euler scheme to the Riemann problem. Details of the 3D MHD scheme and of code testing can, of course, be found in *Arber et al. (2001)*.

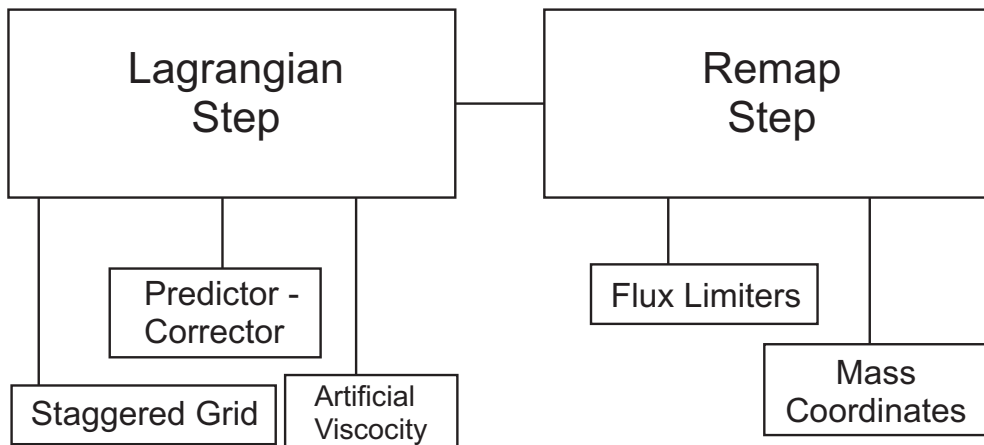


Figure 2.1: The LARE code split into its component parts.

2.2 The Lagrangian step

The Lagrangian step is an Euler step (in time) predictor-corrector scheme performed on a staggered mesh. It is a second order-scheme that does not use conservative form and includes shock viscosity to deal with shocks. To illustrate this we will now consider a 1D example where the Euler equations are evolved by one timestep in the predictor-corrector scheme. A discussion of shock viscosity shall follow this.

2.2.1 1D predictor-corrector step

Consider the 1D Euler equations in Lagrangian form,

$$\frac{D\rho}{Dt} + \rho \frac{\partial u}{\partial x} = 0, \quad (2.1)$$

$$\frac{Du}{Dt} + \frac{1}{\rho} \frac{\partial p}{\partial x} = 0, \quad (2.2)$$

$$\frac{D\varepsilon}{Dt} + \frac{p}{\rho} \frac{\partial u}{\partial x} = 0, \quad (2.3)$$

where ρ is the density, p is the pressure, u is the velocity and $\varepsilon = p/[\rho(\gamma-1)]$ is the specific internal energy density. The material derivative $D/Dt = \partial/\partial t + u\partial/\partial x$. The first feature to consider is the layout of the mesh (Figure 2.2.1). Here the

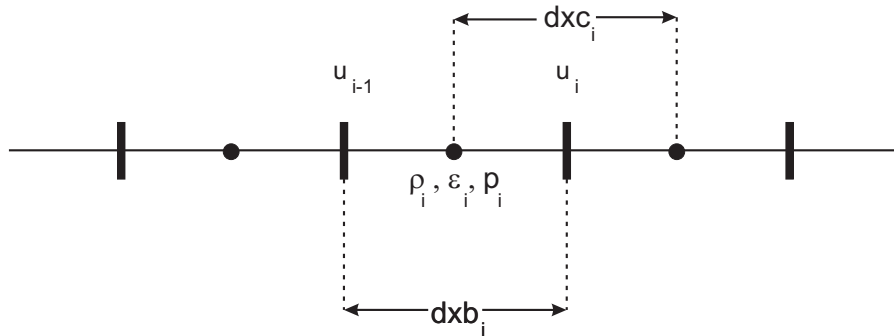


Figure 2.2: The staggered grid.

variables are defined at different positions on the grid (staggered). Normally on staggered grids, scalar quantities are defined at one place and vector quantities at another. Here we define u on the boundaries and ρ and ε at the cell centre. As we are solving in Lagrangian form the mesh will move with the fluid and become distorted from the original Eulerian configuration. Let the distance between boundaries for cell i be dxb_i and the distance from that cell centre to the next be dxc_i . After one timestep dt , the fractional change in a cell's volume is

$$\Delta = \frac{dxb_i + (u_i^{n+1/2} - u_{i-1}^{n+1/2})dt}{dxb_i}. \quad (2.4)$$

2.2 The Lagrangian step

A time centred velocity $u^{n+1/2}$ has been used to make Δ second-order accurate.

Since mass is conserved in a cell from one timestep to the next, the new density can be found from

$$\rho_i^{n+1} = \frac{\rho_i^n}{\Delta}.$$

This means that equation (2.1) need not be solved directly.

We will now look at how to discretize the Euler equations. On a staggered mesh derivatives are always centred. For example a derivative of ρ on the cell boundary would be discretized as

$$\frac{\rho_{i+1} - \rho_i}{dxc_i}.$$

Similarly, the derivative of u at the cell centre would be discretized as

$$\frac{u_i - u_{i-1}}{dxb_i}.$$

One must be careful to ensure that derivatives are defined at the correct points. Failure to do so would lead to decoupling and the chequerboard instability (Morton & Mayers (2005)).

2.2.1.1 Predictor step

The half-timestep discretisation of equation (2.3) is

$$\frac{\varepsilon_i^{n+1/2} - \varepsilon_i^n}{dt/2} = -p_i^n \frac{u_i^n - u_{i-1}^n}{\rho_i^n dxb_i^n}.$$

Notice here that the derivatives are cell-centred since ε is defined at the cell centre. The next part of the predictor is to find the grid at the half timestep.

$$dxb_i^{n+1/2} = dxb_i^n + \frac{1}{2}dt(u_i^n - u_{i-1}^n).$$

To find u^{n+1} , ε^{n+1} and ρ^{n+1} to second order we only need $p^{n+1/2}$ at first order. This can be shown by using a Taylor series to find the truncation error. The pressure at the half timestep is

$$p_i^{n+1/2} = \varepsilon_i^{n+1/2}(\gamma - 1)\rho_i^n \frac{dxb_i^n}{dxb_i^{n+1/2}}.$$

2.2.1.2 Corrector step

The update for the velocity can now be found,

$$\frac{u_i^{n+1} - u_i^n}{dt} = -\frac{p_{i+1}^{n+1/2} - p_i^{n+1/2}}{\rho_{i+1/2}^n dx c_i^n}.$$

Since u is defined at the cell boundary, we need to average ρ to find its value there ($\rho_{i+1/2}$ in the above equation). This is done by

$$\rho_{i+1/2} = \frac{dx b_i \rho_i + dx b_{i+1} \rho_{i+1}}{dx b_i + dx b_{i+1}}.$$

Notice that in the pressure derivative there are variables represented at two different times. One could write $\rho_{i+1/2}^{n+1/2} dx c_i^{n+1/2}$. However since mass is conserved it has the same value as at timestep n . This means that all derivatives can be performed on the original Eulerian grid.

To find the energy, we require the velocity at the half timestep. This is found by the simple average

$$u_i^{n+1/2} = \frac{1}{2}(u_i^n + u_i^{n+1}).$$

The updated energy can now be found from

$$\frac{\varepsilon_i^{n+1} - \varepsilon_i^n}{dt} = -p_i^{n+1/2} \frac{u_i^{n+1/2} - u_{i-1}^{n+1/2}}{\rho_i^n dx b_i^n}.$$

All that remains is to update the grid and find the new density. Hence,

$$dx b_i^{n+1} = dx b_i^n + dt(u_i^{n+1/2} - u_{i-1}^{n+1/2})$$

and

$$\rho_i^{n+1} = \rho_i^n \frac{dx b_i^n}{dx b_i^{n+1}}.$$

2.2.2 Shock viscosity

It was mentioned earlier that shocks are discontinuous, or weak, solutions to the Euler or MHD equations. Numerically, however, a shock has to be smeared over a few grid cells. If the shock is too steep, the Fourier expansion of the solution will be dominated by short wavelengths that cannot be propagated across the grid properly. This leads to either the break down of the numerical scheme or the formation of post-shock oscillations. In order to prevent these outcomes and preserve shock structure, *artificial viscosity* can be applied to the scheme. Its sole purpose is to make the flow more diffusive wherever it is required. As shocks correspond to compressions of the fluid, one technique would be to switch on the artificial viscosity when $\nabla \cdot \mathbf{u} < 0$. Instead of implementing artificial viscosity, one can calculate the *shock viscosity* for the Euler equations directly from the Rankine-Hugoniot relations. This can then be applied to the scheme to help resolve shocks. We will now derive the shock viscosity for the 1D Euler equations.

Consider the 1D Euler equations as given in equations (2.1) to (2.3). These are written in terms of the Eulerian coordinates x and t . For the following analysis we shall transform the equations into mass coordinates defined by

$$\xi = \int \rho(x, t) dx.$$

After a little algebra, the Euler equations become

$$\frac{DV}{Dt} - \frac{\partial u}{\partial \xi} = 0,$$

$$\frac{Du}{Dt} + \frac{\partial p}{\partial \xi} = 0,$$

$$\frac{DE}{Dt} + \frac{\partial}{\partial \xi}(pu) = 0,$$

where $V = 1/\rho$ and $E = \varepsilon + u^2/2$.

All of these equations are now in conservative form. This means that shocks are governed by the Rankine-Hugoniot relations,

$$u_0 - u_1 = s(V_1 - V_0), \quad (2.5)$$

$$p_1 - p_0 = s(u_1 - u_0), \quad (2.6)$$

$$p_1 u_1 - p_0 u_0 = s(E_1 - E_0), \quad (2.7)$$

where s is the shock speed. The subscript ‘1’ means ‘behind the shock’ and ‘0’ means ‘ahead of the shock’. Since $E = \varepsilon + u^2/2$, with a little algebra, equation (2.7) can be rewritten as

$$\varepsilon_1 - \varepsilon_0 = \frac{p_0 + p_1}{2}(V_0 - V_1). \quad (2.8)$$

From the definition of V it is clear that

$$V_1 - V_0 = \frac{1}{\rho_1} - \frac{1}{\rho_0}.$$

Hence equation (2.8) can be written as

$$\varepsilon_1 - \varepsilon_0 = \frac{p_0 + p_1}{2} \left(\frac{1}{\rho_0} - \frac{1}{\rho_1} \right).$$

Using equations (2.5) and (2.6), the shock speed can be written as

$$s = \rho_0 \rho_1 \frac{u_1 - u_0}{\rho_1 - \rho_0} = \frac{p_1 - p_0}{u_1 - u_0}.$$

With the ideal gas law and sound speed,

$$\varepsilon = \frac{p}{\rho(\gamma - 1)}, \quad c_s^2 = \frac{\gamma p}{\rho},$$

combined with writing $\Delta u = u_1 - u_0$ and $\Delta p = p_1 - p_0$, it follows that

$$\frac{\rho_0 \rho_1}{\rho_1 - \rho_0} \Delta u = \frac{\Delta p}{\Delta u}$$

and

$$\frac{p_1}{\rho_1} - \frac{p_0}{\rho_0} = \frac{\gamma - 1}{2\rho_0} (p_0 + p_1) \left(1 - \frac{\rho_0}{\rho_1} \right).$$

Combining these leads to the expression

$$p_1(\Delta p - \rho_0(\Delta u)^2) = p_0\Delta p + \frac{(\gamma - 1)}{2}(p_0 + p_1)\rho_0(\Delta u)^2.$$

Writing this as a quadratic for p_1 gives

$$p_1^2 - \left(2p_0 + \frac{\gamma + 1}{2}\rho_0(\Delta u)^2\right)p_1 + p_0\left(p_0 - \frac{\gamma - 1}{2}\rho_0(\Delta u)^2\right) = 0.$$

Hence, the jump condition for the pressure across the shock is

$$p_1 - p_0 = \frac{\gamma + 1}{4}\rho_0(\Delta u)^2 + \rho_0|\Delta u| \left[\left(\frac{\gamma + 1}{4}\right)^2 (\Delta u)^2 + c_s^2 \right]^{1/2}.$$

Note that in 1D $\Delta u = \Delta x \nabla \cdot \mathbf{u}$, where Δx is the cell size. To implement the above expression as viscosity, a scalar q can be added to p when the computational cells are compressed. When $c_s^2 \gg (\Delta u)^2$, this has the approximate form

$$q = \sigma_1 \rho c_s \Delta x |\nabla \cdot \mathbf{u}| + \sigma_2 \rho \Delta x^2 (\nabla \cdot \mathbf{u})^2,$$

where σ_1 and σ_2 are coefficients that are determined by experiment¹. Since this is added to the pressure there is an associated heating term added to the energy equation of $-q \nabla \cdot \mathbf{u} / \rho$. Note that q is always positive so it should only be applied when $\nabla \cdot \mathbf{u} < 0$ to ensure that shocks only ever heat.

2.3 The remap step

At the end of the Lagrangian step all the variables have been updated on a grid that has moved with the fluid. These variables need to be remapped back onto the original Eulerian grid. This process is purely geometrical, with all of the physics taking place in the Lagrangian step. To illustrate this we shall now consider the density and energy remaps in 1D (in multiple dimensions the remap step can become very complicated). Each variable is assumed to be piecewise linear.

¹Technically, the shock viscosity in this form is *artificial viscosity* and this is how it is implemented in LARE. Since it is derived from the Rankine-Hugoniot relations, however, we shall continue to refer to it as *shock viscosity*.

2.3.1 The density remap

The density is calculated throughout the code using mass conservation. At the end of the Lagrangian step the grid has evolved and the density is defined on the new grid. To remap the density back to the Eulerian grid one needs to find how much mass has entered and left the cell. For a cell i let the leaving mass be dM_i . If ρ^E is the original mass in the Eulerian cell, the mass left after the Lagrangian step is

$$\rho_i^E - dM_i + dM_{i-1}.$$

Let the total mass in an Eulerian cell at the start be $\rho_i dx b_i$ and the total mass in a Lagrangian cell after dt be $\rho'_i dx b'_i$. Conservation of mass then implies,

$$\rho_i dx b_i = \rho'_i dx b'_i.$$

Here, we use ' to signify a new time as the theory applies to any time increment

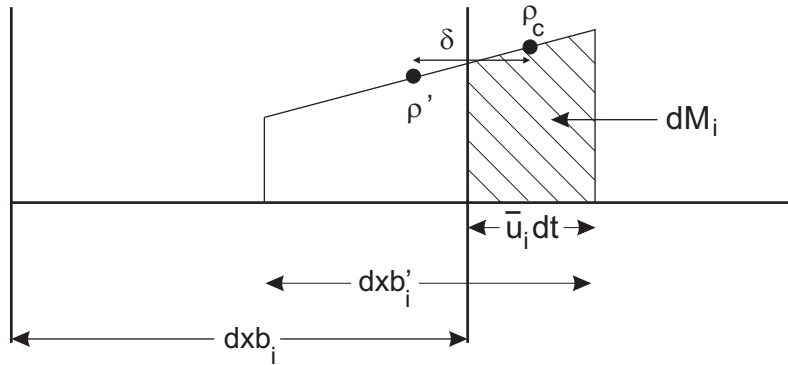


Figure 2.3: The change in mass of a cell after a timestep.

and not just integer or half-integer steps. We will now go through the calculation of dM_i . The first step is to find the density at the centre of the shaded region of Figure 2.3. From Figure 2.3 it is clear that this is

$$\rho_c = \rho'_i + \delta \frac{\partial \rho'_i}{\partial x'}.$$

By simple geometry,

$$\delta = \frac{1}{2}dx b_i - \frac{1}{2}|\bar{u}_i|dt,$$

where \bar{u}_i is the velocity of the boundary taken at the half timestep. Let

$$D_i = \frac{\partial \rho'_i}{\partial x'} \quad \text{and} \quad \psi_i = \frac{|\bar{u}_i|dt}{dx b'_i}.$$

The density can be written as

$$\rho_c = \rho'_i + \frac{dx b'_i}{2} D_i (1 - \psi_i).$$

We shall postpone the discussion of D_i until the section on flux limiters. Hence it follows that

$$dM_i = \left(\rho'_i + \frac{dx b'_i}{2} D_i (1 - \psi_i) \right) |\bar{u}_i| dt.$$

Now since

$$\rho_i^{n+1} dx b_i = \rho'_i dx b'_i - dM_i + dM_{i-1},$$

the density remap is given by

$$\rho_i^{n+1} = \rho_i + \frac{1}{dx b_i} (dM_{i-1} - dM_i).$$

2.3.2 The specific energy density remap

In the density remap the amount of mass leaving a cell, dM_i , was calculated. This knowledge can be put to good use in the specific energy density remap by working in Lagrangian coordinates. Since mass is effectively now the x -coordinate, the overlap distance, as shown in Figure 2.4, is given by dM_i . Thus, assuming $\bar{u}_i > 0$, the energy, $d\varepsilon_i$, in the shaded region of Figure 2.4 can be determined. Firstly, if the energy in an Eulerian cell i is ε_i^E , the energy left after the Lagrangian step will be

$$\varepsilon_i^E - d\varepsilon_i + d\varepsilon_{i-1}.$$

From Figure 2.4,

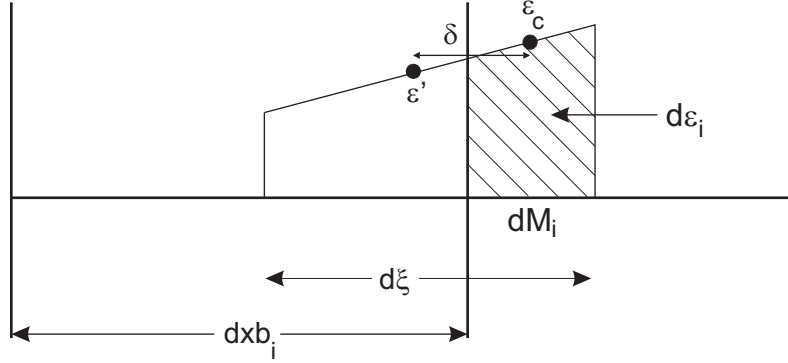


Figure 2.4: The energy change in mass coordinates.

$$d\xi = \rho_i dx b_i = \rho'_i dx b'_i.$$

Also, similar to the density case,

$$\varepsilon_c = \varepsilon'_i + \delta \frac{\partial \varepsilon'_i}{\partial \xi},$$

where ξ is the mass coordinate.

By simple geometry,

$$\delta = \left(\frac{d\xi}{2} - \frac{dM_i}{2} \right).$$

This in turn gives

$$\varepsilon_c = \varepsilon'_i + \frac{\partial \varepsilon'_i}{\partial \xi} \left(\frac{d\xi}{2} - \frac{dM_i}{2} \right).$$

Hence, the change in energy can be written as

$$d\varepsilon_i = \left(\varepsilon'_i + \frac{\partial \varepsilon'_i}{\partial \xi} \left(\frac{d\xi}{2} - \frac{dM_i}{2} \right) \right) dM_i.$$

From the definition of $d\xi$,

$$d\xi \frac{\partial \varepsilon'_i}{\partial \xi} = dx b_i \rho_i \frac{\partial \varepsilon'_i}{\partial \xi} = dx b_i \frac{\partial \varepsilon_i}{\partial x},$$

where $\partial \varepsilon_i / \partial x$ is the gradient ε on the original grid, the calculation of which will be considered in the section on flux limiters. Using this definition it follows that

$$d\varepsilon_i = \left(\varepsilon'_i + \frac{1}{2} dx b_i \frac{\partial \varepsilon_i}{\partial x} \left(1 - \frac{dM_i}{\rho'_i dx b'_i} \right) \right) dM_i.$$

Hence, the specific energy density remap is

$$\varepsilon_i^{n+1} = (\varepsilon'_i dx b'_i \rho'_i + d\varepsilon_{i-1} - d\varepsilon_i) \frac{1}{dx b_i \rho_i^{n+1}}.$$

2.3.3 The velocity remap

The velocity remap is not presented here as it is practically the same as the energy remap. The only difference is that the velocity is defined at a different position (in 1D, on the boundary rather than the cell centre) and so a different control volume is required.

2.3.4 Flux limiters

In the previous sections, the gradients D_i and $\partial\varepsilon/\partial x$ were left unknown. To calculate these, numerical tools known as flux limiters are used. These help to preserve monotonicity in the code and prevent overshooting and the growth of spurious oscillations. There are a wide variety of limiters and for a more comprehensive discussion the reader is directed to [Laney \(1998\)](#). Here we shall concentrate on a particular type of limiter called the Van Leer flux limiter.

Before the limiter can be implemented though, we need to find the gradients D_i and $\partial\varepsilon/\partial x$. Consider a piecewise linear variable f . Then $|D_i| = |df_i/dx|$ can be calculated using a third order upwind method. The reason we have chosen a third-order method is that first-order methods contain too much diffusion and second-order methods are no less computationally expensive. Hence,

$$|\bar{D}_i| = \frac{(2 - \psi_i) |f_{i+1} - f_i|}{3 dx c_i} + \frac{(1 + \psi_i) |f_i - f_{i-1}|}{3 dx c_{i-1}}, \quad \bar{u}_i > 0,$$

$$|\bar{D}_i| = \frac{(2 - \psi_i) |f_{i+1} - f_i|}{3 dx c_i} + \frac{(1 + \psi_i) |f_{i+2} - f_{i+1}|}{3 dx c_{i-1}}, \quad \bar{u}_i \leq 0.$$

Now we can implement the flux limiter to constrain the gradient. This must obey a monotonicity condition as described by [van Leer \(1997\)](#). For the velocity

boundary \bar{u}_i it has to ensure that the value of f_i , extrapolated at the boundaries of cell i , is less than f_{i+1} (the value in the next cell) and greater than f_{i-1} (the value in the previous cell). This prevents overshoots. Mathematically, these conditions can be written as

$$f_i + \frac{dx b_i}{2} \bar{D}_i < f_{i+1}, \quad \text{i.e.} \quad dx b_i \bar{D}_i < 2(f_{i+1} - f_i),$$

$$f_i + \frac{dx b_i}{2} \bar{D}_i > f_{i-1}, \quad \text{i.e.} \quad dx b_i \bar{D}_i < 2(f_i - f_{i-1}),$$

for $\bar{u}_i > 0$. These limiting constraints are obeyed by taking

$$D_i = \hat{s} \min(|\bar{D}_i| dx b_i, 2|f_{i+1} - f_i|, 2|f_i - f_{i-1}|),$$

where

$$\hat{s} = \begin{cases} \text{sign}(f_{i+1} - f_i), & \text{sign}(f_{i+1} - f_i) = \text{sign}(f_i - f_{i-1}), \\ 0, & \text{otherwise.} \end{cases}$$

The purpose of the variable s is to determine whether df/dx is positive, negative or zero.

Therefore, the overall effect of the Van Leer flux limiter is to maintain monotonicity. This, in combination with shock viscosity, provides a double-edged weapon in the accurate resolution of shocks.

2.4 The LARE steps

Now that the basics of the Lagrangian remap scheme are in place we shall examine how these are treated in the full LARE scheme. When applied to 3D MHD, the details are, obviously, technically more difficult than the 1D Euler case. However, most of the ideas involved are essentially the same. For the sake of brevity, we shall not give the full details of the scheme here. These can be found in [Arber *et al.* \(2001\)](#).

2.4.1 The LARE Lagrangian step

The equations solved by the code are

$$\frac{D\rho}{Dt} = -\rho \nabla \cdot \mathbf{u}, \quad (2.9)$$

$$\frac{D\mathbf{u}}{Dt} = \frac{1}{\rho}(\nabla \times \mathbf{B}) \times \mathbf{B} - \frac{1}{\rho} \nabla p + \frac{1}{\rho} \nabla \cdot \mathbf{T} + \mathbf{g}, \quad (2.10)$$

$$\frac{D\mathbf{B}}{Dt} = (\mathbf{B} \cdot \nabla) \mathbf{u} - \mathbf{B}(\nabla \cdot \mathbf{u}) - \nabla \times (\eta \nabla \times \mathbf{B}), \quad (2.11)$$

$$\frac{D\varepsilon}{Dt} = -\frac{p}{\rho} \nabla \cdot \mathbf{u} + \frac{\eta}{\rho} j^2 + \frac{Q_{\text{visc}}}{\rho}, \quad (2.12)$$

$$p = \frac{1}{\tilde{\mu}} \rho RT, \quad (2.13)$$

where all variables have their usual meanings. The staggered grid for 3D is shown below.

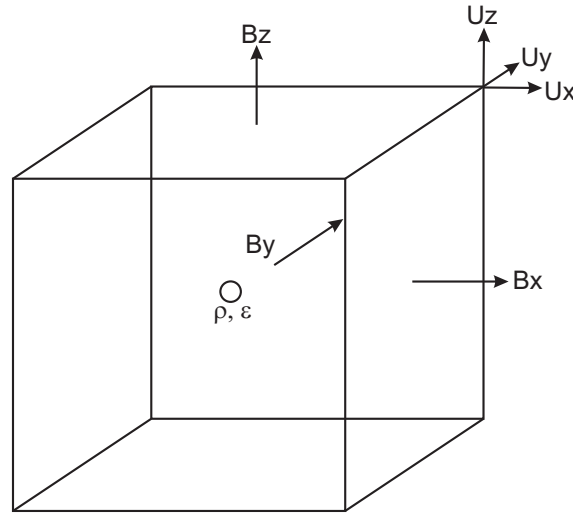


Figure 2.5: The 3D staggered grid in LARE.

Scalar variables are held in the centre of the cube, magnetic field components on the faces and velocity components at the vertex. As in the 1D example, variables are needed at different locations than those defined in Figure 2.5. The

averaging used depends on whether the variable is a volume average, e.g. ρ , or a surface average, e.g. \mathbf{B} . To start, we define $\text{cvol}_{i,j,k}$ as the volume of each cell on the Eulerian grid (in practice one can begin with a stretched grid, so that not all cells have the same volume). For the set of indices (i, j, k) $\rho_{i,j,k}$ and $\varepsilon_{i,j,k}$ are the averages over $\text{cvol}_{i,j,k}$ of density and specific energy and are defined at the cell volume centre. $Bx_{i,j,k}$ is the x -component of the magnetic field and is defined to be face-centred at $xc_{i,j,k} + dx b_{i,j,k}/2$, where $xc_{i,j,k}$ is the x -coordinate of the centre of the cell and $dx b_{i,j,k}$ is the length of the cell in the x direction. All components of velocity are defined at the cell vertex so that $vx_{i,j,k}$ is defined at the point $(xc_{i,j,k} + dx b_{i,j,k}/2, yc_{i,j,k} + dy b_{i,j,k}/2, zc_{i,j,k} + dz b_{i,j,k}/2)$. To obtain the density at the cell vertex, $\rho_{i,j,k}^v$, control volume averaging is used. i.e.

$$\rho_{i,j,k}^v = \frac{1}{8 \text{cvol}_{i,j,k}^v} \sum_{l=i}^{i+1} \sum_{m=j}^{j+1} \sum_{n=k}^{k+1} \rho_{l,m,n} \text{cvol}_{l,m,n},$$

where

$$\text{cvol}_{i,j,k}^v = \frac{1}{8} \sum_{l=i}^{i+1} \sum_{m=j}^{j+1} \sum_{n=k}^{k+1} \text{cvol}_{l,m,n},$$

is the velocity cell control volume. The \mathbf{B} field components at the cell centre are simply the averages of the values on opposing faces. The velocity components defined on cell faces, e.g. $vxb_{i,j,k}$, are found by averaging over the four vertex values.

In the 1D Euler example, the control volume is $dx b$. Using the averaging methods described above, the Lagrangian step can be written as finite difference equations similar to those described before. Again, for more details, the reader is directed to [Arber *et al.* \(2001\)](#).

The predictor magnetic field is found from the induction equation (2.11) in the form

$$\frac{D}{Dt} \int B_i d\tau = \int u_i \mathbf{B} \cdot d\mathbf{s} - \int [\nabla \times (\eta \nabla \times \mathbf{B})]_i d\tau,$$

$$\frac{D}{Dt} \int \mathbf{B} \cdot d\mathbf{s} = - \int \eta \mathbf{j} \cdot d\mathbf{l},$$

where the integrals over τ and \mathbf{ds} refer to integrals over the volume of a control volume and its surface, respectively. Integrals over \mathbf{dl} refer to line integrals around the surface integrated over in the \mathbf{ds} integral. For the magnetic field the corrector step is straightforward since \mathbf{B} does not need to be updated. The \mathbf{B} fields are simply converted into fluxes using $\Phi x = Bx dyb dyz$, etc. These fluxes are then used in the remap step to preserve $\nabla \cdot \mathbf{B} = 0$ from (2.13).

The shock viscosity described for the 1D Euler scheme is generalized for 3D MHD simulations in LARE. The tensor shock viscosity has the form

$$\sigma_{ij}^{shock} = (\nu_1 \rho c_f L + \nu_2 \rho L^2 |s|) \left(\varepsilon_{ij} - \frac{1}{3} \delta_{ij} \nabla \cdot \mathbf{u} \right),$$

where ν_1 and ν_2 are adjustable parameters, L is the the distance across the cell in the direction normal to the shock front and s is the rate of strain tensor in the direction normal to the shock front. All other symbols have their usual meanings. This is applied to all cells, not just those which are compressed, as significant shear forces may exist across expanding cells. The heating term is, however, always positive. The use of L in the formula prevents the shock viscosity from introducing grid scale noise and preserves circular shocks on the Cartesian grid.

2.4.2 The LARE remap step

The theory described in the previous sections for the remap step is also applicable to LARE. In 3D, LARE performs a series of 1D sweeps in the x , y and z directions. The sequence of these sweeps is alternated to remove any possible bias.

The calculation of magnetic flux to be remapped follows the same approach as that of the density. The total flux through the y face at $yc_{i,j,k} + dyb_{i,j,k/2}$ is unchanged during the Lagrangian step and is given by $\Phi y = By dx b dz b$ and this is remapped using the predictor velocity $ux_{i,j,k}^{n+1/2}$ to find the area of Lagrangian cells overlapping neighbouring Eulerian cells in the x pass of the remap. However, since the flux is defined as a face surface averaged quantity the velocity must be defined at the edge centre; i.e. in the calculation of $dM_{i,j,k}$, the velocity must be replaced by $(ux_{i,j,k}^{n+1/2} + ux_{i,j,k-1}^{n+1/2})/2$. In all other respects the calculation of $d\Phi y_{i,j,k}$, the y flux remapped from cell (i, j, k) to cell $(i + 1, j, k)$, follows the calculation of $dM_{i,j,k}$.

In order to preserve $\nabla \cdot \mathbf{B} = 0$, the Evans and Hawley constrained transport method is used. The solenoidal condition implies that the magnetic flux through a closed domain is zero. Considering an elementary volume, the updated fluxes are

$$\Phi y_{i,j,k}^{n+1} = \Phi y_{i,j,k} - d\Phi y_{i,j,k},$$

$$\Phi y_{i+1,j,k}^{n+1} = \Phi y_{i+1,j,k} + d\Phi y_{i,j,k},$$

$$\Phi x_{i,j,k}^{n+1} = \Phi x_{i,j,k} + d\Phi y_{i,j,k},$$

$$\Phi x_{i+1,j,k}^{n+1} = \Phi x_{i+1,j,k} - d\Phi y_{i,j,k},$$

etc., for the other components. It can easily be shown that the sum of all these components results in the cancelling of all terms for the form $d\Phi$. Thus, if the total flux through the (closed) computational domain is zero, the constrained transport scheme will keep it at zero to machine precision. More details can be found in [Bodenheimer *et al.* \(2007\)](#). Converting the fluxes back into field components then completes the LARE remap step.

2.5 The Riemann problem

To demonstrate how effective Lagrangian-remap schemes are at accurately resolving shocks we shall implement the 1D Euler scheme described earlier to solve the Riemann problem. This is a standard test for Euler codes where the initial state consists of two uniform media separated by an interface. Consider the domain $[0, 1]$ and take $\gamma = 2$. Then simple initial conditions are

$$x < \frac{1}{2} \quad \left\{ \begin{array}{l} p_L = 128 \\ \rho_L = 256/49 \\ u_L = 0, \end{array} \right.$$

and

$$x > \frac{1}{2} \quad \left\{ \begin{array}{l} p_R = 1 \\ \rho_R = 2/25 \\ u_R = 0, \end{array} \right.$$

where subscripts L and R refer to left and right of the interface at $x = 1/2$, respectively. The values here represent a large pressure jump and so would be a good test for any Euler code. At $t = 0$, the interface is removed and a flow profile develops that is defined by three waves: a shock, an expansion fan and a contact discontinuity. Shocks are jump discontinuities which, as previously mentioned, are governed by the Rankine-Hugoniot equations (2.5)-(2.7). Shock waves are compressive and may originate in an initial jump discontinuity or spontaneously from a smooth compression wave. Expansion fans (or waves) are simple waves that decrease pressure and density. Contact discontinuities create neither compression nor expansion. They form when the flow speed and pressure are continuous while there is a jump in the density. They have similarities and differences to shocks. Like shocks, they obey the Rankine-Hugoniot equations. Unlike shocks, however, they cannot form spontaneously. Rather, they must originate either in the initial conditions or in the intersection of two shocks.

For the initial conditions given above, the analytical solution to the Riemann problem is given in five regions as

$$x < \frac{1}{2} - 7t \quad \left\{ \begin{array}{l} p = 128 \\ \rho = 256/49 \\ u = 0, \end{array} \right.$$

$$\frac{1}{2} - 7t < x < \frac{1}{2} + \frac{7}{2}t \quad \left\{ \begin{array}{l} p = 128 \left(\frac{1}{7} \left(\frac{2}{3} \left(\frac{x}{t} + 7 \right) - \frac{x}{t} \right) \right)^4 \\ \rho = \frac{256}{49} \left(\frac{1}{7} \left(\frac{2}{3} \left(\frac{x}{t} + 7 \right) - \frac{x}{t} \right) \right)^2 \\ u = \frac{2}{3} \left(\frac{x}{t} + 7 \right), \end{array} \right.$$

$$\frac{1}{2} + \frac{7}{2}t < x < \frac{1}{2} + 7t \quad \left\{ \begin{array}{l} p = 8 \\ \rho = 64/49 \\ u = 7, \end{array} \right.$$

$$\frac{1}{2} + 7t < x < \frac{1}{2} + \frac{25}{2}t \quad \left\{ \begin{array}{l} p = 8 \\ \rho = 2/11 \\ u = 7, \end{array} \right.$$

$$\frac{1}{2} + \frac{25}{2}t < x \quad \left\{ \begin{array}{l} p = 1 \\ \rho = 2/25 \\ u = 0. \end{array} \right.$$

The five regions correspond to the undisturbed flow behind the expansion wave, the flow between the start of the expansion wave and the contact discontinuity, the flow between the contact discontinuity and the shock and the flow ahead of the shock. The single non-uniform region corresponds to the expansion wave.

Taking 300 gridpoints, the numerical and analytical solutions for u and ρ are overplotted for $t = 0.0324$.

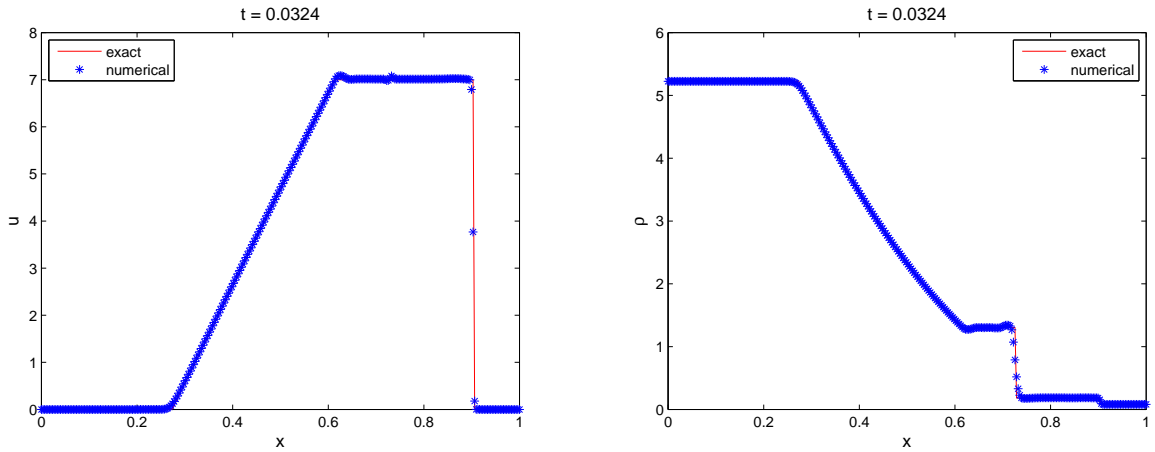


Figure 2.6: The profiles for u and ρ at $t = 0.0188$. Shock viscosity and flux limiters have been used in the construction of these solutions.

As can be seen in Figure 2.5, the Lagrangian-remap scheme accurately calculates the correct positions and propagation speeds of the shock, the expansion fan and the contact discontinuity. The above solution includes shock viscosity and Van Leer flux limiters. A closer look at the numerical solution is given in Figure 2.5.

In the u profile the numerical solution accurately captures the shock. There are some small bumps on the top plateau associated with Gibbs overshoots at the end of the expansion fan and the start of the contact discontinuity in the ρ profile. The shock is also accurately captured in the ρ profile. The contact discontinuity

2.5 The Riemann problem

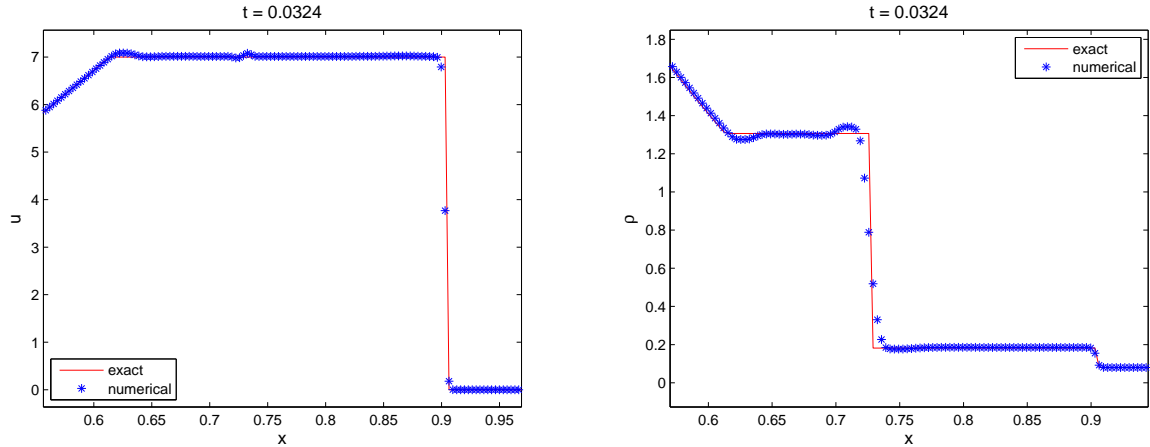


Figure 2.7: The profiles for u and ρ at the contact discontinuity and the shock.

is also well represented though the points are slightly smeared across it. This can be improved by increasing the number of points. The results of the code are successful and are comparable to those produced by a conservative solver, e.g. a Roe solver. Without shock viscosity the solution deteriorates, as shown Figure 2.8. In the u profile the bumps on the top plateau are larger and there is

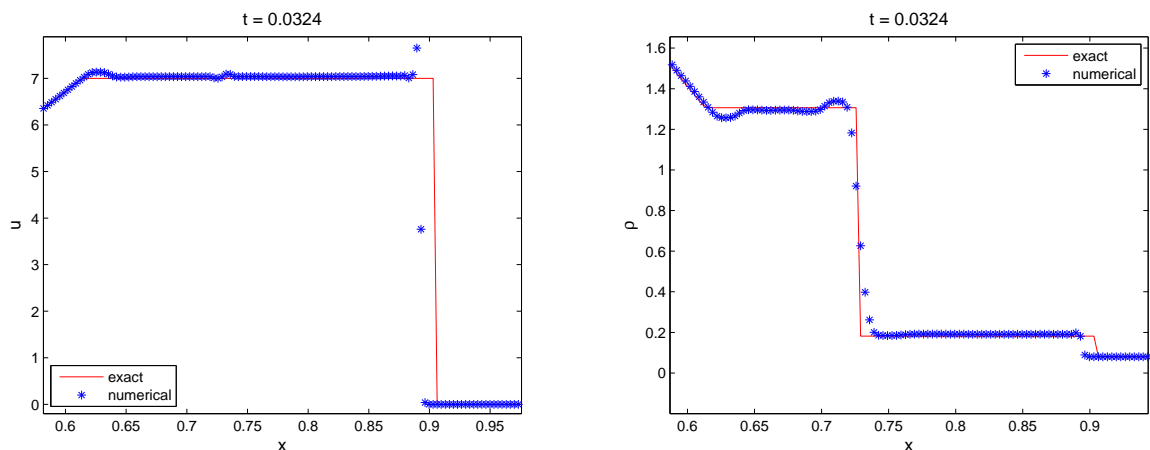


Figure 2.8: The closeup profiles for u and ρ with no shock viscosity.

a substantial overshoot at the shock. This also leads to the shock position being incorrectly predicted. In the ρ profile the Gibbs overshoots are larger and the

shock profile is inaccurate. Without flux limiters the numerical solution blows up after the first time step. They are vital for the scheme to reproduce an accurate solution.

2.6 Summary

This chapter has introduced a Lagrangian remap scheme (LARE) for solving the MHD equations. LARE is ideally suited to problems in flux emergence and in the solar atmosphere, in general. Benefits over other numerical techniques have been given and an in-depth account of the anatomy of Lare has been presented for both the Euler and MHD equations. As a test of the effectiveness of the scheme, the Riemann problem is solved and compared to an analytical solution. With the inclusion of shock viscosity and flux limiters, an accurate solution is produced. Without these, the scheme fails to resolve shocks accurately.

Chapter 3

Literature review

3.1 Review

Simulations have been used to study flux emergence for the past twenty years. In this chapter, we present a literature review where key works are highlighted and a brief synopsis is given for each. It is not exhaustive but conveys how the field has developed. We shall proceed in (approximately) chronological order but split the works into two sections: 2D/2.5D models and 3D models. The author's own publications are not included in this review since they are the subject of the following chapters of this thesis. Throughout the past two decades there has been considerable variety in the nomenclature of flux emergence. Here we shall attempt to keep descriptions as uncluttered as possible. Each synopsis is based on descriptions from the papers in question.

3.1.1 2D and 2.5D simulations

In the late 1980s and early 1990s a series of papers were published about simulations of the emergence of a magnetic flux sheet through a simplified solar atmosphere. The first of these publications that we will consider is [Shibata *et al.* \(1989a\)](#). Here they study the mechanism which allows flux to emerge. They call this the *Parker instability*, which in our terminology is just the undular mode of the magnetic buoyancy instability (see Chapter 1). This instability can occur even when the system is stable to interchange modes.

They consider a two-layer atmosphere as a simple model of the solar photosphere/chromosphere - corona system. The initial magnetic flux sheet is placed in the lower atmosphere and satisfies magnetostatic balance. To drive the instability they impose velocity perturbations of the form

$$u_x \propto \sin\left(\frac{2\pi(x - X_{max}/2)}{\lambda}\right),$$

where u_x is the horizontal velocity, λ is the wavelength of the small velocity perturbation and X_{max} is the horizontal size of the computational domain. The numerical scheme solves the ideal MHD equations.

The first case that is considered in the paper is when $\lambda = X_{max}$. Here the instability initially grows with the linear characteristics. As the instability develops, the loop expands with flux ballooning upwards. The loop accelerates in the chromosphere and then decelerates in the corona. The reason for this is that the loop is unstable to undular perturbations in the chromosphere. The magnetic buoyancy force is greater than the restoring magnetic curvature force. In the corona the pressure difference, and hence the buoyancy force, is less. The restoring curvature force becomes too strong and the loop decelerates. As the loop rises downflows are generated along the loop. These can reach speeds greater than the local sound speed. Hence shocks are observed near the footpoints of the loop.

The second case that is considered in the paper is when $\lambda \ll X_{max}$. In the low-temperature atmosphere (chromosphere) the loop demonstrates self-similar behaviour. When it reaches the corona the acceleration of the loop decreases and it eventually decelerates, as in the previous case. There are also downflows along the loop, again as in the first case. The main difference between the two cases is that in the second, the perturbation (and hence the loop) is more pronounced. This increases the restoring curvature force and hence increases deceleration when the loop reaches the corona.

The next publication in this ‘series’ is [Shibata *et al.* \(1989b\)](#). This naturally extends from the previous paper by including the extra effects of resistive MHD and an overlying coronal magnetic field. Apart from these changes, the rest of the setup is the same as in [Shibata *et al.* \(1989a\)](#). The rise of the loop follows the same behaviour as before. This time, however, the loop interacts with the

coronal field with differing results based on two separate cases. The first case is when the coronal field is parallel to the loop field. Here the loop experiences significant deceleration as it tries to push through the coronal field. For the other case where the coronal and loop fields are antiparallel this does not happen due to reconnection at the interface.

[Kaisig *et al.* \(1990\)](#) test how photospheric shearing affects the Parker instability when the conditions for it are satisfied and when they are not. The shearing motions they impose have the form

$$u_y(x) \propto \tanh\left(\frac{x - X_{max}/2}{w_{sh}}\right),$$

where w_{sh} is the horizontal width of the shearing region.

For a Parker-unstable setup, it is found that shearing motions do not have a drastic effect on the expansion of the loop. For the Parker-stable case, shearing motions are observed to make the Parker mode non-linearly unstable. The expansion of the loop is caused by the increase of magnetic pressure due to the shearing of magnetic field lines. The size of the loop and the rise velocities are smaller than for the linear case.

The ‘early’ literature we have examined so far have all used the same basic model: a two-tiered atmosphere and magnetic flux sheets. As mentioned in Chapter 1, it is currently believed that active regions are formed by the emergence of magnetic flux tubes. Another class of simulations use flux tubes for their initial magnetic field. [Magara \(2001\)](#) performed simulations of a rising flux tube from the upper convection zone to the corona. As an initial distribution of the magnetic field the Gold-Hoyle flux tube model is adopted. The gas pressure within the tube is chosen to be lower than that outside of it. The tube, however, remains in thermal equilibrium with its environment and so the tube is less dense than its surroundings. This leads to the rising of the tube.

He categorizes the rise of the tube into four main phases. In the first phase, the tube rises through the convection zone due to buoyancy. In addition, this layer is convectively unstable, so that continuous convective motion arises. As the tube is twisted, it maintains its shape throughout the rise, despite the corrosive effects of convection and the turbulent wake of the tube (see [Emonet & Moreno-Insertis \(1998\)](#)).

In the second phase the continuous rise generated in the convection zone cannot persist through the photosphere because the photosphere is a convectively stable layer that inhibits buoyancy. This results in the deceleration of the tube. Another feature is that the top of the tube becomes flattened because the top of the tube slows down while the lower part of the tube is still in the convection zone with a high rise velocity. The deformation described here is reported to be much stronger than when the tube is in the convection zone (where there is no sign of strong deformation due to weak convection).

In the third phase, as the tube is flattened, the magnetic field under the contact surface becomes parallel to the surface. A magnetic layer forms from which plasma is squeezed out the sides by horizontal surface motions. This makes the contact surface subject to the magnetic Rayleigh-Taylor instability, which, again, is the undular mode of the magnetic buoyancy instability discussed in Chapter 1.

In the fourth phase, the magnetic layer emerging through the photosphere by the magnetic Rayleigh-Taylor instability begins to expand if the surrounding gas pressure is too weak to counteract the magnetic pressure of the emerging layer. As it expands, the undulation of the magnetic layer causes plasma to flow down from inside the layer, making the layer lighter. After the light layer rises, the magnetic field also rises. This is the undular magnetic buoyancy, or Parker, instability that is responsible for the emergence of flux sheets in the previous papers that have been considered. In some respect, one can think of the flattened flux tube as a localized flux sheet. Once the magnetic flux has emerged, the loop proceeds in a self-similar manner as in previous accounts. It is also noted that not all of the flux emerges. Some of it remains trapped at the photosphere and remains there since it does not satisfy the conditions of the Parker instability.

Following on from this we shall now consider the work of [Archontis *et al.* \(2007\)](#). This paper studies the interaction of emerged flux tubes. The initial setup consists of a solar interior (a stable convection zone so as to concentrate on the emergence), a photosphere/chromosphere and a corona. Two flux tubes are initially placed at different heights in the solar interior and have the form

$$B_z = B_0 \exp\left(-\frac{r^2}{R^2}\right), \quad B_\varphi = \alpha r B_z,$$

where B_z is the field component along the tube axis, r is the radial distance from the axis, R is the radius of the tube, B_φ is the azimuthal field component and α the uniform twist. Both flux tubes have the same direction of twist. To initiate the simulation, a density deficit is introduced. This gives the tubes buoyancy and they begin to rise. The higher tube reaches the photosphere first and emerges in the fashion described by Magara (2001). The flux from this tube expands to fill the corona and acts like a coronal field for the lower flux tube to emerge into. When the lower tube reaches the photosphere and emerges, its field pushes up through the field of the other tube. As these fields are in opposite directions, a current sheet forms in between them. Eventually the field from the lower tube has pushed out as far as it can and a current sheet ‘ring’ is formed. This goes tearing-unstable and plasmoids form. The current sheet is strongest at the horizontal midpoint between the two tubes. Here a large plasmoid forms and breaks loose, ascending into the corona. After the ejection, the current ring is broken and there is an obvious change in topology. Just below where the plasmoid was ejected, a Syrovatsky-type current sheet is left. This eventually collapses into an X-point.

This simple model relates the magnetic field below the photosphere to the structure and eruptive events of the corona. It suggests that phenomena such as plasmoids, reconnection jets, loop brightening and arcade flares are coupled with the emergence and interaction of magnetic field structures from within the solar interior.

We will now turn our attention to Leake & Arber (2006) who include non-MHD terms in their simulations. All of the previous simulations described have treated the Sun as being fully ionized and an ideal gas. In reality, however, the chromosphere is only partially ionized and this paper looks at how including this affects flux emergence. To take this into account they include Cowling resistivity, $1/\sigma_c$ as well as the standard Coulomb resistivity $1/\sigma$. Cowling resistivity gives a measure of the diffusion of the magnetic field due to the collisions of ions and electrons with neutrals and acts perpendicular to the field. In the standard MHD induction and energy equations, \mathbf{J}/σ and \mathbf{J}^2/σ are replaced by $\mathbf{J}_\parallel/\sigma + \mathbf{J}_\perp/\sigma_c$ and $\mathbf{J}_\parallel^2/\sigma + \mathbf{J}_\perp^2/\sigma_c$, respectively. The Cowling resistivity must be recalculated after every iteration of the simulation from an estimation of the fraction of neutrals,

itself found from the variables ρ , T and \mathbf{B} . The diffusion layer in the chromosphere results in a faster rate of magnetic flux emergence. Another feature is that the emerging field is force-free, with all cross-field currents dissipated by ion-neutral collisions when the field crosses the chromosphere. This agrees with the widely held view that the coronal field is force-free.

A consequence of using an adiabatic energy equation is that plasma from an emerging flux tube cools the corona. To prevent this, [Leake & Arber \(2006\)](#) model the non-adiabatic energy processes in the solar atmosphere using a Newton cooling term of the form

$$\frac{d\varepsilon}{dt} = -\frac{\varepsilon - \varepsilon_0(\rho)}{\tau_r},$$

where $\varepsilon_0(\rho)$ is the equilibrium specific energy density and τ_r is the relaxation timescale. In simulating coronal heating τ_r is chosen to depend on some power of the density

$$\tau_r = \left(\frac{\rho}{\rho_{\text{ph}}}\right)^{-1.7}$$

so that at the relatively dense photosphere ($\rho = \rho_{\text{ph}}$) the timescale is about 0.1 s and is large enough that the effect becomes negligible in the sparse corona.

The relative simplicity of 2D/2.5D simulations is both a benefit and a drawback. In all of the papers discussed in this section, the flux tube or sheet must rise as a whole due to simulations having variables in only two dimensions. This prevents structures such as kinked flux tubes forming and can also create enhanced flows due to the lack of the extra degrees of freedom compared with three dimensions.

3.1.2 3D simulations

In this section we will examine a series of papers, in chronological order, concerning 3D flux emergence.

The first simulation of a 3D emerging flux tube was performed by [Fan \(2001\)](#). She considers a tube that is in thermal equilibrium and has a constant twist, with field components as described for [Archontis *et al.* \(2007\)](#) in the previous

section. In order to generate an Ω -shaped tube, the middle of the tube ($x = 0$) is made more buoyant with declining buoyancy for increasing $|x|$. This follows a Gaussian profile of the form $\exp(-x^2/\lambda^2)$, where λ gives a measure of the size of the kink. For $|x| \gg \lambda$ the tube is in mechanical equilibrium. The atmosphere is modelled as a solar interior (convectively stable), a photosphere/chromosphere, a transition region and a corona. This paper set the standard for flux emergence simulations for the next decade.

The numerical code solves the ideal MHD equations. When the simulation begins the buoyant middle part of the tube rises. As it reaches the photosphere the top of the tube flattens and it decelerates. The top of the tube then emerges into the atmosphere via the Parker instability. The axis of the tube remains constrained in the lower photosphere.

At the beginning of emergence the top part of the twisted flux tube is present at the base of the photosphere and so a nearly north-south orientated bipolar region forms. The horizontal velocity has a simple diverging pattern. Soon after, the positive and negative vertical magnetic field intensifies near the east and west corners of the region, respectively. Drawing a line from the east spot of the field intensification to the west spot, it is found to be slightly tilted anticlockwise from the east-west direction. This tilt goes against Joy's law if the emerging flux tube is in the northern hemisphere. The reason given for this is that the model does not include the effects of the Coriolis force when the tube is moving through the solar interior.

One of the key features of this simulation, which was not possible for the previous experiments in 2D, is that the emerged field structure is between foot-points in the photosphere. With the field being sheared, the inner field lines are observed to writhe into an S -shape. This is associated with sigmoidal brightenings which can be observed with X-rays.

[Magara & Longcope \(2001\)](#) have also looked at this problem but with a slightly different setup. They extend the 2.5D study of [Magara \(2001\)](#) and adopt the same temperature model and a Gold-Hoyle flux tube. The tube is in mechanical equilibrium and is then driven upwards by a velocity perturbation. Again, they solve the ideal MHD equations. Emergence proceeds as in [Fan \(2001\)](#).

[Magara & Longcope \(2003\)](#) take this investigation further with a detailed analysis of the magnetic energy, helicity and field line structure. They use the same setup as in [Magara & Longcope \(2001\)](#) with the exception of a slightly different velocity perturbation. In their experiments they observe flux emergence proceeding as normal but with the axis of the perturbed part of the tube emerging above the base of the photosphere. The axis field line however does not expand outward initially like outer field lines but remains almost horizontal with a small dip in the centre. The reason for this is that the magnetic pressure associated with this field line is less than the surrounding gas pressure. The dip at the centre is due to mass collecting there. The consequential vertical compression of the field in the dipped location increases the vertical magnetic pressure there, while the dipped nature of the field line increases the vertical tension. Eventually the upward magnetic forces defeat gravity and the field line expands outwards. [Magara & Longcope \(2003\)](#) develop a simple model to describe curved field lines and show that the evolution of the field lines is dependent upon the aspect ratio of the field line height to its footpoint distance. Field lines close to the axis have a high footpoint distance and hence a low aspect ratio. These are classed as undulating. Providing that magnetic forces are strong enough to support the dipped part against gravity, it will gradually rise and eventually reach a position where magnetic forces are dominant and the field lines can expand. Outer field lines with a high aspect ratio are classed as expanding field lines.

[Archontis *et al.* \(2004\)](#) perform numerical experiments with the aim of understanding the physical processes that have only been given brief attention in the previous literature. They begin with the initial setup of [Fan \(2001\)](#). This time, however, the resistive MHD equations are solved so that the effects of reconnection can be studied explicitly. As the flux tube rises, shock waves precede it and travel through the atmosphere with the classical structure of non-linear Lamb waves. The advance of the buoyantly rising tube is to some extent counteracted by a drag force that is exerted on the tube by the surrounding solar interior. Additionally, the axial field strength of the tube decreases as the tube rises following the law of magnetic conservation

$$B_y(z) = B_y(z_0)\rho(z)/\rho(z_0),$$

where z_0 is the initial height of the tubes axis, B_y is the axial field strength and ρ the density. When the tube reaches the photosphere the Parker instability causes the field to emerge into the atmosphere just as in [Fan \(2001\)](#) and the other previous literature. [Archontis et al. \(2004\)](#) go into more detail here and find the precise criterion for the onset of the instability ([Acheson \(1979\)](#)) to be

$$-H_p \frac{\partial}{\partial z}(\log B) > -\frac{\gamma}{2}\beta\delta + \tilde{k}_{\parallel}^2 \left(1 + \frac{\tilde{k}_{\perp}^2}{\tilde{k}_z^2}\right), \quad (3.1)$$

where H_p is the pressure scale height, γ is the ratio of specific heats, β is the plasma beta and \mathbf{k} is the wave vector with horizontal components \tilde{k}_{\parallel} parallel to the field, \tilde{k}_{\perp} perpendicular to the field and vertical component \tilde{k}_z . The remaining term δ is the superadiabatic excess given by $\delta = \nabla - \nabla_{ad}$, where ∇ is the actual temperature gradient in the equilibrium stratification and ∇_{ad} is its adiabatic value. The criterion describes the competing effects of the destabilising magnetic field gradient and the convectively stable temperature gradient. For an isothermal layer (the photosphere in this model), $\delta = -0.4$. When a flux tube rises to this layer, the value of β decreases due to the increasing magnetic pressure. Hence the first term on the right-hand side of (3.1) decreases, allowing for the magnetic buoyancy to ensue and carry magnetized plasma to the corona. Inequality (3.1) is the stability condition for the undular magnetic buoyancy instability (1.23) written in different variables.

Once the magnetic field reaches the photosphere the temperature gradient varies very little. Therefore the magnetic pressure must build up at the top of the tube so that the plasma beta falls and the stabilizing temperature gradient becomes even weaker, thus satisfying the criterion and allowing emergence. The right-hand wave term of the criterion indicates that if field lines become too bent a tension force will additionally prevent the field from emerging. The inclusion of Newton cooling, such as in [Leake & Arber \(2006\)](#), causes the convectively stable temperature gradient to be lost and so the onset of the Parker instability occurs on a faster timescale.

The post-emergence expansion follows that observed in [Fan \(2001\)](#). Isosurfaces of the current density show sigmoidal shaped current concentrations lying in the lower photosphere along the tube's axial direction. [Archontis et al. \(2004\)](#)

also run an experiment with a horizontal coronal field. This is chosen so that when the tube hits the corona, the fields are antiparallel. As the field pushes through, an arched current sheet forms and reconnection is observed.

[Galsgaard *et al.* \(2005\)](#) study the effects of a horizontal coronal field in more detail. They perform several experiments where the angles between the coronal field lines and the tube field lines vary. As in [Archontis *et al.* \(2004\)](#) an arched current sheet forms as the tube pushes into the corona. For the antiparallel case, the reconnection observed is similar to the 2D case of a Syrovatsky current sheet. At varying alignments however, the reconnection is found to be fully 3D in nature and not just a simple extension of 2D analogues. All along the arched current sheet rim, reconnection is found to generate high-velocity jets that propagate horizontally away from the emergence site.

[Manchester *et al.* \(2004\)](#) take the setup of [Fan \(2001\)](#) and run the simulation for longer. They study shear flows that develop along the polarity inversion line (PIL) of the emerging flux tube. These occur due to the expanding magnetic field in the atmosphere and are driven by the Lorentz force. It is found that after a certain time, a flux rope forms within the field of the emerged tube in the atmosphere. This is described as an eruption although the flux rope is confined by the overlying field.

[Murray *et al.* \(2006\)](#) investigate the effects of varying the magnetic field strength and the twist of a flux tube as it rises through the solar interior and emerges into the atmosphere. They find a self-similar evolution in the rise and emergence of the flux tube when the magnetic field strength of the tube is modified. During the rise through the solar interior, the height of the crest and axis, the velocity of the crest and axis and the decrease in the magnetic field strength of the axis of the tube are directly dependent on the initial magnetic field strength given to the tube. No such self-similarity is seen however when the twist of the tube is changed. This is due to the complicated interaction of the tension force on the rise of the tube. For low magnetic field strengths and twist values it is found that the tube cannot fully emerge into the atmosphere since the buoyancy instability criterion cannot be fulfilled. For tubes that do advance into the atmosphere, when the magnetic field strength has been modified, further self-similar behaviour is found in the amount of tube flux that is transported

into the atmosphere. For tubes that do emerge it is found that the variation in twist results in the buoyancy instability, and subsequent emergence, occurring at different locations along the tube's length.

[Murray & Hood \(2008\)](#) study the emergence of tubes with non-constant twist. They find that irrespective of the tube's twist profile, if the tube initially has a low tension force then it will experience greater expansion and consequential weakening of its field strength during the rise through the solar interior. Thus, upon reaching the solar surface it will fail to undergo a magnetic buoyancy instability and will not emerge into the atmosphere. For those tubes that do emerge into the atmosphere, they find little distinction between the atmospheric field and few indicators as to the initial twist profile of the tube. In general, tubes with stronger tension forces have a faster growth rate of the magnetic buoyancy instability, while tubes with weaker tension forces expand to a greater degree in the horizontal direction post-emergence. They conclude that different twist profiles only have a significant difference if the tension of the initial tube is sufficiently low.

[Moreno-Insertis *et al.* \(2008\)](#) apply a flux emergence simulation to the modelling of jets in coronal holes. Starting with the standard atmosphere of [Fan \(2001\)](#), they also include an initial oblique field to model the coronal hole. A flux tube is then inserted into the solar interior and allowed to emerge in the usual way. As the tube emerges, reconnection with the oblique field results in a jet along the open field lines. The topology of this structure bears a strong resemblance to linear force-free extrapolations of MDI magnetograms of such regions. The timescales, velocities, and other plasma properties in the experiment are consistent with recent statistical studies of this type of event made with Hinode data.

[Archontis & Török \(2008\)](#) investigate flux rope formation and eruption from flux emergence. They find flux rope formation within the expanding emerging arcade due to the shearing and reconnection of field lines at low atmospheric heights. If the tube emerges into a non-magnetized atmosphere, the flux rope rises, but remains confined inside the expanding magnetized volume. In contrast, if the expanding tube is allowed to reconnect with a pre-existing coronal field,

the flux rope experiences a full eruption with a rise profile that is in qualitative agreement with erupting filaments and Coronal Mass Ejections.

[Hood *et al.* \(2009\)](#) depart from the standard model of a cylindrical flux tube and consider a toroidal geometry. They demonstrate that with this change of geometry, the original axis of the tube, which remains trapped in the lower photosphere for the cylinder case, can rise up to coronal heights. Extensions of this work will be discussed in the following chapter.

[Archontis & Hood \(2010\)](#) revisit the models of [Archontis *et al.* \(2004\)](#) and [Archontis & Török \(2008\)](#) to investigate how changing the initial flux tube parameters affects the resulting photospheric distribution. They find that the photospheric magnetic flux distribution consists of two regions of opposite polarities and elongated magnetic tails on the two sides of the polarity inversion line (PIL). Their shape is progressively deformed due to plasma motions towards the PIL and these results are in qualitative agreement with observational studies of magnetic flux emergence in active regions. If the initial twist of the emerging tube is small, the photospheric magnetic field develops an undulating shape and does not possess tails. For all parameter cases, they find that a new flux rope is formed above the original axis of the emerging tube that may erupt into the corona, depending on the strength of the ambient field.

With the exception of [Leake & Arber \(2006\)](#) all the papers that we have considered use the MHD approximation and have come to be known as *idealized* studies. The purpose of such investigations has been to focus on a particular aspect of flux emergence and discover the underlying physics. Due to their simplicity, however, they can normally only achieve qualitative agreement with observations. A new class of simulations has developed that has the unfortunate adjective of *realistic* attached to it. ‘Realistic’ flux emergence simulations consider a more detailed energy equation, including radiative transfer, thermal conduction and partial ionization. Their main value lies in their ability to produce synthetic observations for comparison with the real Sun. We shall now describe some of the key papers.

[Cheung *et al.* \(2007\)](#) perform flux emergence simulations from the upper convection zone into the photosphere which take into account the effects of non-local radiative energy exchange, partial ionisation and magneto-convection. They use

the standard flux tube initial profile as in [Fan \(2001\)](#) and [Archontis *et al.* \(2004\)](#). When the simulation begins it is found that convection influences the evolution of the emerging magnetic field before and after it appears at photosphere. In the subphotospheric layers the convective flow distorts a rising flux tube and imposes a systematic undulation along the tube. The undulatory nature of an emerging flux tube is shown to be a consequence of its interaction with granular convection. The amount of distortion and deformation is found to be strongly dependent on the initial conditions of the tube, most notably its buoyancy and twist. Tubes with high flux suffer less deformation in the convection zone than tubes with low flux. If the tube is sufficiently twisted ($\alpha \approx 0.5$) then the emergence event is seen to be accompanied by the transient appearance of an extended darkening in the direction of the tube axis. Analysis suggests that they are associated with emerged cooled magnetic material overshooting into the photosphere.

[Martínez-Sykora *et al.* \(2008\)](#) have extended the work of [Cheung *et al.* \(2007\)](#) to simulate magnetic flux emergence from the upper convection zone to the corona (at the cost of a lower resolution). They solve the full MHD equations with non-grey, non-LTE (local thermal equilibrium) radiative transfer and thermal conduction along the magnetic field lines. They begin their simulations with the same initial profile as [Cheung *et al.* \(2007\)](#). In their discussion they state that the initial twist of the flux tube is important for determining whether or not it will emerge. This was found by [Murray *et al.* \(2006\)](#), although this is not referenced in the paper. The results from the upper convection zone to the photosphere are found to agree with those of [Cheung *et al.* \(2007\)](#). One interesting effect that is found is the increase of magnetic field strength in small regions in the atmosphere near the edges of the rising tube. They find both ‘classical’ photospheric bright points and bright features in the chromosphere. In the case of the higher lying regions, the bright points are regions of concentrated high magnetic field strength, high up- or downflowing velocity, high velocity convergence and high vorticity.

[Tortosa-Andreu & Moreno-Insertis \(2009\)](#) extend the study of [Cheung *et al.* \(2007\)](#) to include the upper layers of the photosphere and mid-chromosphere. They assume LTE between the plasma and radiation. Their experiments reveal the formation of twisted magnetic flux tubes that result from the retraction of photospheric horizontal fields at new intergranular lanes in decaying granules.

In the chromosphere, they present evidence for the non-radiative heating of the emerging magnetized plasma due to the passage of shocks and/or ohmic dissipation. High-temperature points in the magnetic domain are studied and compared to observations from the Hinode satellite.

Stein et al. (2010) simulate the rise of initially uniform, horizontal and untwisted flux sheets through the upper convection zone and their emergence through the solar surface. The magnetic field is advected upward by the diverging up-flows and pulled down in the downdrafts, which produces a hierarchy of loop like structures of increasingly smaller scale as the surface is approached. For weak field strengths, the convection dominates and the sheets show little magnetic buoyancy. For strong field strengths, magnetic buoyancy dominates and bipolar structures emerge at the photosphere.

Fang et al. (2010) extend the model of *Manchester et al. (2004)* to include convection, non-ideal equations of state and empirical coronal heating. They confirm the results of other studies such as *Tortosa-Andreu & Moreno-Inertis (2009)*. They also focus on shear flows, finding both magnetic and velocity shearing occurring at a sharp PIL.

Chapter 4

Toroidal flux emergence

4.1 Introduction

As is evident from the previous chapter, the model of choice (or perhaps of habit) for the initial magnetic field, in flux emergence simulations, is the twisted cylindrical flux tube. In the Cartesian geometry of these simulations, the cylinder model represents a localized region of a toroidal flux tube (in the global sense) where a density deficit produces the emergence of a bipolar region. They are normally placed near to the base of the photosphere for computational convenience and the physics of their emergence has been studied in considerable detail.

Although much has been learned, and continues to be learned, from the cylinder model, it has two features that have been the source of criticism. The first is that the axis of the original tube does not emerge into the corona but remains trapped in the photosphere. The second is that the two main photospheric polarities (or sunspots) of the emerging cylinder continue to drift apart until they are stopped artificially by the sides of the computational domain. In an attempt to tackle these problems, [Hood *et al.* \(2009\)](#) consider a different model for the initial magnetic field - a toroidal flux tube. By this we mean a locally toroidal tube, one that is toroidal in the Cartesian geometry of the simulation. It was demonstrated that this change in geometry can solve the problems mentioned above. In this chapter we shall look in detail at the underlying physics of toroidal flux emergence. We shall first consider the setup of the initial equilibrium and then describe the emergence process in detail, examining the effects of changing

the initial twist and field strength.

The results of this chapter have been published in

On the emergence of toroidal flux tubes: general dynamics and comparisons with the cylinder model, MacTaggart and Hood, Astronomy & Astrophysics 2009, 507, 995

4.2 Initial equilibrium

In this section we describe the basic initial equilibrium used in the flux emergence simulations of this thesis. This description will apply to all simulations in subsequent chapters and any extra features will be reported in appropriate sections. We are solving equations (2.9) to (2.13) and use a non-dimensionalization based on typical photospheric values: pressure, $p_{\text{ph}} = 1.4 \times 10^4$ Pa; density, $\rho_{\text{ph}} = 3 \times 10^{-4}$ kg m⁻³; temperature, $T_{\text{ph}} = 5.6 \times 10^3$ K and scale height $H_{\text{ph}} = 170$ km. The other units used in the simulations are: time, $t_{\text{ph}} = 25$ s; speed, $u_{\text{ph}} = (p_{\text{ph}}/\rho_{\text{ph}})^{1/2} = 6.8$ km s⁻¹ and magnetic field $B_{\text{ph}} = 1.3 \times 10^3$ G. Unless specified otherwise, all subsequent values are expressed in terms of this non-dimensionalization. $\eta = 0.001$ and this value is used in all further simulations in this thesis unless specified in the text.

4.2.1 Hydrostatic atmosphere

In complex 3D simulations, it is important to have an initial condition that is as close to an equilibrium as is practically possible in order to correctly identify physical processes and not confuse them with the effects of a non-equilibrium initial condition. The initial stratification of the atmosphere is similar to that used in previous flux emergence studies (e.g. Fan (2001), Archontis *et al.* (2004)). The solar interior ($z \leq 0$) is taken to be marginally stable to convection since in this study we are focussing on the emerging field. The effects of convection are left for future work. The photosphere/chromosphere lies in the region $0 \leq z \leq 10$,

the transition region in $10 \leq z \leq 20$ and the corona in $z \geq 20$. The (non-dimensionalized) temperature is specified as

$$T(z) = \begin{cases} 1 - \frac{\gamma-1}{\gamma}z & z \leq 0, \\ 1 & 0 < z \leq 10, \\ T_{\text{cor}}^{(z-10)/10} & 10 < z \leq 20, \\ T_{\text{cor}} & z > 20, \end{cases}$$

where $T_{\text{cor}} = 150$ is the coronal temperature. The other state variables, pressure and density, are found by numerically solving the hydrostatic equation

$$\frac{dp_0}{dz} = -\rho_0 g.$$

The subscript 0 represents quantities of the background unmagnetized plasma. i.e. outwith any flux tubes. Figure 4.1 displays the temperature and density as a function of height.

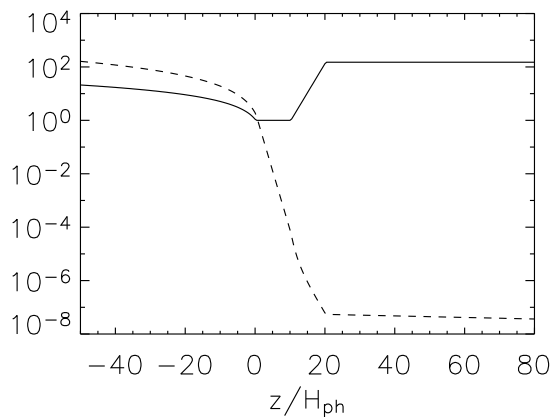


Figure 4.1: The model temperature and associated hydrostatic density as a function of height. Key: temperature (solid), density (dash).

4.2.2 Initial magnetic field

Consider the non-dimensionalized magnetohydrostatic equations with no external forces

$$\mathbf{j} \times \mathbf{B} - \nabla p_1 = \mathbf{0}, \quad (4.1)$$

$$\nabla \times \mathbf{B} = \mathbf{j}, \quad (4.2)$$

$$\nabla \cdot \mathbf{B} = 0. \quad (4.3)$$

These equations are used to find analytical expressions for the initial flux tube profiles. Here, p_1 is the pressure excess in the flux tube. The total pressure is $p = p_0 + p_1$. Hence, solving equations (4.1) to (4.3) with hydrostatic balance for the non-magnetized plasma, satisfies the full equilibrium equation

$$\nabla p = \nabla(p_0 + p_1) = \mathbf{j} \times \mathbf{B} + \rho \mathbf{g}.$$

4.2.2.1 Cylindrical flux tube

The magnetic field of a twisted cylindrical flux tube (Fan (2001)) may be given by

$$\mathbf{B} = B_y(r)\hat{\mathbf{y}} + B_\theta(r)\hat{\boldsymbol{\theta}}, \quad (4.4)$$

where

$$B_y(r) = B_0 e^{-r^2/r_0^2}, \quad (4.5)$$

$$B_\theta(r) = \alpha r B_y(r). \quad (4.6)$$

$\hat{\mathbf{y}}$ is the direction of the tube axis and $\hat{\boldsymbol{\theta}}$ is the azimuthal direction in the tube cross-section. r_0 is the radius of the tube and $r^2 = x^2 + z^2$. The flux tube is uniformly twisted with α denoting the angle of field line rotation about the axis over a unit length of the tube. B_0 is the initial field strength at the axis of the tube.

Inserting (4.4) into equation (4.1) gives the equation

$$\frac{B_\theta}{r} \frac{d}{dr}(r B_\theta) + \frac{1}{2} \frac{dB_y^2}{dr} + \frac{dp_1}{dr} = 0. \quad (4.7)$$

Solving this gives a pressure difference, relative to the background hydrostatic pressure, of

$$p_1(r) = B_0^2 e^{-2r^2/r_0^2} (\alpha^2 r_0^2 - 2 - 2\alpha^2 r^2) / 4. \quad (4.8)$$

The density deficit can then be calculated from $\rho_1 = p_1/T(z)$. As mentioned in the previous chapter, to encourage an Ω -loop, ρ_1 is multiplied by the factor e^{-y^2/λ^2} to make the middle of the tube more buoyant. This exponential factor results in the increase of the temperature in the tube with increasing $|y|$.

4.3 Toroidal flux tube

For a toroidal tube we again start from the magnetohydrostatic equations (4.1) to (4.3). If, in Cartesian coordinates, the tube axis lies in the y -direction then these equations can be written in polar coordinates (s, ϕ, x) :

$$s^2 = y^2 + (z - z_0)^2 \quad \text{with} \quad s \cos \phi = y \quad \text{and} \quad s \sin \phi = z - z_0,$$

where z_0 is the base of the computational box. We wish to solve equations (4.1) to (4.3) under the assumption of *rotational invariance*. In this case we represent the magnetic field in cylindrical coordinates (s, ϕ, x) by

$$\begin{aligned} \mathbf{B} &= \nabla A \times \nabla \phi + B_\phi \mathbf{e}_\phi \\ &= -\frac{1}{s} \frac{\partial A}{\partial x} \mathbf{e}_s + \frac{1}{s} \frac{\partial A}{\partial s} \mathbf{e}_x + B_\phi \mathbf{e}_\phi, \end{aligned}$$

where A is the flux function and is constant on magnetic field lines. This form automatically satisfies the solenoidal constraint (4.3). Taking the dot product of \mathbf{B} with equation (4.1) gives

$$\mathbf{B} \cdot \nabla p_1 = (\nabla A \times \nabla \phi + B_\phi \mathbf{e}_\phi) \cdot \nabla p_1 = 0.$$

As we are assuming rotational invariance, $\mathbf{e}_\phi \cdot \nabla p_1 = 0$. It follows that

$$p_1(s, x) = F(A(s, x)),$$

for an arbitrary function F . After some manipulation, it follows that equation (4.1) becomes

$$-\frac{1}{s} \left\{ \left[\frac{1}{s} \frac{\partial^2 A}{\partial x^2} + \frac{\partial}{\partial s} \left(\frac{1}{s} \frac{\partial A}{\partial s} \right) \right] \nabla A - \left[\frac{1}{s} \frac{\partial}{\partial s} (s B_\phi) \frac{\partial A}{\partial x} - \frac{\partial B_\phi}{\partial x} \frac{\partial A}{\partial s} \right] \mathbf{e}_\phi + B_\phi \nabla (s B_\phi) \right\} = \frac{dp_1}{dA} \nabla A. \quad (4.9)$$

By considering the ϕ -component of equation (4.9), it is the case that

$$\frac{1}{s} \left[\frac{\partial}{\partial s} (sB_\phi) \frac{\partial A}{\partial x} - \frac{\partial}{\partial x} (sB_\phi) \frac{\partial A}{\partial s} \right] = \frac{1}{s} \mathbf{B} \cdot \nabla (sB_\phi) = 0.$$

It follows from this that

$$b_\phi(s, x) = sB_\phi(s, x) = G(A(s, x)),$$

for an arbitrary function G . This allows us to write equation (4.9) in the form

$$-\frac{1}{s} \left[\frac{1}{s} \frac{\partial^2 A}{\partial x^2} + \frac{\partial}{\partial s} \left(\frac{1}{s} \frac{\partial A}{\partial s} \right) \right] \nabla A - \frac{1}{s^2} b_\phi \frac{db_\phi}{dA} \nabla A = \frac{dp_1}{dA} \nabla A.$$

Since all of the terms are in the direction of ∇A , the *Grad-Shafranov* equation has the form

$$\frac{\partial^2 A}{\partial s^2} - \frac{1}{s} \frac{\partial A}{\partial s} + \frac{\partial^2 A}{\partial x^2} + b_\phi \frac{db_\phi}{dA} + s^2 \frac{dp_1}{dA} = 0. \quad (4.10)$$

We now define a local toroidal coordinate system (r, θ, ϕ) , where

$$r^2 = x^2 + (s - s_0)^2 \quad \text{with} \quad s - s_0 = r \cos \theta \quad \text{and} \quad x = r \sin \theta,$$

with major axis s_0 . Changing to these coordinates, equation (4.10) can be expressed as

$$\frac{\partial^2 A}{\partial r^2} + \frac{1}{r} \frac{\partial A}{\partial r} + \frac{1}{r^2} \frac{\partial^2 A}{\partial \theta^2} - \frac{1}{s_0 + r \cos \theta} \left(\cos \theta \frac{\partial A}{\partial r} - \frac{\sin \theta}{r} \frac{\partial A}{\partial \theta} \right) + b_\phi \frac{db_\phi}{dA} + (s_0 + r \cos \theta)^2 \frac{dp_1}{dA} = 0. \quad (4.11)$$

To make analytical progress, we assume that the minor radius is much smaller than the major radius. Taking $\varepsilon = r_0/s_0 \ll 1$, we consider the regular expansion

$$A \sim A_0 + \varepsilon A_1 + \varepsilon^2 A_2 + \dots$$

To leading order, taking a cylindrically symmetric solution, equation (4.11) reduces to

$$\frac{1}{r} \frac{\partial}{\partial r} \left(r \frac{\partial A_0}{\partial r} \right) + \frac{1}{2} \frac{db_\phi^2}{dA_0} + s_0^2 \frac{dp_1}{dA_0} = 0.$$

Multiplying by $B_\theta = \partial A_0 / \partial r$ and changing the A_0 derivatives to r derivatives gives, with some rearrangement of variables,

$$\frac{B_\theta/s_0}{r} \frac{d}{dr} (rB_\theta/s_0) + \frac{1}{2} \frac{d(s^2 B_\phi^2/s_0^2)}{dr} + \frac{dp_1}{dr} = 0.$$

This has the same form as equation (4.7) from the cylinder model. We can therefore choose the solutions in a similar manner to those of the straight tube. These are

$$B_\phi = \frac{s_0}{s} B_0 e^{-r^2/r_0^2}, \quad B_\theta = \alpha \frac{s_0}{s} B_0 r e^{-r^2/r_0^2}.$$

The local toroidal magnetic fields can be further approximated to $O(\varepsilon)$. Notice that

$$s = s_0 \left(1 + \frac{r}{s_0} \cos \theta \right) \sim s_0 + O(\varepsilon).$$

Applying this approximation to the local toroidal magnetic fields gives

$$B_\phi \sim B_0 e^{-r^2/r_0^2} + O(\varepsilon), \quad B_\theta \sim \alpha B_0 r e^{-r^2/r_0^2} + O(\varepsilon).$$

With these approximations, B_0 and α can be compared directly to their corresponding values from the cylindrical model. The pressure difference is, as in the cylindrical case, $p_1(r) \sim B_0^2 e^{-2r^2/r_0^2} (\alpha^2 r_0^2 - 2 - 2\alpha^2 r^2) / 4$. The temperature profile is specified and the density deficit is given by

$$\rho_1 \sim B_0^2 e^{-2r^2/r_0^2} (\alpha^2 r_0^2 - 2 - 2\alpha^2 r^2) / (4T(z)). \quad (4.12)$$

The magnetic field is required in Cartesian coordinates for the purposes of simulations. Before this is found, we must express B_θ in terms of cylindrical components B_s and B_x as

$$\begin{aligned} B_s &\sim -B_\theta(r) \sin \theta + O(\varepsilon) = -B_\theta(r) \frac{x}{r} + O(\varepsilon), \\ B_x &\sim B_\theta(r) \cos \theta + O(\varepsilon) = B_\theta(r) \frac{s - s_0}{r} + O(\varepsilon). \end{aligned}$$

We can now write down the equations for the toroidal magnetic field in Cartesian coordinates

$$B_x \sim B_\theta(r) \frac{s - s_0}{r} + O(\varepsilon), \quad (4.13)$$

$$B_y \sim -B_\phi(r) \frac{z - z_0}{s} - B_\theta(r) \frac{x y}{r s} + O(\varepsilon), \quad (4.14)$$

$$B_z \sim B_\phi(r) \frac{y}{s} - B_\theta(r) \frac{x z - z_0}{r s} + O(\varepsilon). \quad (4.15)$$

4.4 Parameter study

Now that the basic model is established, we shall investigate the dynamics of toroidal flux emergence by considering a range of parameters. In this study we look at the effects of changing the initial field strength B_0 and the initial twist α . The other parameters will be kept constant with $s_0 = 15$, $r_0 = 2.5$ and $z_0 = -25$. The simulations have periodic boundary conditions on the sides of the computational box and closed boundary conditions on the top and bottom of the box. Various box dimensions and resolutions have been tested to ensure the boundary conditions have no detrimental effects on the evolution of the experiments. For the data analysed in this chapter, the dimensions of the computational box are $[-50, 50] \times [-50, 50] \times [-25, 85]$. The resolution is 256^3 .

4.4.1 Varying B_0 with fixed α : general dynamics

In this section we consider the effects of changing the initial field strength, B_0 , and keep the initial twist fixed at $\alpha = 0.2$. This twist is smaller than those used in previous studies (e.g. [Fan \(2001\)](#), [Murray *et al.* \(2006\)](#), [Hood *et al.* \(2009\)](#)) and is believed to be more applicable to the Sun. We follow the evolution for the cases $B_0 = 1, 3, 5, 7$ and 9 .

From equation (4.12) it can be seen that the buoyancy force on the tube is proportional to B_0^2 . It is then expected that tubes with a stronger B_0 will rise faster and further than those with a smaller initial value. This is confirmed in the simulations and the height-time profiles of the tube axes are displayed in [Figure 4.2](#). The axes are tracked by examining the change in B_x in the $y = 0$ plane. The field line structure is also examined to confirm that the axes do indeed pass through the plane at the change in B_x . This method is applicable since the tubes

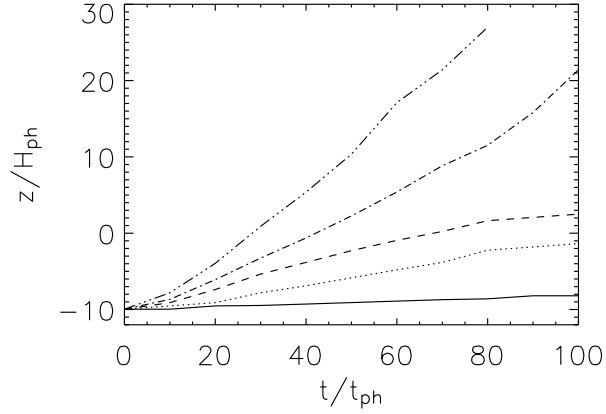


Figure 4.2: The height-time profiles for axes with different B_0 traced in the $y = 0$ plane. Key: $B_0 = 1$ (solid), $B_0 = 3$ (dot), $B_0 = 5$ (dash), $B_0 = 7$ (dot-dash) and $B_0 = 9$ (triple dot-dash).

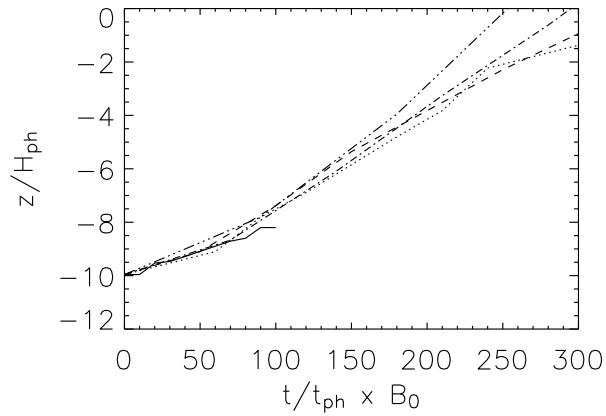


Figure 4.3: The height-time profiles in the solar interior rescaled to time $\bar{t} = tB_0$. Key: $B_0 = 1$ (solid), $B_0 = 3$ (dot), $B_0 = 5$ (dash), $B_0 = 7$ (dot-dash) and $B_0 = 9$ (triple dot-dash).

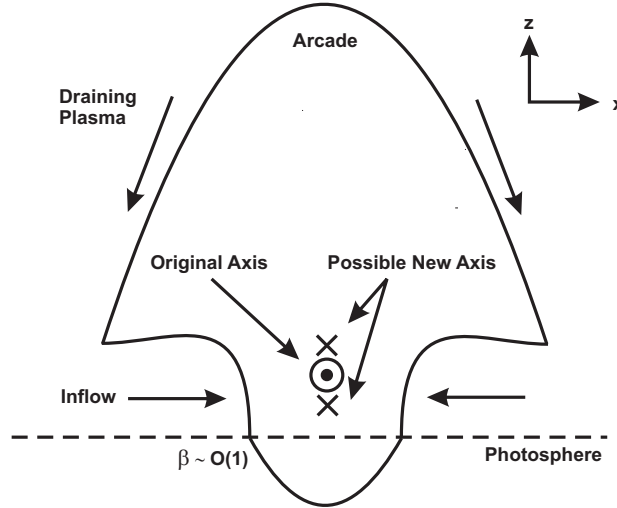


Figure 4.4: This diagram illustrates some of the main dynamical features of the emergence of a toroidal flux tube. The outline represents the outermost field line of the emerging arcade. See the text for more details.

are weakly twisted. By rescaling the time as $\bar{t} = tB_0$, the heights reached by the axes are similar in the solar interior (see Figure 4.3). This is equivalent to measuring time on the Alfvén timescale rather than on a sound timescale. Thus the heights of the tube axes are not only a function of time but also of initial field strength, i.e. $H(\bar{t}) = H(tB_0)$ where H is the height function of a tube axis. This agrees with the behaviour of cylindrical tubes as found by Murray *et al.* (2006). The two low field strength cases, $B_0 = 1, 3$, do not reach the photosphere in the time the simulation is run. These tubes may emerge if their evolution is tracked for a much longer time span. The axes of the other three cases, $B_0 = 5, 7, 9$, all emerge above the base of the photosphere. These cases differ from the cylindrical model, where the tube axis remains trapped near the base of the photosphere ($z = 0$). There is also a distinction between the cases themselves. The magnetic field evolution of the strong field cases, $B_0 = 7, 9$, differs from that of the moderate field case, $B_0 = 5$. Their axes rise to the corona whereas the axis for the $B_0 = 5$ case stops in the middle of the photosphere. Before we consider why this occurs we will describe the general behaviour of the emergence of toroidal flux tubes.

Figure 4.4 displays a diagram showing some of the main features of the emergence process based on the dynamics found in the simulations. When the flux tube

reaches the base of the photosphere ($z = 0$), the plasma beta ($\beta = p/(|\mathbf{B}|^2/2)$) of the tube at the photosphere decreases until it is $O(1)$. There the magnetic field becomes subject to a magnetic buoyancy instability and expands rapidly into the solar atmosphere which has an exponential decrease in pressure with height. As the magnetic arcade expands, the magnitude of B_y decreases with height due to flux conservation. This gradient in B_y results in a Lorentz force that drives horizontal shear flows along the neutral line between the bipolar sources. This can be understood by considering the y -component of the tension from the Lorentz force

$$\{(\mathbf{B} \cdot \nabla)\mathbf{B}\}_y = \mathbf{B} \cdot \nabla B_y.$$

The gradient of B_y is negative moving in the direction of \mathbf{B} on one side of the arcade and is positive moving in the direction of \mathbf{B} on the other. As the field is not in equilibrium, horizontal shearing occurs from the base of the photosphere to the top of the arcade.

As the magnetic field expands into the atmosphere, plasma drains from the top of the arcade and follows field lines down to the photosphere. Due to the rapid expansion of the arcade, a pressure and density deficit forms at the centre of the emerging region just above the photosphere. As the pressure at the centre of the arcade is smaller than that further out at the photosphere (laterally), plasma flows into the region of reduced pressure (see Figure 4.4). The plasma either collects there or drains down the legs of the toroidal tube.

The combination of horizontal shearing and inflow can bring together inclined field lines and initiate magnetic reconnection. This process can result in the formation of new flux ropes in the solar atmosphere. However, the new axis will be either above or below the original axis, as shown in Figure 4.4.

4.4.2 $B_0 = 5, 7$ comparison

Now that a basic description of the dynamics of toroidal flux emergence has been presented we shall examine, more closely, particular cases that exhibit different classes of behaviour. As shown before (see Figure 4.2) the original tube axis of the $B_0 = 5$ case stops rising in the middle of the photosphere, whereas the axis of the $B_0 = 7$ case rises to the corona. We shall now compare these cases.

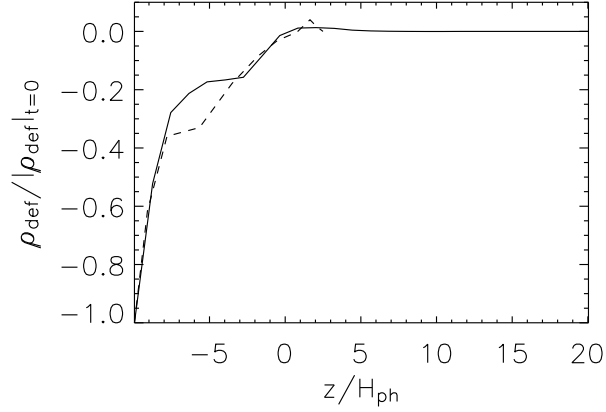


Figure 4.5: The density deficit at the tube axis (in the $y = 0$ plane) as a fraction of the initial unsigned density deficit against height. Time moves from left to right. Key: $B_0 = 5$ (dash), $B_0 = 7$ (solid).

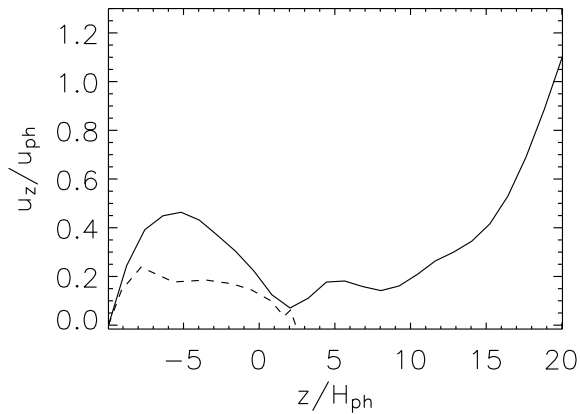


Figure 4.6: The vertical velocity, u_z , (in the $y = 0$ plane) as a function of height. u_{ph} is the photospheric velocity scale and H_{ph} is the photospheric scale height. Time moves from left to right. Key: $B_0 = 5$ (dash), $B_0 = 7$ (solid).

Figure 4.5 shows how the density deficit at the axis, as a fraction of the initial unsigned density deficit, varies with height. The deficit is calculated by taking density values from inside and outside the tube, at the same height, in the $y = 0$ plane. This gives a measure of the buoyancy of the tubes. The evolution of the two cases is similar. Both curves rise until the tubes become neutrally buoyant at $z \approx 2.5$. The $B_0 = 7$ case becomes neutrally buoyant at an earlier time than the $B_0 = 5$ case because the stronger field case rises faster. The point of neutral buoyancy corresponds to $t \approx 110$ for the $B_0 = 5$ case and $t \approx 52$ for the $B_0 = 7$ case. One important point to note is that both cases become neutrally buoyant in the photosphere. This is not found for the cylindrical model where the tubes become over-dense *before* reaching the photosphere (Murray *et al.* (2006)).

Figure 4.6 displays how the vertical velocity, u_z , at the axis varies with height. The $B_0 = 7$ case achieves more than double the rise velocity of the $B_0 = 5$ case in the solar interior. Both cases initially follow a similar profile. i.e. u_z increases until a maximum is reached and then decreases. For the $B_0 = 5$ case, the velocity decreases to approximately zero at a height $z = 2.4$. This corresponds to a time of $t \approx 110$. At this height, the $B_0 = 7$ case has a rise velocity of $u_z \approx 0.1$, at time $t \approx 52$ demonstrating that the initial choice of B_0 is crucial in determining the evolution of the axis properties. However, the story is more complicated as the axis heights in the photosphere and above are also influenced by draining flows.

As previously described, plasma drains down the emerged magnetic arcade and then flows into a region of reduced total pressure ($p + |\mathbf{B}|^2/2$). An example of this region from the $B_0 = 7$ case is displayed in Figure 4.7. This ‘square well’ profile exists between the heights of $z \approx 1.64$ and $z \approx 6.8$ for the $B_0 = 5$ case and $z \approx 1.64$ and $z \approx 5.1$ for the $B_0 = 7$ case. For $B_0 = 5$, the original tube axis rises slowly (compared with the $B_0 = 7$ case) and just reaches the bottom of the pressure deficit region when plasma flows into it. It is this plasma that flows on *top* of the original axis and prevents its further ascent. Figures 4.8 and 4.9 illustrate the positions of the original tube axis, for both cases, in relation to the field structure of the magnetic arcade at $t = 100$.

As previously described, there is horizontal shearing (y -direction) in the arcade as it expands. This motion combined with inflowing plasma can lead to magnetic reconnection. Figures 4.10 and 4.11 show examples of shearing and inflows for

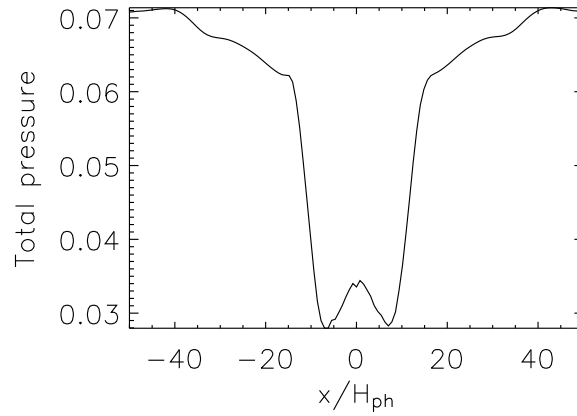


Figure 4.7: The ‘square well’ profile for the deficit in the total pressure. This deficit exists for a finite range of heights (see text) and plasma draining from above flows into it. This figure is for the $B_0 = 7$ case at $t = 100$ and $(y, z) = (0, 3)$.

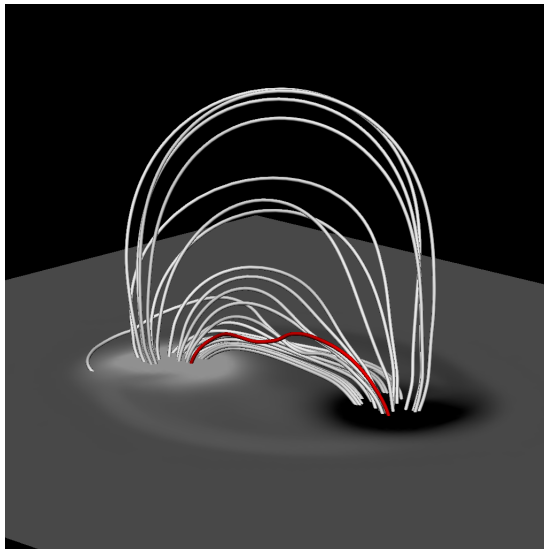


Figure 4.8: The $B_0 = 5$ case at $t = 100$. The original tube axis is represented by a red field line. Some surrounding field lines are traced in grey. A simulation magnetogram is placed at the bottom of the photosphere ($z=0$) and shows B_z .

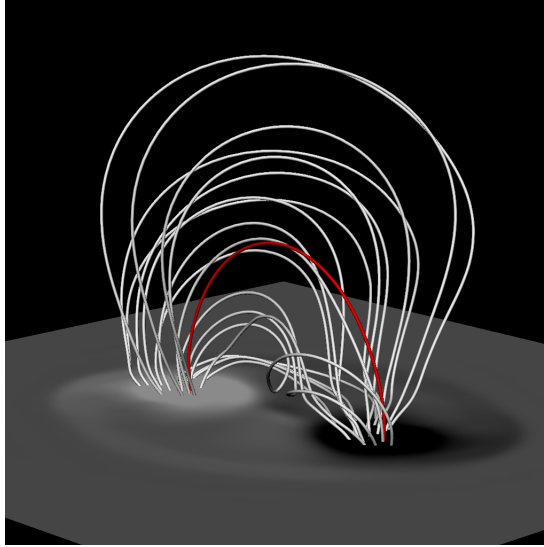


Figure 4.9: The $B_0 = 7$ case at $t = 100$. The original tube axis is represented by a red field line. Some surrounding field lines are traced in grey. A simulation magnetogram is placed at the bottom of the photosphere ($z=0$) and shows B_z .

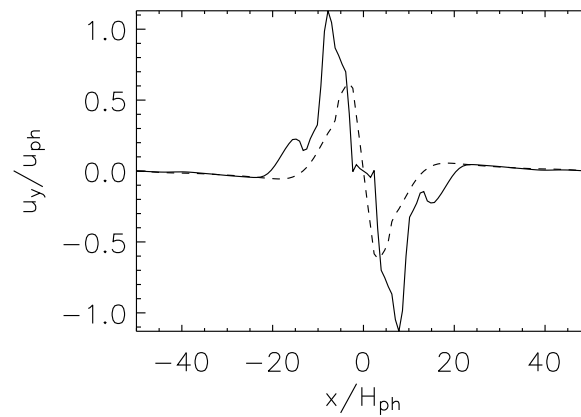


Figure 4.10: Shearing profiles at $t = 100$ and $(y, z) = (0, 3)$ for $B_0 = 5$ (dash) and $B_0 = 7$ (solid).

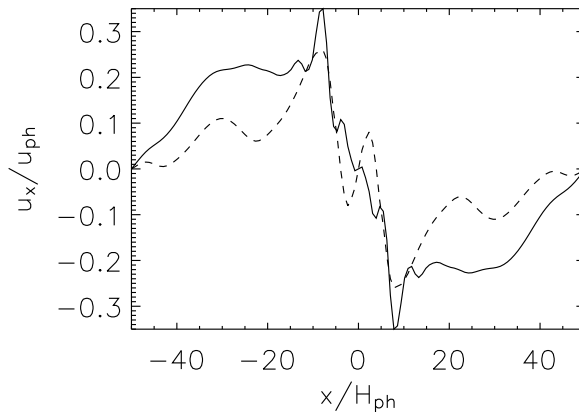


Figure 4.11: Inflow profiles at $t = 100$ and $(y, z) = (0, 3)$ for $B_0 = 5$ (dash) and $B_0 = 7$ (solid). There are clear inflow profiles for both cases. However, when the flows meet in the centre of the pressure deficit zone, they produce more complex behaviour.

both cases, respectively. The combination of these flows does indeed lead to reconnection, in both simulations, and results in the formation of new flux ropes. In the $B_0 = 5$ case, a flux rope forms above the original axis and is able to rise to the corona. Figure 4.12 shows the field line structure of the new rope for the $B_0 = 5$ case in relation to the axis of the original tube. Similar behaviour has been observed in simulations using the cylinder model. In the $B_0 = 7$ case, the original axis emerges to the corona and a new flux rope forms below it. To our knowledge this has not been found in previous theoretical flux emergence studies that use the cylinder model and do not include convection. The flux rope forms directly below the original axis and the reconnection that creates it produces an upflow. This upflow gives an extra kick to the rising of the original axis and explains the steep increase in the u_z curve for $B_0 = 7$ in Figure 4.6. The field line structure of the new flux rope in the $B_0 = 7$ case is shown in Figure 4.13.

In the emergence process not all the flux is transported into the atmosphere, some remains in the solar interior and at the base of the photosphere. To quantify how much flux emerges and how much does not we consider the horizontal flux, through the central $y = 0$ plane,

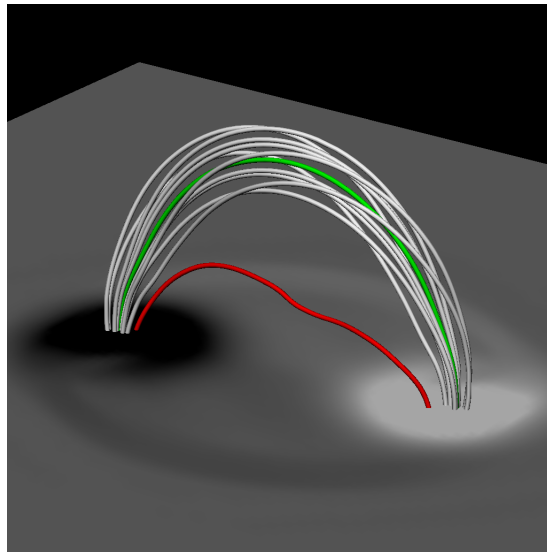


Figure 4.12: The $B_0 = 5$ case at $t = 100$. The red field line represents the original tube axis. The green field line represents the axis of a new flux rope. The surrounding field line structure at the new axis is demonstrated by some field lines traced in grey. The original axis is pinned down in the photosphere whereas the new rope is at the base of the corona. The simulation magnetogram of B_z is at $z = 0$.

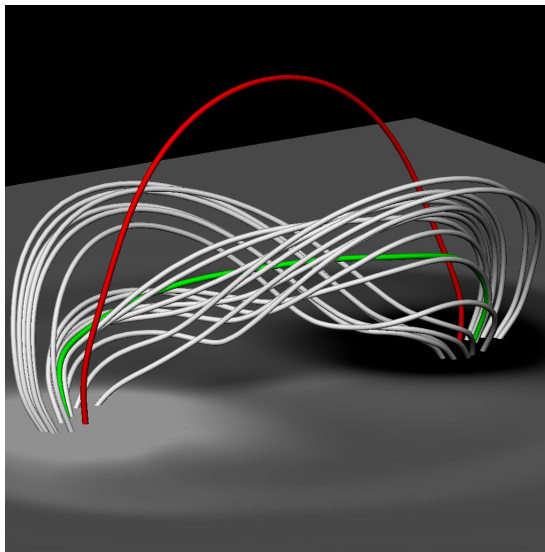


Figure 4.13: The $B_0 = 7$ case at $t = 100$. The red field line represents the original tube axis. The green field line represents the axis of a new flux rope. The surrounding field line structure at the new axis is demonstrated by some field lines traced in grey. Reconnection occurs where the grey field lines cross. An upward jet from this pushes the original axis higher. The simulation magnetogram of B_z is at $z = 0$.

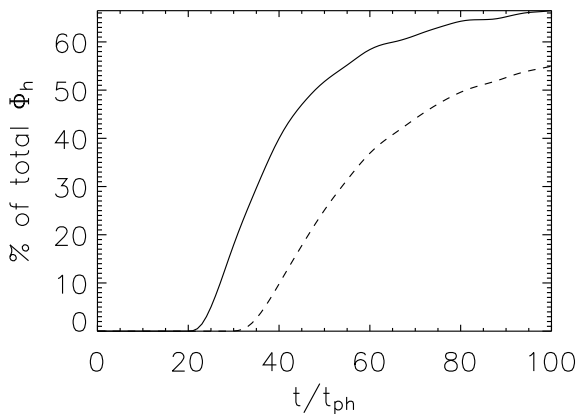


Figure 4.14: The evolution of $\Phi_h(y = 0, t)/\Phi_h(y = 0, t = 0) \times 100\%$ for $B_0 = 5$ (dash) and $B_0 = 7$ (solid) in the atmosphere ($z > 0$).

$$\Phi_h(y = 0) = \int \int B_y dx dz.$$

This integral is calculated for the regions above and below the base of the photosphere ($z = 0$). These values are shown in Figures 4.14 and 4.15 as percentages of the initial Φ_h , through time, for $B_0 = 5$ and $B_0 = 7$. As described above, the $B_0 = 7$ case rises faster and emerges before the $B_0 = 5$ case. Also, the stronger field case transports more flux into the atmosphere, as expected. The horizontal flux remains constant, for both cases, when the flux tube rises in the interior and has not yet reached the photosphere. When the tube reaches the photosphere and becomes subject to the buoyancy instability, horizontal flux is transported into the atmosphere and the same amount is depleted in the interior.

4.4.3 Plasma drainage

We have now partly answered the first criticism of flux emergence simulations, stated in the Introduction, by showing that the original axis of a toroidal tube, with sufficiently strong B_0 , can emerge to the corona. However, the problem of why this happens in the toroidal model and not in the standard cylindrical model

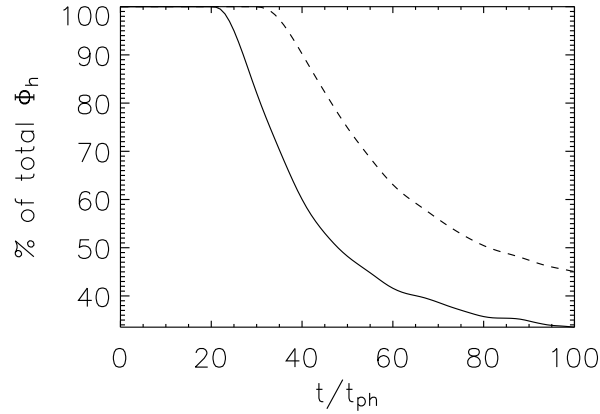


Figure 4.15: The evolution of $\Phi_h(y = 0, t)/\Phi_h(y = 0, t = 0) \times 100\%$ for $B_0 = 5$ (dash) and $B_0 = 7$ (solid) in the interior ($z < 0$).

remains to be confronted. For a cylindrical tube with $B_0 = 9$, [Murray *et al.* \(2006\)](#) find that the maximum height of the original tube axis reaches $z \approx 2$. The main difference between the two models lies in the geometry. The legs of the toroidal model rise steeply as the whole arch of the tube rises to emerge. The cylinder model, however, with its exponential buoyancy profile, kinks in the centre of the tube. The buoyant section increases as the tube rises higher. i.e. the size of the Ω -profile grows.

As the cylinder model emerges, plasma draining from the emerged arcade flows down to the photosphere and collects in multiple dips where the axis is trapped. In the toroidal model, flows exist in the legs of the tubes that correspond to draining downflows. Figures 4.16 and 4.17 show a cut of u_z through one of the legs for the $B_0 = 7$ case at $t = 40, 50$, respectively. At $t = 40$ the tube is buoyantly rising and the vertical velocity in the cut is positive. By $t = 50$, however, plasma begins to drain down the arcade and also down the legs of the tube. There is a change in sign in the velocity of the cut and this corresponds to a draining downflow. The geometry of the toroidal model allows the plasma to drain down the legs and not collect in dips. It is this property that allows the original axis of the toroidal tube to emerge.

To determine whether or not the axis can emerge in the cylinder model, we per-

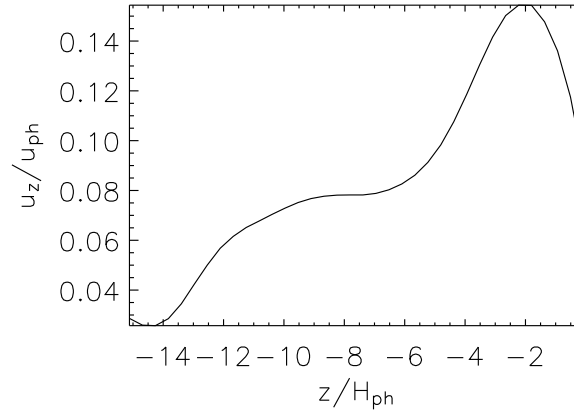


Figure 4.16: The vertical velocity profile through a cut in one of the legs of the toroidal tube at $t = 40$ and $(x, y) = (0, -13)$. The vertical velocity in the cut is positive since the tube is buoyantly rising.

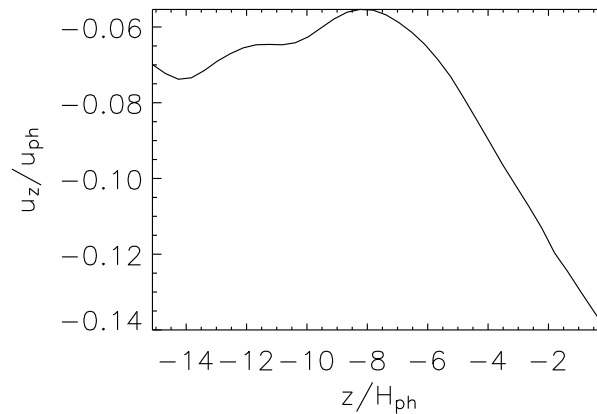


Figure 4.17: The vertical velocity profile through a cut in one of the legs of the toroidal tube at $t = 50$ and $(x, y) = (0, -13)$. The sign of the velocity in the cut has now changed since plasma drains down the leg, creating a downflow.

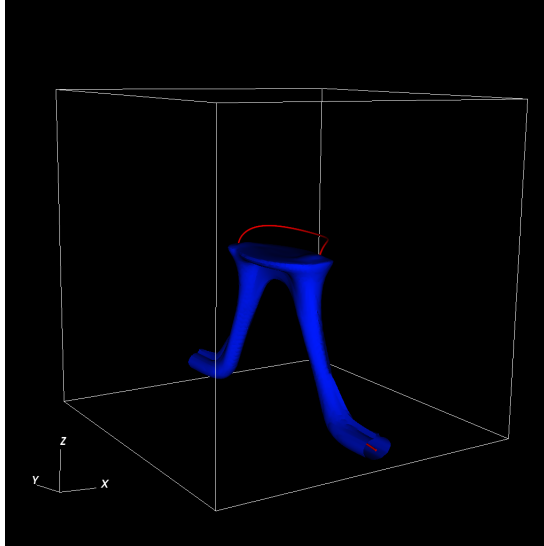


Figure 4.18: The geometry of the cylinder model with the buoyancy profile $n \exp(-y^2/\lambda^2) - (n - 1)$ exhibits a toroidal-like shape. This snapshot is at $t = 86$ and shows an isosurface of $|\mathbf{B}| = 0.5$ in blue and a field line in red indicating the axis.

form a simple test. Instead of using the standard buoyancy profile of $\exp(-y^2/\lambda^2)$, we consider

$$n \exp(-y^2/\lambda^2) - (n - 1),$$

where n is a positive integer. This is a generalization of the standard profile ($n = 1$) and will make the central part of the tube buoyant and the ends of the tube over-dense. The size of the buoyant region is controlled by n and λ . The reason for choosing this profile is to produce a toroidal-like geometry from the cylinder model. When the experiment begins, the centre will rise and the ends sink, giving the required shape. For our experiment we choose $n = 6$, $\lambda = 20$, $B_0 = 7$ and $\alpha = 0.4$. This strong twist is used to help prevent the breaking up of the tube in the solar interior. The base of the computational box is lowered to $z_0 = -50$ to allow the tube to develop a toroidal profile. Figure 4.18 depicts the shape of the tube at $t = 86$ by showing an isosurface of $|\mathbf{B}| = 0.5$ and a field line indicating the tube axis.

As mentioned at the beginning of this section, [Murray *et al.* \(2006\)](#) found that the axis of a tube with $B_0 = 9$ and $\alpha = 0.4$ rises to a maximum height of $z \approx 2$. In our experiment the, now arched, cylinder axis has risen far beyond this. By $t = 86$ the height of the axis is $z \approx 10$, the base of the transition region. This confirms that it is the geometry of the toroidal model that enables the efficient draining of plasma and so allows the axis to emerge.

This may help to explain why flux emergence studies that include convection find that the axis of the cylindrical tube emerges. If convective flows can change the geometry of the tube from cylindrical to toroidal, then the axis can emerge as in our experiment.

4.4.4 Varying α with fixed B_0

In this section we investigate the effect of varying the initial twist α . We will consider the evolution of tubes with $\alpha = 0.2, 0.3, 0.4$. We will take $B_0 = 7$ for all these cases since, as described in the previous section, this value results in the tube axis emerging with the field around the axis being vertical at the centre of the sunspots. All tubes have an initial minor radius $r_0 = 2.5$ and major radius $s_0 = 15$.

4.4.4.1 Rise and emergence

The twist of the magnetic field of a flux tube results in a tension force acting on the tube. At the top of the initial toroidal tube the density deficit at the axis is given by

$$\rho_{\text{def}} = \frac{B_0^2(\alpha^2 r_0^2 - 2)}{4T(z)}.$$

The smaller the value of α the larger the deficit. Hence the axes of tubes with smaller values of α are more buoyant than tubes with larger values. Although the whole tube is made buoyant, the top of the tube is more buoyant since $T(z)$ monotonically decreases with height in the solar interior. [Figure 4.19](#) shows the height-time profiles for the tube axes in the solar interior. As expected, the lower the twist, the faster the rise.

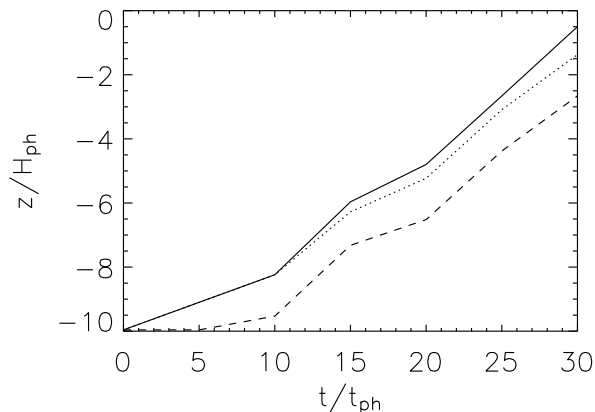


Figure 4.19: The axis height-time profiles for the cases $\alpha = 0.2$ (solid), $\alpha = 0.3$ (dot) and $\alpha = 0.4$ (dash) in the solar interior.

Once the tube reaches the photosphere, it slows down and then emerges by means of a buoyancy instability. To investigate how the initial twist influences the emergence, we look at how the unsigned vertical flux evolves with time. The total unsigned vertical flux in a plane ($z = z_0$) is defined by

$$\Phi_v(z_0) = \int \int |B_z| dx dy.$$

Here we will consider the $\alpha = 0.2$ and $\alpha = 0.4$ cases. Figure 4.20 shows the height-time profile for the top of the magnetic field. i.e. the top of the tube and its expansion into the atmosphere. Figure 4.21 displays the evolution of Φ_v for the different twist cases in the plane $z = 10$ (base of the transition region).

The $\alpha = 0.2$ case rises to the photosphere before the $\alpha = 0.4$ case. At the photosphere, however, the smaller twist case takes longer to become subject to the buoyancy instability than the larger one. This means that both cases emerge at approximately the same time. Murray *et al.* (2006) found similar behaviour for the cylinder model. Once emerged, the field of the $\alpha = 0.4$ case rises faster and further than the $\alpha = 0.2$ case. This is shown in Figure 4.20. Figure 4.21 shows the evolution of Φ_v for $\alpha = 0.4$ begins before that of $\alpha = 0.2$. It also rises at a faster rate and by $t = 94$ there is double the amount of unsigned vertical flux compared with the $\alpha = 0.2$ case. When at the photosphere, the field for

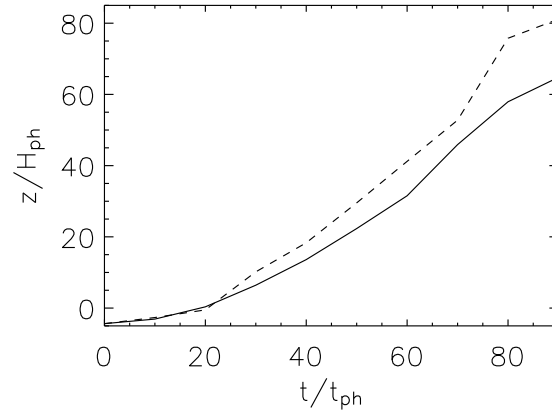


Figure 4.20: The height-time profiles of the tops of the magnetic fields of tubes with different twists. Key: $\alpha = 0.2$ (solid), $\alpha = 0.4$ (dash).

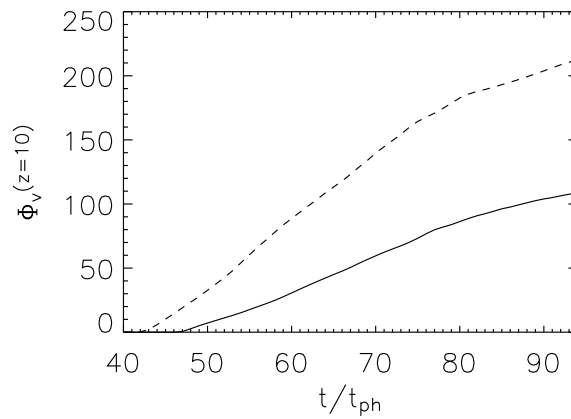


Figure 4.21: The evolution of the vertical flux through $z = 10$, Φ_v , for tubes with different twists. Key: $\alpha = 0.2$ (solid), $\alpha = 0.4$ (dash).

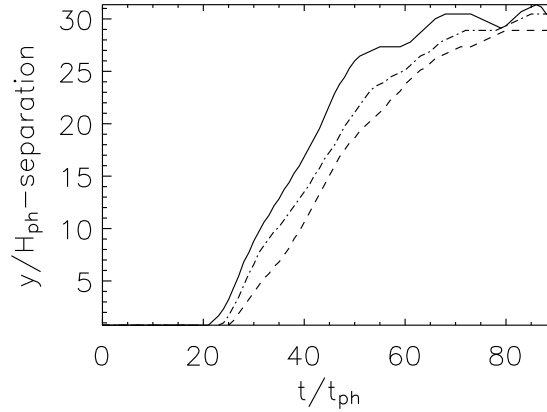


Figure 4.22: The y -separation in time of the maximum and minimum B_z at the base of the photosphere ($z=0$). The higher the twist, the slower the separation. Key: $\alpha = 0.2$ (solid), $\alpha = 0.3$ (dot-dash), $\alpha = 0.4$ (dash).

the $\alpha = 0.2$ case was weaker than that of the $\alpha = 0.4$ case. Therefore, the field emerging into the atmosphere is also weaker, resulting in a weaker evolution of the total unsigned flux.

4.4.4.2 Sunspot drift

A simulation drawback of the cylinder model, which is the second criticism described in the Introduction, is that the sunspot pair it produces continually drifts apart until it reaches the edge of the computational box. Although a density deficit is introduced into the tube to form an Ω -loop, the entire tube is in fact buoyant since the $\exp(-y^2/\lambda^2)$ profile makes the ends of the tube weakly buoyant. This is what causes the sunspots to drift apart. In the toroidal model, although the entire tube is made buoyant, the ‘feet’ of the flux tube are held at a fixed distance apart in the solar interior. Figure 4.22 shows the y -separation of the maximum and minimum B_z the base of the photosphere ($z = 0$) for the twist cases $\alpha = 0.2, 0.3, 0.4$. As described above, the lower the twist, the faster the rise to the photosphere. Once the tubes reach the photosphere, the fields begin to spread. The sunspot separation increases linearly until a peak distance is reached

and the y -separation remains approximately constant. This peak distance corresponds to the major diameter of the initial tube. In this example, $2s_0 = 30$. The constancy of the separation between the two main opposite polarities (sunspots) in an active region is often used as a criterion for the region's maturity (e.g. [Liu & Zhang \(2006\)](#)). Tubes of a higher twist will spread laterally more slowly than tubes of a lower twist since a higher twist produces a stronger tension force. The slopes for the linear separation phase are estimated to be 0.833 for $\alpha = 0.2$, 0.815 for $\alpha = 0.3$ and 0.8 for $\alpha = 0.4$.

The maximum separation of the sunspots in these simulations is determined by the distance of the almost vertical flux tube legs at the base of the numerical box. This has consequences for the structure of the magnetic field in the interior. The classic picture of flux emergence, as mentioned in Chapter 1, considers flux tubes with long wavelengths in the convection zone, typically generated by $m = 1, 2$ instabilities at the tachocline, where m is the longitudinal wavenumber. In the local Cartesian approximation near the surface, this can be represented by the cylinder model. The toroidal model, on the other hand, has vertical legs. There are two possible mechanisms for forming toroidal tubes in the convection zone. Either the modification of the cylindrical tube takes the form of that described in § 4.4.3, namely the (enhanced) buoyant region of the cylindrical tube is spatially limited and takes effect deeper in the convection zone (rather than near the photosphere as in previous simulations) or the instability, at the base of the convection zone, involves a higher longitudinal mode, e.g. $m > 10$. Both cases would produce toroidal shaped tubes with almost vertical legs.

4.5 Summary

In this chapter we have carried out a parametric study of the emergence of buoyant *toroidal* flux tubes through the solar interior and into the atmosphere. By varying two of the parameters, namely B_0 and α , we have been able to investigate the general behaviour of the emerging tubes.

Keeping α constant, the variation of the initial field strength produces a wealth of behaviour. In the solar interior the buoyancy force is proportional to B_0^2 . Tubes with stronger B_0 rise faster and further than those with lower values. In the

solar interior the tubes exhibit a self-similar behaviour. By rescaling the time to $\bar{t} = tB_0$, the axis height-time profiles for the different B_0 lie on top of each other. This shows that the axis heights of the tubes are not only a function of time but also of B_0 .

Once emerged, the evolution of the tubes can vary strongly depending on the choice of the initial field strength. A value between $B_0 = 5$ and $B_0 = 7$ gives a threshold between two general classes of behaviour. For the $B_0 = 7$ case, the axis rises fast enough to emerge into the atmosphere before plasma draining from the field above flows into a pressure deficit and blocks its ascent. The plasma instead drains below the axis and produces reconnection upflows that further increase the height of the axis. For the $B_0 = 5$ case, the axis does not rise fast enough to escape plasma draining on top of it and so is pinned down in the photosphere.

An advantage of the toroidal model over the standard cylinder model is that the axis of the original tube is able to emerge into the atmosphere and so the field at the centre of the sunspots is vertical. This is made possible by the ability of the plasma to drain down the legs of the tube in the solar interior. In the cylinder model such draining is not possible and plasma collects in dips along the tube axis. It has been shown, however, that by changing the buoyancy profile to produce a toroidal shape, the tube axis can achieve greater heights in the solar atmosphere.

Keeping B_0 constant, the variation in α also produces interesting behaviour. In the solar interior it is found that tubes with lower twists rise faster than tubes with higher twists. Once at the photosphere, however, low twist tubes take longer to become subject to the magnetic buoyancy instability. This allows higher twist tubes to catch up and emerge approximately at the same time.

It is found that the amount of flux emerged into the atmosphere depends on the value of α . The higher the twist the more flux is transported upwards. In the rise of a flux tube, the stronger the twist, the more preserved the tube remains. The field strength of higher twisted tubes is stronger than lower twisted tubes when they emerge. This manifests itself in the amount of flux that is transported into the atmosphere.

Another feature of the toroidal model, which improves upon the cylinder model, is that the sunspots drift to a fixed separation and then stop. This

4.5 Summary

separation is determined by the major diameter of the original tube, $2s_0$. The y -separation of the maximum and minimum values of B_z increases linearly until the maximum separation of the major diameter is reached. The higher the twist of the tube, the slower the separation rate.

Chapter 5

Coronal eruptions

5.1 Introduction

Coronal mass ejections are the most violent forms of eruption in the solar system. They can eject enormous amounts of mass (10^{10} to 10^{13} kg) and achieve speeds from 300 to 500 km/s. Some fast CMEs have been found that can even reach reach speeds in excess of 2000 km/s. The issue of CME genesis has been of interest to theoreticians for some time. Excellent accounts of this topic are [Forbes \(2000\)](#), [Schindler \(2006\)](#) and [Vršnak \(2008\)](#).

One popular model for CME initiation is the *breakout model* ([Antiochos *et al.* \(1999\)](#)). The initial condition for the breakout model, in its most basic form, is a quadrupolar magnetic field. There are four flux domains. Two consist of flux joining the neighbouring bipole polarity and the inner flux region where the innermost polarities connect. In the outer flux region the magnetic field joins the outer two polarities above the other regions. The initial flux in the inner region must exceed the flux in the outer region for breakout to occur.

To initiate an eruption, this configuration is stressed by shearing the central arcade through an imposed photospheric flow on the lower boundary. The X-point becomes distorted into a horizontal current layer. As the shearing increases, the diffuse current evolves into a thin current sheet that results in rapid reconnection. This reconnection allows for the transfer of magnetic flux from the inner and overlying systems to the side arcades. The loss of the field above the sheared central arcade leads to a runaway expansion. This, together with

the increase in magnetic pressure due to the additional flux from reconnection at the top current sheet, leads to the formation of a current sheet in the central arcade. Reconnection here results in the expulsion of a flux rope. These stages are illustrated in Figure 5.1. There have been several simulations of breakout in 2.5D (Antiochos *et al.* (1999), MacNeice *et al.* (2004), van der Holst *et al.* (2007), Soenen *et al.* (2009)) and some recent simulations in 3D (DeVore & Antiochos (2008), Lynch *et al.* (2008)).

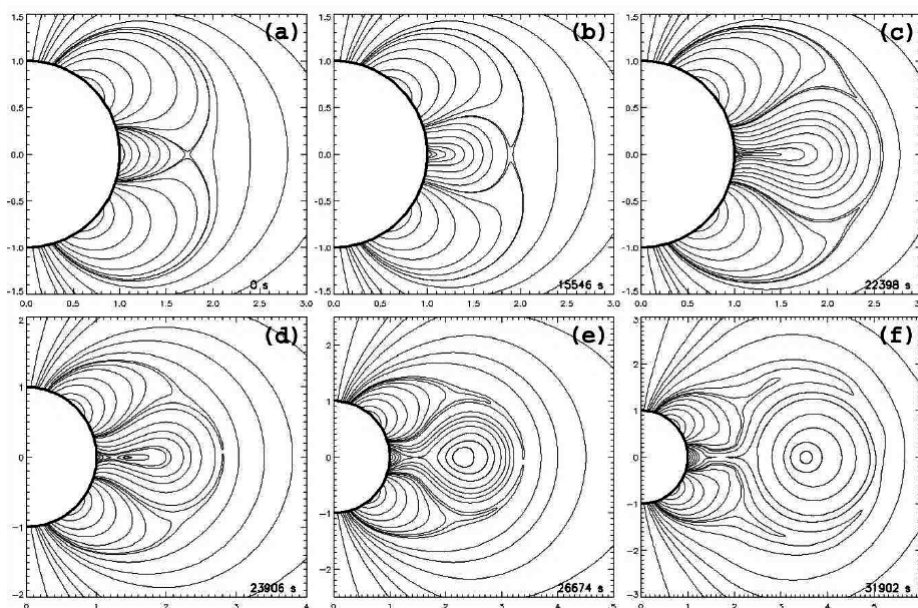


Figure 5.1: Meridional projections of magnetic field lines throughout the magnetic breakout eruption process at six different times. (a) shows the initial quadrupolar structure. (b) and (c) show the expanding inner region due to increased magnetic pressure from shearing at the photosphere. The null point is deformed into a current sheet and external reconnection takes place. (d) and (e) show continued expansion and the pinching off of a flux rope through internal reconnection. (f) shows the outer expansion of the new flux rope. This diagram is from Lynch *et al.* (2008). Spatial units are in solar radii.

There have been many observational studies of CMEs with a mixture of

results. Some work claims to find breakout-compatible eruptions (Li & Luhmann (2006)) and others find eruptions that are incompatible (Ugarte-Urra *et al.* (2007)). A comprehensive list of observational papers related to the breakout model is given in Lynch *et al.* (2008). Observational work has also tried to find the link between CME eruption and flux emergence. Zhang *et al.* (2008) published a statistical survey of 189 CME-source regions, 46 active regions and 15 newly emerging active regions. They find that 60% of the CME-source regions have a flux increase during 12 hours before the eruption and 40% show a magnetic flux decrease. They conclude that the relationship between CMEs and flux emergence is complicated and that flux emergence alone is not unique as a trigger for a CME.

In this chapter, we perform a theoretical study of the relationship between CME eruption and flux emergence. First, we attempt to produce magnetic breakout self-consistently using only flux emergence and without the imposition of an ad-hoc photospheric shearing motion. We then extend the results of the previous chapter and examine how the flux ropes that form in toroidal emergence can escape.

The results of this chapter have been published in

Can magnetic breakout be achieved from multiple flux emergence?, MacTaggart & Hood 2009, Astronomy & Astrophysics, 501, 761

and

Multiple eruptions from magnetic flux emergence, MacTaggart & Hood 2009, Astronomy & Astrophysics, 508, 445

5.2 Modelling magnetic breakout with flux emergence

In all the breakout simulations listed in the previous section, the solar atmosphere is modelled as the corona with the lower boundary representing the photosphere. The initial setup is altered by *imposed shearing motions* at the photosphere. The continued application of these motions results in breakout, as described previously. A recent 2.5D simulation has been performed by [Zuccarello *et al.* \(2008\)](#) where, instead of shearing, they drive breakout by flux emergence. Here flux emergence is simulated by imposing a time-dependent condition on the photospheric boundary. They produce a CME from a detached helmet streamer, included in the initial condition, and not from the pinching off of a flux rope from the central arcade, as in the original model of [Antiochos *et al.* \(1999\)](#).

In this section, we attempt to model magnetic breakout in a more self-consistent manner by using flux emergence alone. As the original breakout model is 2.5D, we also perform 2.5D MHD simulations. We solve equations (2.9) to (2.13) and use the standard atmosphere of Chapter 4. The simulation box has periodic side boundaries. The top and bottom boundaries are closed. In dimensionless coordinates, the simulation box has size $[0,400] \times [-50,140]$. The resolution is 800^2 . Flux tubes are modelled as twisted cylinders. For a single tube, the axial magnetic field is given by

$$B_z = B_0 \exp(-r^2/R^2),$$

where B_0 is the initial magnetic field strength at the axis of the tube and $r = \sqrt{(x - x_0)^2 + (y - y_0)^2}$ is the radial distance from the axis of the tube at (x_0, y_0) . The flux tubes are uniformly twisted and have an azimuthal component given by

$$B_\varphi = \alpha r B_z,$$

where α is the initial twist.

5.2.1 Quadrupolar initial condition

It was found by Archontis *et al.* (2007) that, in 2.5D, the interaction of two flux tubes results in the formation of a quadrupolar magnetic field in the solar atmosphere, the initial condition to the breakout model. The key stages of this process are described in Chapter 3. We examine the effect of changing the lateral distance between the axes of the initial two tubes by performing four experiments. The tubes are kept at the same strength, twist and radius ($B_0 = 5$, $\alpha = -0.4$ and $R = 2.5$) in all the experiments and only the original positions are changed. The four experiments involve two tubes placed in the solar interior with lateral separation of the axes of (i) 20, (ii) 40, (iii) 60 and (iv) 80 units respectively. The left-hand tube is always placed at $y = -5$, while the right-hand tube is placed at heights $y = -8; -9; -10; -11$, respectively. The reason for this is because when the tubes are further away from each other it takes the left-hand tube longer to expand over the right-hand tube and provide a field for it to emerge into. This means that the right-hand tube is slightly weaker, at the same height, for experiments with a larger initial separation. None of the experiments, however, are symmetric and the differences are slight. Each case produces a quadrupolar formation. Figure 5.2 portrays the profile of a typical quadrupolar formation from the experiments. The black contours outline field lines and the colourmap shows the magnitude of the magnetic field. Note that $|\mathbf{B}|$ is, locally, a minimum near the X-point. The X-point is not a null point as there is still an axial component of the magnetic field into the plane of the figure. We will now examine some of the important features of this quadrupolar formation.

5.2.1.1 Photospheric conditions

Here we will consider the field at times long after the formation of the quadrupole. These times will vary due to the different initial tube separation of the various cases. As mentioned before, it is often the case in the modelling of solar eruptions that the atmosphere is taken to be the corona, with $\beta \ll 1$, and the bottom boundary is taken to be the photosphere. Footpoints of a magnetic field are assumed to be fixed at this bottom boundary, unless a flow is artificially imposed.

5.2 Modelling magnetic breakout with flux emergence

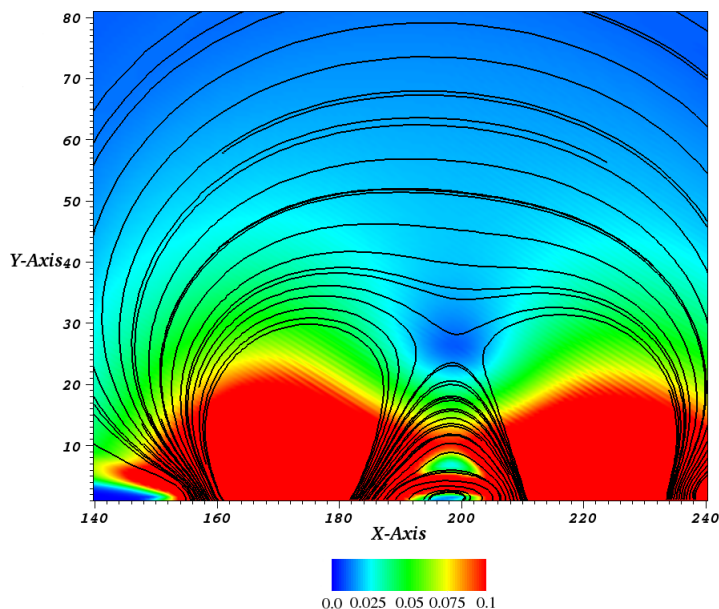


Figure 5.2: The resulting quadrupole from experiment (i) where the tubes have an initial lateral separation of 20. The colourmap shows $|\mathbf{B}|$ and some field lines are traced in black.

On examination of the forces at the base of the photosphere ($y = 0$) in our experiments, however, the assumption of a fixed field profile at the photosphere is not strictly true. Since, in this region, $\beta \approx 1$, flows in the plasma can influence the field and move it. Long after the formation of the quadrupole, the lateral plasma forces approximately balance. For example, the x -component of the Lorentz force approximately balances the lateral plasma pressure gradient, $\partial p / \partial x \approx (\mathbf{j} \times \mathbf{B})_x$. This implies there is no horizontal acceleration and that $u(x, 0, t) \approx \text{constant}$. From the simulations, this velocity component is small but nonzero and approximately constant in time. The z -component of the Lorentz force gives rise to a shearing motion. However, the magnitude of u_z is an order of magnitude smaller than u_x . Dynamically, the main effect is the lateral spreading of the system.

Consider experiment (i), with an initial lateral separation of 20, at time $t = 275$. The initial formation of the quadrupolar structure occurs around $t \approx 120$. Figure 5.3 compares the horizontal component of the Lorentz (solid curve) and

5.2 Modelling magnetic breakout with flux emergence

plasma pressure gradient (dashed curve) forces at the photospheric base $y = 0$.

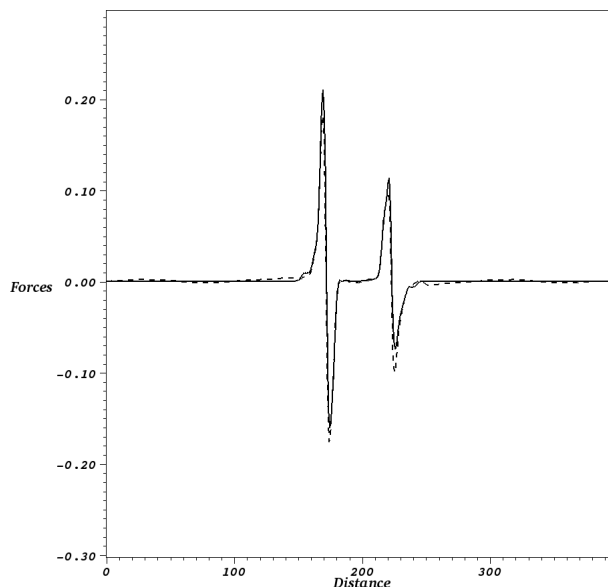


Figure 5.3: The solid line shows $(\mathbf{j} \times \mathbf{B})_x$ and the dashed line, $\partial p / \partial x$. Both cuts are taken at the photosphere at time $t = 275$ for experiment (i).

The forces are nearly in balance so that the resultant force is extremely small. The approximate steady state horizontal flow, at the photospheric base $y = 0$, is displayed in Figure 5.4. This shows that there remains a steady flow that is slowly moving the magnetic sources apart. The left hand tube is moving to the left and the right hand tube is moving to the right. Although the flows are highly subsonic, it does mean that the magnetic sources do not remain at fixed locations. However, this is exactly what one would expect. If the magnetic field has to be sufficiently strong (i.e. β around unity) to emerge, then the Lorentz force and the pressure gradient forces will be large enough to move the photospheric footpoints apart.

If we now consider experiment (iv), with an initial axial separation of 80, at time $t = 338$ (the later time is needed as the quadrupolar structure takes longer to form due to the larger separation of the tubes), the profiles are remarkably

5.2 Modelling magnetic breakout with flux emergence

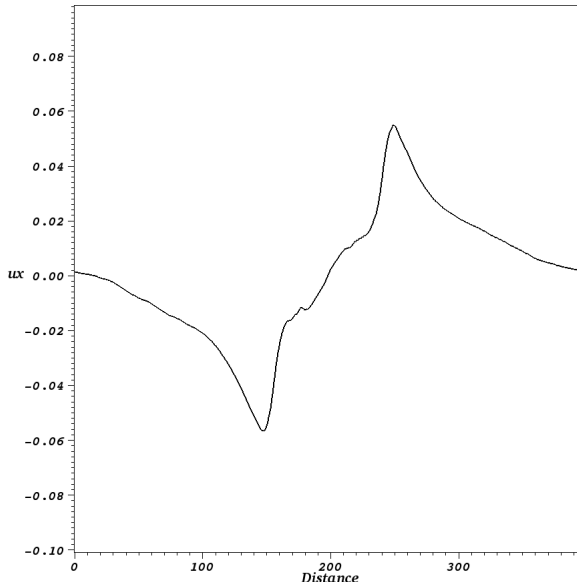


Figure 5.4: The horizontal speed at the photosphere at $t = 275$ for experiment (i).

similar (compare Figures 5.5 and 5.6 with Figures 5.3 and 5.4, respectively, for experiment (i)). The largest magnitude of speed for the profile of experiment (iv) is 0.76 times that of experiment (i). Since the initial separation of the tubes in experiment (iv) is four times that in experiment (i), it suggests that the initial separation has only a minor effect on the steady-state drift velocity at the photosphere.

5.2.1.2 Current densities

In the original breakout model ([Antiochos *et al.* \(1999\)](#)) the initial condition is a potential quadrupolar field. In order to compare our work with others, we examine the magnitude of the current density and determine if the fields are close to potential. Here we shall consider experiment (ii) with an initial axial separation of 40. Figure 5.7 shows the variation of $|\mathbf{j}|$ with height, from the photosphere, through the centre of the simulation box, $x = 200$. This also passes very close to the X-point. The currents below the corona are much stronger than

5.2 Modelling magnetic breakout with flux emergence

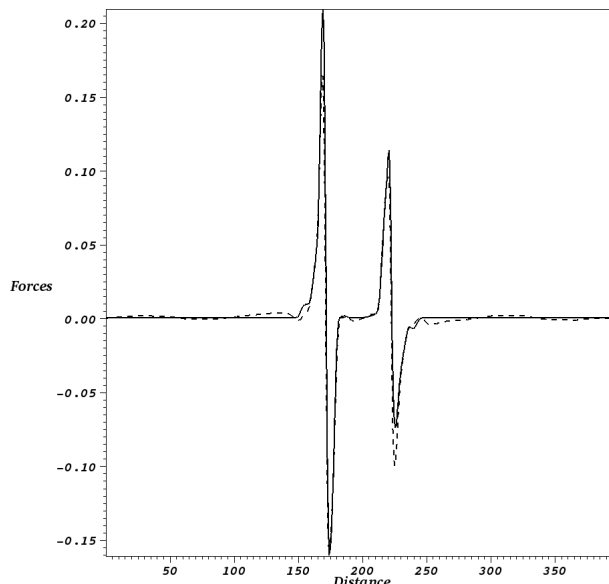


Figure 5.5: The solid line shows $(\mathbf{j} \times \mathbf{B})_x$ and the dashed line, $\partial p / \partial x$. Both cuts are taken at the photosphere at time $t = 338$ for experiment (iv).

those above it. Increasing in height from the photosphere, the current density decreases. This decrease is not monotonic, however, and is due to bands of flux that connect the two flanking tubes (see Figure 5.2). Above the corona, the current density continues to decrease until a sharp rise at a height of $y = 33$. This is the position of the X-point. Beyond this the current becomes negligible compared with sub-coronal values.

We will now consider how the magnitude of the current density compares with that of the magnetic field. Figure 5.8 shows the logarithmic variation of $|\mathbf{j}|/|\mathbf{B}|$ with height through the same cut as in Figure 5.7. Below the corona there are bands of flux connecting the two flanking tubes. This results in peaks and troughs where the current dominates and is dominated, respectively, in the ratio with the magnetic field strength. Increasing in height towards the corona, there is a general decreasing trend in $|\mathbf{j}|/|\mathbf{B}|$. At $y = 33$ there is a sharp increase corresponding to the X-point, where $|\mathbf{j}|$ increases and $|\mathbf{B}|$ decreases. Above the X-point, the curve

5.2 Modelling magnetic breakout with flux emergence

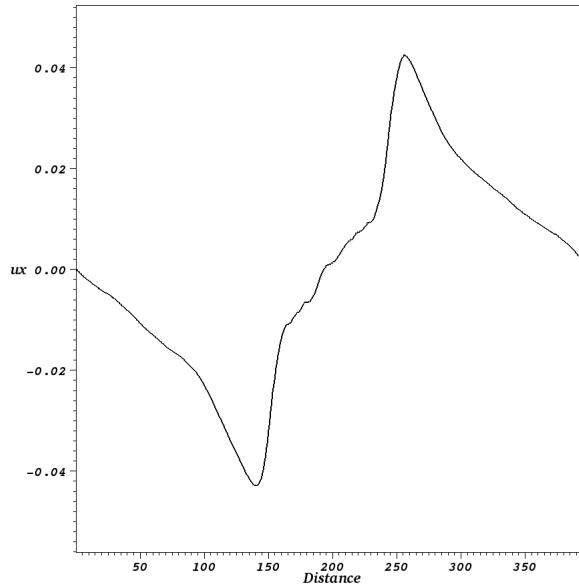


Figure 5.6: The horizontal speed at the photosphere at $t = 338$ for experiment (iv).

decreases to -2 on the \log_{10} scale and then fluctuates about -1.7. The magnetic field strength becomes weaker with height but is still, from Figure 5.8, nearly two orders of magnitude greater than the current density. Therefore, in the corona, with the exception of the X-point, the magnetic field is essentially potential. i.e. $\mathbf{j} \approx \mathbf{0}$. Below the corona, the field is not potential due to the presence of strong currents. As will be described in the following section, it is this region which contains vital physics that determines the final state of the system.

5.2.1.3 Three tubes

Now that the quadrupolar field has been created purely from flux emergence, the next step is to emerge a third flux tube up through the central arcade. The aim is to simulate the effect of shearing in the breakout model, without actually imposing any photospheric velocity shear. In the breakout model, although the central portion of the quadrupolar magnetic field is sheared, the arcades do not expand laterally at the base. This aids the reconnection necessary for flux rope eruption

5.2 Modelling magnetic breakout with flux emergence

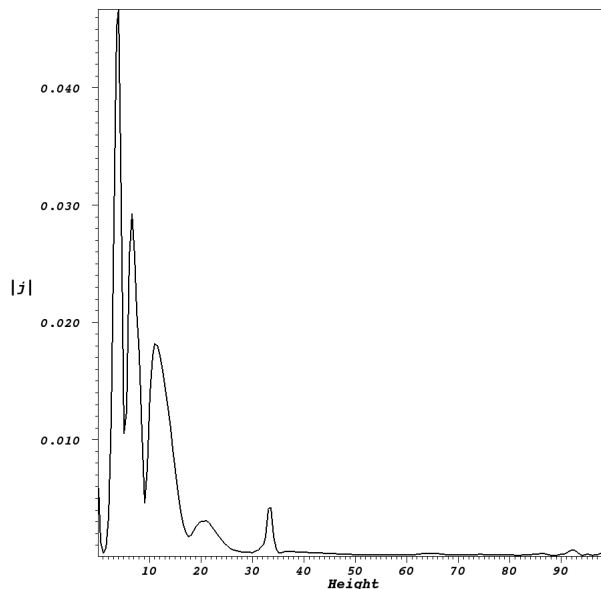


Figure 5.7: The variation of current density with height for experiment (ii) at time $t = 278$. The cut is taken through $x = 200$.

because the increased magnetic pressure can only force the sheared region to expand into the X-point, causing a current sheet to form there. In our flux emergence model, $\beta \approx 1$ at the photosphere. This means, as previously stated, that the plasma can move the field. When a third tube is inserted into the solar interior, below the central arcade of the quadrupole, it will rise and expand. The twist for the third tube is chosen so that it is in the opposite direction to that of the flanking tubes. This means that it will not reconnect with the side arcades upon emergence. When the third tube rises and emerges into the central arcade, it not only forces the field, already there, higher but it also interacts with the flanking tubes, causing them to move further apart. The scale of this movement is different for the different cases. For experiments (i) and (ii), axial separations of 20 and 40, the middle tube will make contact with the flanking tubes below the photosphere and drive them further apart. For experiment (iii) with a separation of 60, this interaction is less pronounced and in experiment (iv), with a separation

5.2 Modelling magnetic breakout with flux emergence

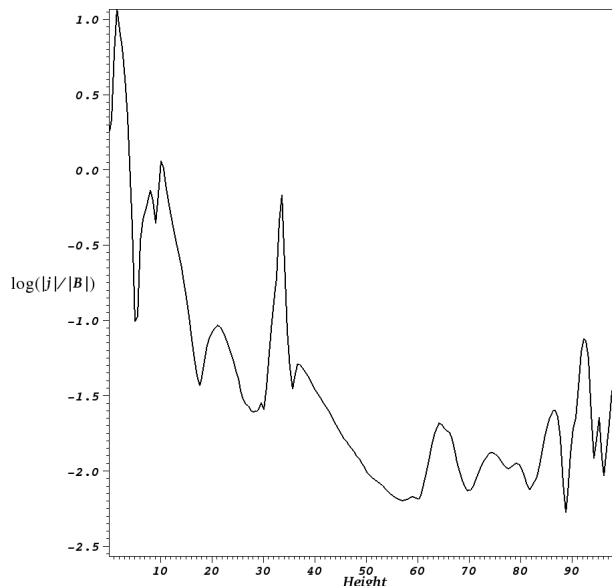


Figure 5.8: The logarithmic variation of $|j|/|B|$ with height for experiment (ii) at time $t = 278$. The cut is taken through $x = 200$.

of 80, the middle tube can reach the photosphere without its field making direct contact with the flanking tubes. However, when the middle tube emerges through the photosphere, it expands both upwards and laterally. The emerged field does indeed push up into the X-point and deforms it into a current sheet. Reconnection occurs here and transports flux to the side arcades exactly in the same manner as in the breakout model. However, the emerged field also expands laterally and pushes the side arcades further apart. In the breakout model, the reconnected flux is added to the side arcades, increasing their pressure and so compressing the middle arcade. This does not happen in our simulation because the side arcades have already been moved further apart. To study the effects of this sideways expansion, we shall now consider experiment (iv), where the interaction of the middle tube with the flanking tubes is expected to be the weakest out of the four experiments considered.

Figure 5.9 shows the quadrupolar configuration with the middle tube having

5.2 Modelling magnetic breakout with flux emergence

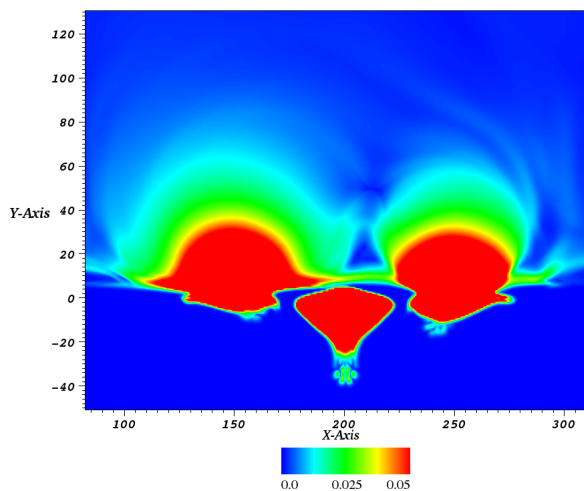


Figure 5.9: The quadrupolar configuration with the middle tube at the photosphere at time $t = 300$ for experiment (iv). The colourmap is of $|\mathbf{B}|$.

reached the photosphere. Just above the middle tube there is a band of field connecting the two flanking tubes. This is due to the presence of strong currents in this region, which allows reconnection to occur. Above this region (and in the corona) the X-point can be seen just off centre. Although the middle tube, for this case, has no direct contact with the flanking tubes, its expansion pushes the plasma away from it and increases the drift velocity of the flanking tubes. The velocity profile at the photosphere at time $t = 300$ is given in Figure 5.10. In this profile, the smaller peaks of the equilibrium flow can be seen.

We will now examine this experiment at a much later time when the middle tube has emerged and expanded. Figure 5.11 shows the configuration of the field at time $t = 450$. It is clear that the middle tube has not only expanded upward but also laterally. By comparison with Figure 5.9, the axes of the flanking tubes have each been pushed a distance of 20 further apart. The horizontal velocity at the photosphere is smaller in magnitude than it was at $t = 300$ but it is still larger than the equilibrium velocity (see Figure 5.6) produced by the quadrupole. The horizontal photospheric velocity at $t = 450$ is displayed in Figure 5.12. At the centre of this velocity profile there is a very small inflow. This, however, does not grow in time but flattens out. The horizontal photospheric velocity tends

5.2 Modelling magnetic breakout with flux emergence

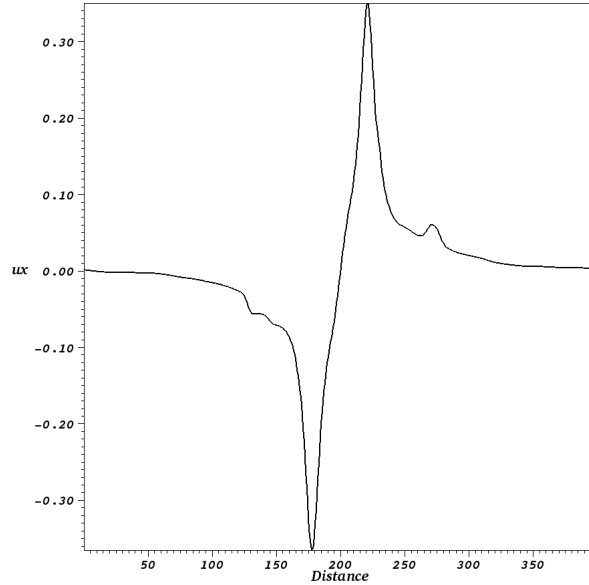


Figure 5.10: The horizontal speed profile at the photosphere at $t = 300$.

towards that for the equilibrium profile.

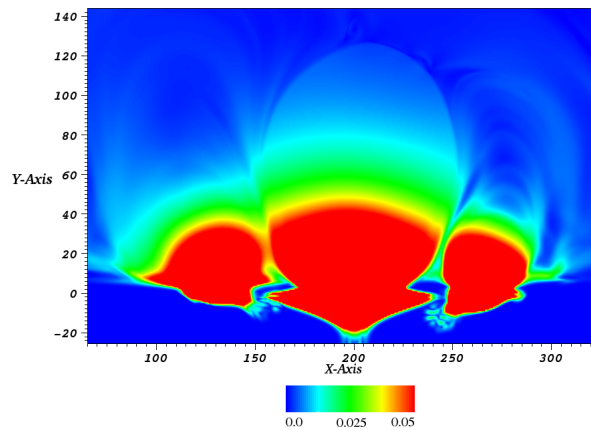


Figure 5.11: The magnetic field of experiment (iv) at time $t = 450$. The colourmap is of $|\mathbf{B}|$.

As the system expands laterally, the upward expansion has slowed down con-

5.2 Modelling magnetic breakout with flux emergence

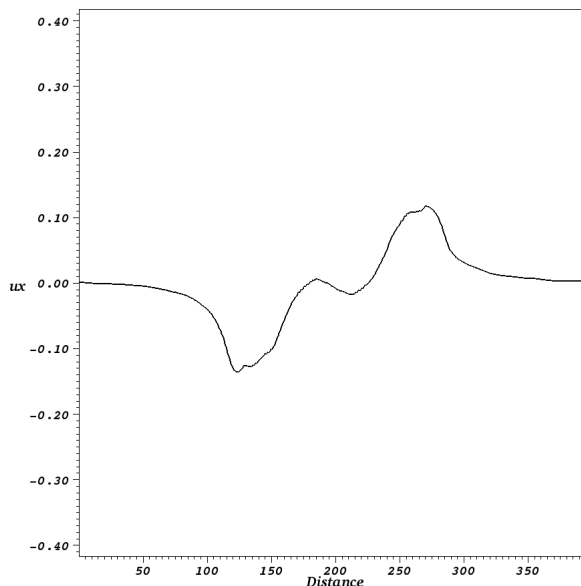


Figure 5.12: The horizontal speed profile at the photosphere at $t = 450$.

siderably. As the middle arcade expansion is driven by the emergence of a flux tube from the magnetic buoyancy instability, it will only expand for a limited time. Figure 5.13 displays the vertical velocities for $t = 360$ and $t = 450$ starting from the base of the photosphere ($y = 0$). This combination of a lateral expansion of the arcades and a limited upward expansion means that the field compression required to drive reconnection and expel a flux rope does not happen. In other words, this self-consistent flux emergence model of magnetic breakout does not produce the eruption of a flux rope.

5.2.2 Breakout summary

In this section we have attempted to model magnetic breakout in 2.5D in a self-consistent manner. Standard models, such as those described in the Introduction, have a quadrupolar field as their initial condition. This is dynamically altered by changing the boundary conditions to simulate shearing or flux emergence. Our model is based purely on multiple flux emergence, a common solar phenomenon,

5.2 Modelling magnetic breakout with flux emergence

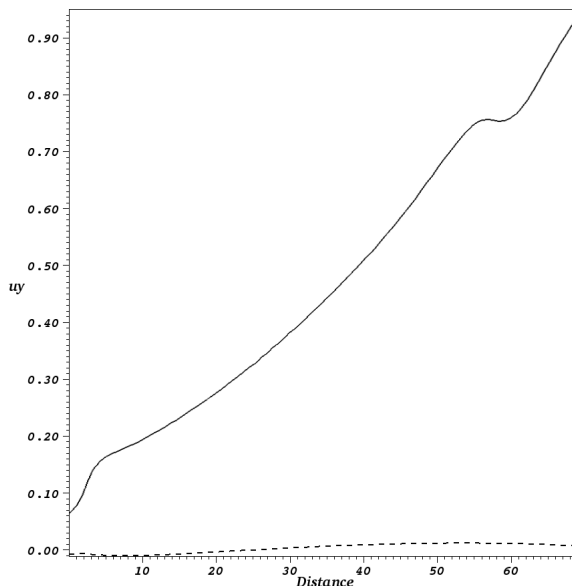


Figure 5.13: The solid curve shows the vertical velocity through the central arcade at $t = 360$. The dashed curve shows the same cut but at $t = 450$.

and the quadrupolar configuration is created as part of the emergence process. When one tube emerges and expands, followed by an identical tube that emerges into the first's field, the resulting equilibrium is a quadrupolar magnetic field. Experiments were performed to test the effect of the initial lateral separation of the two tubes. Each experiment results in a quadrupolar field where the system slowly expands. At the photosphere the sources gradually drift apart. The reason for this is that in our model, $\beta \approx 1$ at the photosphere. Therefore, if a flow is set up in the plasma, it can influence the magnetic field. Rather than artificially impose shearing motions, we increase the magnetic pressure in the central arcade by emerging more flux here. Once the first two tubes have produced a quadrupolar equilibrium, a third tube of opposite twist is emerged below the central arcade of the quadrupole. Although other flux tube combinations are possible, we make this choice since it produces the correct magnetic configuration required by the breakout model. As this tube emerges, it pushes upwards to deform the X-point

5.3 Eruptions from toroidal flux emergence

into a current sheet, as in the standard breakout scenario. The system, however, also expands laterally, pushing the quadrupolar arcades even further apart. The reason for this is, again, due to $\beta \approx 1$ at the photosphere and $\beta > 1$ in the solar interior. This expansion acts against the central arcade pinching off to form a flux rope. This is in agreement with the results obtained by [Zuccarello *et al.* \(2008\)](#). They also do not attain the necessary reconnection to pinch off a flux rope from the central arcade. The upward expansion is also finite as the emergence is driven from the magnetic buoyancy instability. This in combination with the lateral expansion of the system means that this self-consistent flux emergence model does not produce breakout.

What this study shows is that, in 2.5D, successful breakout requires intensive shearing and little or no lateral expansion, to build up the required magnetic pressure. In 2.5D, the flux tubes represent infinitely long straight tubes, with no kink caused by a density deficit. Shearing does occur when these tubes emerge. However, it is much smaller than in 3D tubes which are toroidal or kinked cylinders. The previous chapter demonstrated how atmospheric flux ropes can be produced from flux emergence. We shall now investigate how these ropes can erupt and if the eruption mechanism is related to magnetic breakout.

5.3 Eruptions from toroidal flux emergence

5.3.1 3D model

Upon moving from 2.5D to 3D, shear flows generated by emergence change from being dynamically insignificant to becoming major protagonists in the evolution of the system. In the standard breakout models, shearing is imposed to drive the system. In 3D flux emergence, it occurs naturally as part of the emergence process. In the previous chapter it was shown that this shearing, combined with inflows, can produce flux ropes. These ropes, however, remain trapped in the surrounding magnetic field of the emerged flux tube. In this section, we include a coronal field in the equilibrium. This will allow reconnection to occur with the emerging tube field and the escape of the flux rope.

5.3 Eruptions from toroidal flux emergence

We solve equations (2.9) to (2.13) and use the atmosphere of Chapter 4. The computational box has size $[50,50] \times [-50,50] \times [-20,85]$. The resolution is 256^3 . The top and bottom boundaries are closed and the sides are periodic. A horizontal magnetic field of the form

$$\mathbf{B} = B_c(z)(1, 0, 0),$$

is included in the corona. $B_c(z)$ is a hyperbolic tangent profile, so that the field is uniform in the corona and rapidly declines to zero at the base of the transition region. The strength of the coronal field is taken to be 0.01 ($\approx 13\text{G}$). The orientation of the coronal field is chosen so that it is almost antiparallel to the field of the emerging flux tube when they meet. A toroidal flux tube, of the form described in the previous chapter, is placed in the solar interior. It has the parameters $B_0 = 5$, $\alpha = 0.4$, $s_0 = 15$, $r_0 = 2.5$ and $z_0 = -25$. As in the previous chapter, the entire tube is made buoyant.

5.3.2 Eruption mechanisms

As mentioned previously, the pre-existing field of the corona is almost antiparallel to the field of the emerging tube. While the tube emerges, the arcade it forms first makes contact with the coronal field at $t \approx 33$. It pushes into the horizontal field and an arched current sheet forms between them. Reconnection occurs and the outer field lines of the arcade, that pass through the current sheet, change their connectivity and connect to the coronal field. The form of reconnection is fully 3D in the sense that it does not directly involve a null point. [Maclean *et al.* \(2009\)](#) also find this to be the case, with two clusters of null points forming at the sides of the emerging arcade rather than at the apex. They suggest that separator reconnection occurs in the current sheet between the tube and the corona. The effect, however, of this external reconnection is to weaken the tension of the coronal field. This becomes increasingly rapid with the loss of the restraining field, as in the breakout model. Evidence for this can be found by looking at the reconnection rate as it varies in time. The rate of reconnected flux is given by

$$\frac{d\Phi}{dt} = \int E_{\parallel} dl,$$

5.3 Eruptions from toroidal flux emergence

where the right hand side is the integrated parallel electric field along the reconnection line (Schindler (2006)). In 3D, however, no unique line exists at which the flux is split and reconnected (Hornig & Priest (2003)). Within the current sheet, every field line constantly changes its connection. Therefore, to estimate the reconnection rate between the flux tube arcade and the corona, in the simulation, we measure

$$\frac{d\Phi}{dt} \approx \max_{y=0}(E_{\parallel})\delta,$$

where $\max_{y=0}(E_{\parallel})$ is the maximum parallel electric field in the $y = 0$ plane (at the top of the arched current sheet) and δ is the thickness of the current sheet. This is a conservative estimate of the reconnection rate, taking the lengthscale of the integration to be the smallest dimension of the current sheet. This provides a lower bound on the reconnection rate. Figure 5.14 displays the increasing external reconnection rate during the expansion of the emerging arcade. Lynch *et al.* (2008) report that this behaviour is also found in the breakout model. Figure 5.15 shows the field line structure of the reconnected corona at $t = 70$. The coronal field lines are traced from opposite sides of the computational box (red for one side ($x = -50$), green for the other ($x = 50$)) at $z = 22$. A simulation magnetogram showing B_z is placed at the base of the photosphere ($z = 0$). After external reconnection the coronal field connects down into the main photospheric polarities (sunspots), leaving the centre free for the arcade to push on upwards.

With the production of a flux rope and the continued loss of the restraining coronal field through external reconnection, there is a catastrophic expulsion of the flux rope at $t \approx 91$. This description of the eruption is very similar to that of magnetic breakout. There are two important differences, however. The first is that in this flux emergence model, a null point does not play a crucial role in the external reconnection, as it does in breakout. The second is that there are no imposed flows in the flux emergence model. The Lorentz force of the emerging arcade naturally shears the magnetic field.

After the first eruption, the system does not settle into an equilibrium since the flux tube continues to emerge. The magnetic field in the corona is no longer horizontal due to reconnection during the first eruption. Shearing in the emerging arcade produces a second flux rope at a height $z \approx 34$ and time $t \approx 125$. The

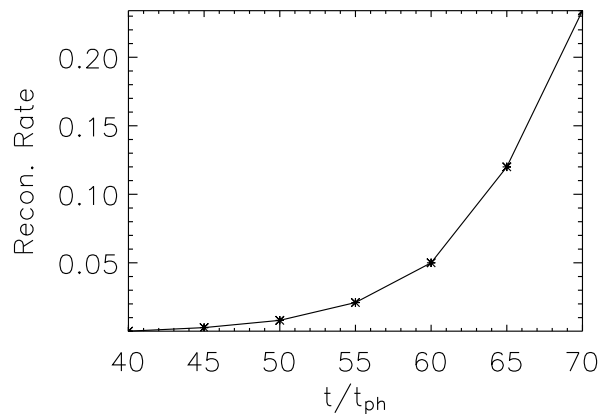


Figure 5.14: As the arcade of the emerging tube expands into the magnetized corona, the continued weakening of the overlying restraining field results in faster reconnection.

field line structure of the new flux rope and the corona at $t = 125$ is displayed in Figure 5.16. Coronal field lines (cyan) are traced from opposite sides of the box at $z = 40$. The red field line is the axis of the new flux rope. Some surrounding field lines (green) are traced from the main photospheric polarities, which are shown on a magnetogram at $z = 0$. This flux rope also erupts but the mechanism of the eruption is different to that of the first. The first eruption was of breakout-type where significant external reconnection (between the emerging arcade and the horizontal coronal field) played a crucial role in the expansion phase up to the eruption. As can be seen in Figure 5.16, however, the first eruption has cleared a path in the corona. External reconnection, therefore, does not feature as a key factor in the eruption of the second rope. This means that the trigger mechanism is not of breakout type and other candidates need to be considered. As mentioned in Chapter 3, Archontis & Török (2008) suggest that the eruption they found is driven mainly by runaway reconnection below the flux rope. This process has two important effects on the eruption. Firstly, the reconnection weakens the tension of the overlying field. Secondly, the upward reconnection jet carries the reconnected field lines to the erupting flux rope, adding poloidal flux to the rope (Vršnak (2008)). Both of these effects help the rope to accelerate further. This,

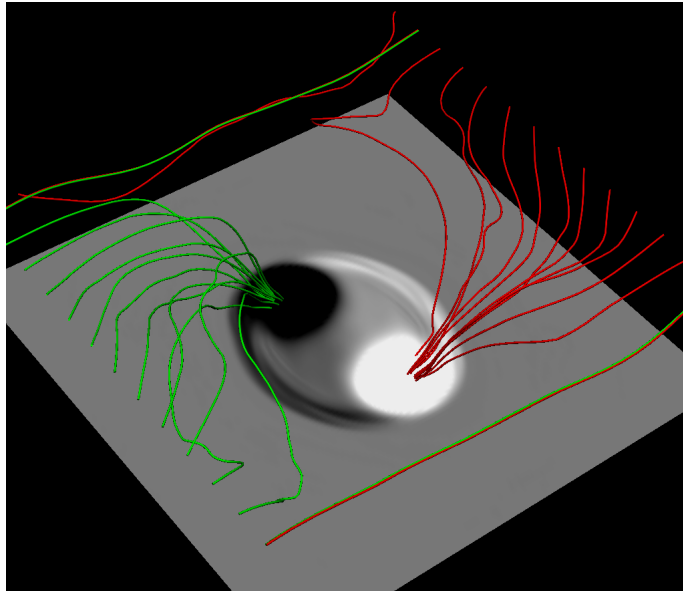


Figure 5.15: The field line structure of the corona after external reconnection. Red and green coronal lines are traced from opposite sides of the box, $x = -50$ and $x = 50$, respectively, at $z = 22$ and $t = 70$. A simulation magnetogram shows B_z at $z = 0$.

in turn, enhances the reconnection below and a runaway process ensues. For the second flux rope, this in combination with a weakened coronal field could drive the eruption. Another possibility, however, is that the newly formed rope becomes subject to an ideal MHD instability. A likely candidate is the torus instability (Bateman (1978), Kliem & Török (2006), Török & Kliem (2007)). A toroidal flux tube will become unstable against expansion if the external poloidal field decreases sufficiently rapidly in the direction of the major tube radius. Fan (2009) suggests that the expansion and acceleration of a flux rope is due to the continuous injection of twist, from the interior, via torsional Alfvén waves. Identifying a unique trigger mechanism is non-trivial as the conditions for several mechanisms can be satisfied simultaneously. In our simulation, the most likely candidate is runaway reconnection as the system never truly reaches an equilibrium to properly test for the torus instability.

The height-time profiles of the erupting ropes are displayed in Figure 5.17.

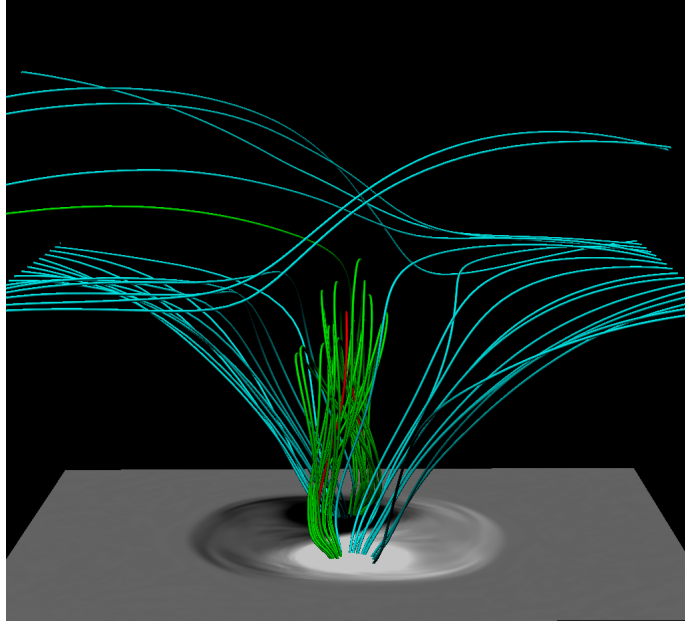


Figure 5.16: The field line configuration just before the eruption of the second rope. Coronal field lines (cyan) are traced from the sides of the box (along the y -axis) at $z = 40$. The red field line is the axis of the newly formed flux rope. Some field lines surrounding this are traced in green. A simulation magnetogram is displayed at $z = 0$.

These are estimated by tracking the O-point of the magnetic field in the $y = 0$ plane. The O-points also carry a ‘circular’ profile of dense plasma so we are confident that these accurately represent the erupting flux ropes. This is demonstrated in Figure 5.18, which shows the second erupting flux rope, with centre $(x, z) \approx (0, 55)$, at $t = 132$ by displaying the plasma density in the $y = 0$ plane. Field line arrows are also shown to indicate the direction of the magnetic field in that plane.

As mentioned earlier, the first flux rope forms at $t \approx 80$. It rises slowly until the eruption at $t \approx 91$. Here the gradient of the curve, in Figure 5.17, changes from (in non-dimensionalized units) 0.3 to 2. At $t = 115$ the centre of the rope has reached $z = 70$ and the gradient of the curve has increased to 2.8. We stop tracking the rope at this time since this is just before it comes into contact with the top boundary of the computational box. At $t \approx 125$ the second rope, that has

5.3 Eruptions from toroidal flux emergence

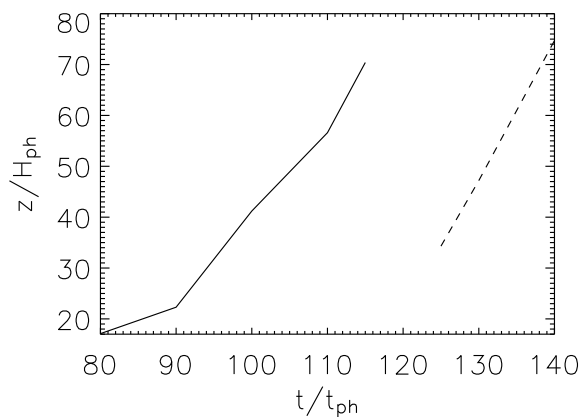


Figure 5.17: The height-time profiles for the two eruptions of the simulation. The curve for the first eruption is solid and the second is dashed.

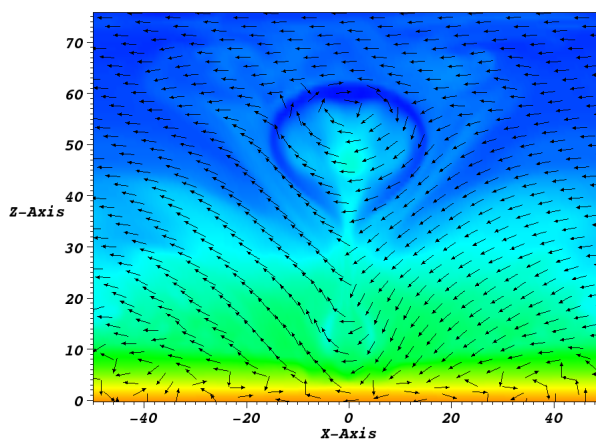


Figure 5.18: The second flux tube eruption of the simulation at $t = 132$. The colour map shows $\log \rho$ in the $y = 0$ plane with field line arrows to show the direction (but not the magnitude) of the magnetic field. Dense plasma can clearly be seen to be carried upwards into the corona with the erupting flux tube.

5.3 Eruptions from toroidal flux emergence

formed, is ejected upwards. Again, the rope is only tracked to just above $z = 70$ since beyond this the upper boundary begins to interfere with the rope's ascent.

The simulation is ended after the second eruption due to computational constraints. The plasma from the first two eruptions hits the top of the computational box, falls back down and interferes with the system. In theory, however, as long as the emergence process transports enough flux into the atmosphere and drives the necessary shearing, there should be more eruptions like the ones described.

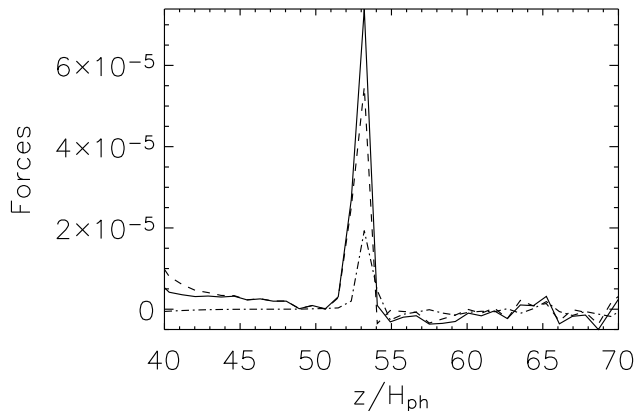


Figure 5.19: The vertical forces carrying the flux rope upwards at $t = 130$. The cut is taken at $(x, y) = (0, 0)$. Key: All forces (solid), $(\mathbf{j} \times \mathbf{B})_z$ (dash), $-\partial p/\partial z$ (dot-dash).

The ropes are carried upwards by a Lorentz force. Looking at the vertical forces, $(\mathbf{j} \times \mathbf{B})_z - \partial p/\partial z - \rho g > 0$ at the height of a flux tube during its rise. Figure 5.19 illustrates this by displaying the (non-dimensionalized) vertical forces as a function of height at $(x, y) = (0, 0)$ for the second flux rope eruption at $t = 130$. A positive upward force exists at the height of the flux rope and moves upwards in time with it. Of all the forces, it is the Lorentz force that dominates and is ultimately responsible for the rise of the ropes.

5.4 Summary

The basic properties of toroidal flux emergence, combined with the inclusion of a coronal magnetic field, allow for multiple CME-type eruptions to occur from the same active region. The coronal field we have used is orientated to maximize reconnection. This allows the flux ropes that form from self-consistent shearing to escape. Since in toroidal flux emergence, the region grows to a certain size and then stops, shear flows are able to continue to build up the pressure in the emerging arcade. This allows for the production of multiple flux ropes and, hence, multiple eruptions. In the model of [Archontis & Török \(2008\)](#), they use a cylindrical twisted flux tube with the standard exponential buoyancy profile. As this continually expands, they only observe one flux rope eruption.

The two eruptions produced in the simulation do not have identical initial conditions. The first can be considered to be of breakout-type. This is in relation to the breakout geometry rather than the eruption mechanism, since magnetic breakout is essentially a runaway reconnection model. External reconnection at the apex of the emerging arcade weakens the tension of the coronal field. With the expansion of the arcade, this reconnection becomes faster through time. Shearing, which occurs as part of the emergence process, induces internal reconnection in the arcade and produces a flux rope. The continued emergence in combination with the removal of the overlying coronal field eventually results in the expulsion of the flux rope. After the first eruption, continued emergence and, therefore, shearing results in the formation of a second flux rope. This also erupts but the trigger mechanism cannot be directly linked to the breakout model, as with the first eruption. Due to the reconnection of the first eruption with the corona, a weakened coronal field exists above the second rope when it forms. Possible trigger mechanisms, such as runaway reconnection and the torus instability, have been suggested. However, it is possible that the trigger for the second eruption is, in fact, a combination of such mechanisms.

At the start of this chapter, we tried and failed to produce magnetic breakout self-consistently from flux emergence alone. For a successful eruption in the breakout model, little or no lateral expansion and strong shearing are required. Moving to the 3D toroidal model, all of these conditions occur self-consistently

5.4 Summary

from the emergence process. The result is multiple eruptions from the same active region with no imposed motions.

Chapter 6

Signatures of flux emergence

6.1 Introduction

Active regions form from the emergence of magnetic flux tubes. In this thesis (and in most of the theoretical flux emergence literature, see Chapter 3) we have used a single monolithic flux tube to model the emerging region. In reality, however, active regions can be areas of multiple flux emergence. [Harra *et al.* \(2010\)](#) present an observation of the emergence of a bipole in one of the sunspots of a large active region. Although the origin of this bipole is not known (i.e. whether it originates from the magnetic field of the existing active region or whether it is separate), it does produce signatures of an emerging twisted flux tube (e.g. [Archontis & Hood \(2010\)](#)). An understanding of the signatures of flux emergence is vital for the correct identification of emerging flux tubes, especially in cases that are not as clear as [Harra *et al.* \(2010\)](#). One such example is a set of observations by [Okamoto *et al.* \(2008\)](#) and [Okamoto *et al.* \(2009\)](#) (hereafter referred to as O1 and O2, respectively) of NOAA AR 10953 with the Solar Optical Telescope (SOT) on board Hinode. Part of this region contains a prominence lying along the polarity inversion line (PIL) of a magnetic arcade. O1 and O2 suggest that the prominence is formed/maintained by the full emergence of a twisted flux rope along the PIL. They produce a cartoon model of a twisted cylinder rising as a whole to the corona. This idea is based on two main signatures that are observed in photospheric vector magnetograms. The first is the ‘sliding doors’ effect where the opposite polarities of the arcade appear to expand laterally

a certain distance before beginning to narrow. The second signature is that the orientation of horizontal magnetic fields at the PIL changes from a normal-polarity configuration to an inverse one. i.e. vectors pointing across the PIL in one direction gradually change to pointing in the other direction.

In this chapter, we assume a flux emergence interpretation and model the emergence of a twisted cylinder into an overlying arcade. We produce magnetograms to compare with the observations and to determine the relevance of the two signatures mentioned above.

The main results of this chapter have been published in

Simulating the ‘sliding doors’ effect through magnetic flux emergence, MacTaggart & Hood 2010, Astrophysical Journal Letters, 716, L219

6.2 Model setup

We model the emergence of a twisted flux tube into an overlying arcade using a 3D MHD simulation. We solve equations (2.9) to (2.13) and use the atmosphere model of Chapter 4. The side boundaries of the computational domain are periodic and the top and bottom are closed. The domain has size $[-60,60] \times [-60,60] \times [-20,80]$ and resolution $128^2 \times 256$. The overlying magnetic arcade is part of a larger quadrupolar structure that is formed from the interaction of two emerging flux tubes and was discussed in the previous chapter. This was found to produce the best numerical arcade equilibrium that is anchored in the solar interior. It is field-free in this layer apart from, of course, at the legs. We choose the stringent condition of a field-free solar interior so that no reconnection occurs when the flux tube is inserted initially. This is to prevent reconnection flows in the solar interior that will disguise the effects of the interaction of the flux tube with the arcade. As we are focussing on the photosphere, the X-line of the quadrupolar field, which sits above the arcade in the corona, can be ignored. The lateral expansion, described in the previous chapter, is negligible since this is a 3D model and allows flows, that were previously constrained to two dimensions, an extra dimension to flow in.

With the equilibrium set up, a uniformly twisted magnetic cylinder is placed in the solar interior. We choose a weakly twisted flux tube of $1/(10\pi)$ turns per unit length of the axis. The orientation of the twist is chosen to inhibit reconnection with the overlying arcade. i.e. when the tube comes into contact with the arcade, their respective fields are not antiparallel. The tube is made buoyant with respect to its surrounding plasma in the solar interior. To encourage an Ω -loop to form, the density deficit is multiplied by the standard exponential function of the form $\exp(-y^2/\lambda^2)$, where y is the distance along the tube axis and λ is an adjustable parameter. Here we take $\lambda = 40$. This is a large value (compared with previous simulations) in order to model the emergence of a long tube. If there was no kink in the tube (i.e. $\lambda = \infty$) then the flux rope axis would not rise above the base of the photosphere in this model. A visualization of the initial condition is displayed in Figure 6.2.

The flux rope in the solar interior is initially placed at $(x, 0, z) = (0, 0, -15)$, has an axial field strength of $|\mathbf{B}| = 8$ and a radius of 2.5. When the tube rises to just below the photosphere and begins to interact with the arcade, its field strength has reduced to approximately 3/2 times that of the arcade field strength.

6.3 First signature: ‘Sliding doors’

In the cartoon model of O1, the ‘sliding doors’ effect is produced by the lateral motions of the arcade polarities as a twisted flux rope passes through the base of the photosphere as a ‘solid’ cylinder. The ‘sliding doors’ effect is also present in our model, however, the mechanism behind it is different. One important aspect which is not present in the cartoon is that the emerging flux rope has a B_z profile of its own and so will have an imprint on the magnetograms. In our model, the ‘sliding doors’ effect is produced by the rise, expansion and emergence of the flux tube. Figure 6.3 displays slices in the $(x, 0, z)$ plane at four different times. Each slice portrays regions of B_z (colours and contours) and (B_x, B_z) arrows to indicate the position of the tube axis.

The first phase of the ‘sliding doors’ effect is the rise of the flux tube to the photosphere. In the solar interior, the flux tube follows a field-free path. It only

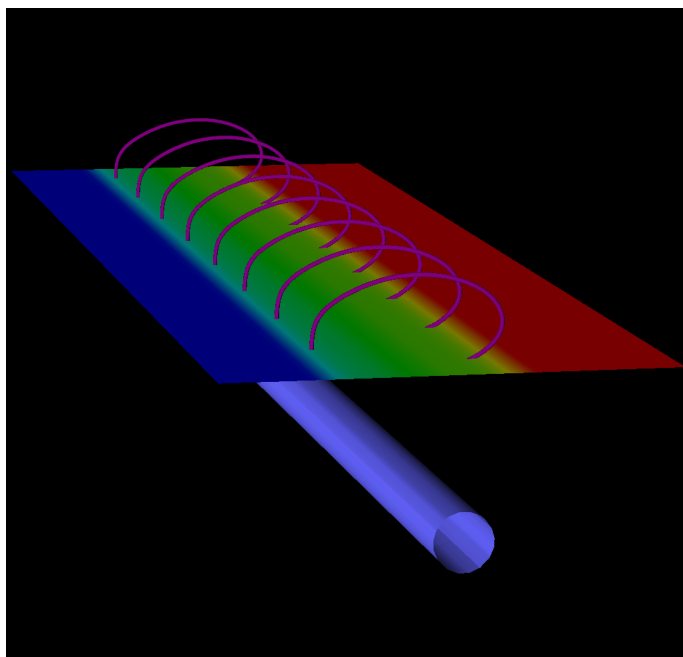


Figure 6.1: The initial condition. The magnetogram of B_z at the base of the photosphere shows the opposite polarities of the arcade (blue - negative, red - positive and green - horizontal field). Some of the arcade field lines are traced in purple from the base of the photosphere. An isosurface ($|\mathbf{B}| = 3$) shows the initial location of the twisted flux rope in the solar interior.

comes into contact with the arcade, which is anchored in the solar interior, just below the photosphere. As the flux tube rises, it expands. Due to its dominant pressure, the flux tube pushes the opposite polarities of the overlying arcade apart. In the cartoon model, this would be in the broadening phase of the ‘sliding doors’ effect. However, this is not the case in our model as the flux tube continues to push upward and so contributes to the B_z map seen on magnetograms. Figure 6.3 (a) shows the interaction of the flux rope with the overlying arcade at $t = 38$. Here the tube has pushed the arcade aside and its own magnetic field has risen above $z = 0$ and into the photosphere. The tube axis is still below $z = 0$.

The second phase of the ‘sliding doors’ effect is the lateral expansion of the tube in the photosphere. Since the photosphere is stable to buoyancy, the flux

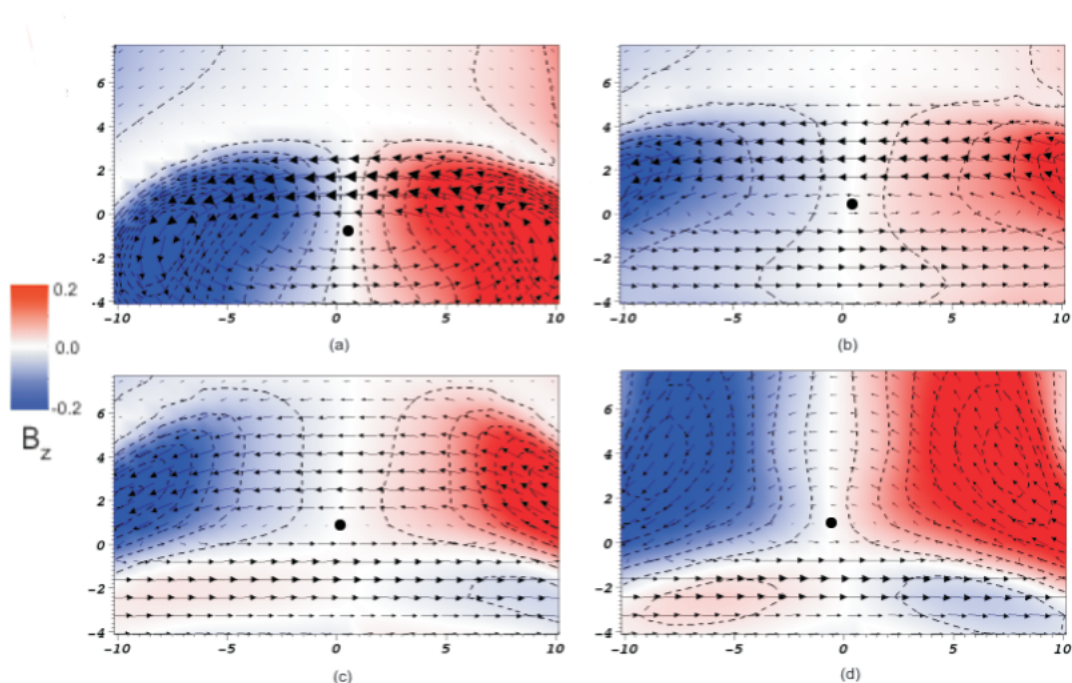


Figure 6.2: Slices in the $(x, 0, z)$ plane. Dashed contours and colours identify regions of strong (relative) B_z . (B_x, B_z) arrows and a black dot indicate the position of the flux tube axis. Each slice represents a different time: (a) $t = 38$, (b) $t = 48$, (c) $t = 58$ and (d) $t = 78$.

rope cannot continue rising due to buoyancy (the presence of the top of the flux tube in the photospheric layer is due to momentum carrying it there). Instead it expands laterally. Figure 6.3 (b) shows this expansion at $t = 48$. The contours in (b) are further apart than those in (a). Hence, the region of weak B_z at the centre of the emerging tube (and hence also at the PIL) is broader. This broadening is the first part of the ‘sliding doors’ effect. Figure 6.3 (b) also shows that the axis of the flux tube is now above the base of the photosphere $z = 0$. Although, as mentioned before, the photosphere is stable to buoyancy, magnetic field from the solar interior still rises upwards and can push through $z = 0$.

With the continued lateral expansion in the photosphere combined with the buoyant rise of flux from below, the emerging flux tube eventually becomes sub-

6.3 First signature: ‘Sliding doors’

ject to the magnetic buoyancy instability. Figure 6.3 (c) displays the initial stage of this at $t = 58$. Here the two main regions of B_z have risen upwards. As the field emerges into the atmosphere, the B_z profile becomes stronger in the central region (at the PIL). Figure 6.3 (d) shows the emergence at the later time of $t = 78$. Now the tube’s field has penetrated far into the atmosphere and the contours of B_z near the base of the photosphere ($z = 0$) have moved closer together. This narrowing is the second part of the ‘sliding doors’ effect. A time-slice of this broadening and narrowing at $z = 0$ is shown in Figure 6.3. In this magnetogram series, the B_z field of the flux tube and the arcade appear ‘merged’ and cannot be distinguished apart from some small areas in the blue region.

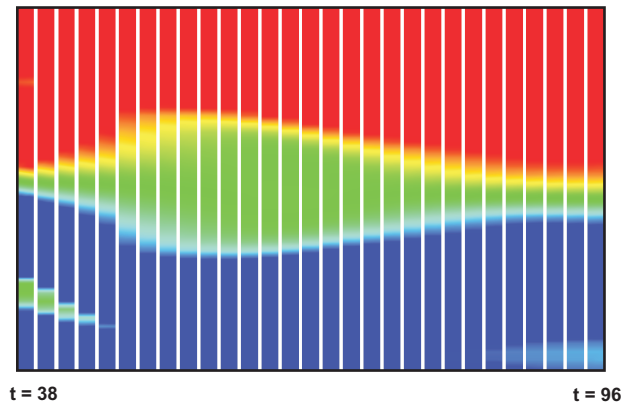


Figure 6.3: Time-slice image showing the ‘sliding doors’ effect. The slices from the simulation are taken at $y = 0$ and from $x = -20$ to $x = 20$. The time difference between the slices is 2 in non-dimensional units. Colours are as indicated in Figure 1.

In short, the ‘sliding doors’ effect is produced from the expansion of the flux rope at the photosphere and its subsequent emergence, via the magnetic buoyancy instability, into the atmosphere. Note that the axis of the flux tube does not continue rising but becomes trapped at a height of $z \approx 1$.

6.4 Second signature: Horizontal vector directions

In principle, it is possible to explain the broadening and narrowing motions discussed in the previous section without recourse to flux tube emergence. However, this would be to neglect the second signature of the change in orientation of the horizontal photospheric magnetic field vectors. Figure 6.4 shows the time evolution of the angle of the horizontal field against the PIL for two positions along the tube length. The graph should be read such that if the PIL faces north (0°), west is -90° and east is 90° .

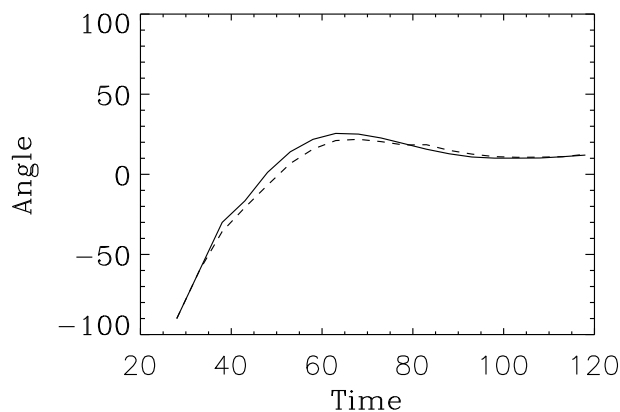


Figure 6.4: Time evolution of the horizontal field vector against the PIL for two locations along the tube length.
Key: $y = 0$ (solid), $y = 10$ (dash)

Due to the large value chosen for λ , the Ω -shape is not greatly pronounced. This can account for the similar profiles of the two curves in Figure 6.4. However, as mentioned earlier, the kink is necessary for the drainage of plasma and, hence, the rise of the flux tube axis above the base of the photosphere. Figure 6.4 clearly shows the switch in vector direction from one side of the PIL to the other. Both curves move through 90° and then reach a maximum angle on the other side of the PIL before appearing to settle at a smaller, but positive, angle. This information is presented in O1 in Figures (d1)-(d6) and reproduced here in

Figure 6.5. Although the angles at various positions along the PIL vary due to convection, it could be argued that for large sections of the observed PIL, the angles follow a profile similar to that in Figure 6.4. This rotation of the horizontal field vector does require the axis to rise above $z = 0$, even though it is only by a small amount. i.e. the axis does not rise to coronal heights. The top of the tube, however, is able to reach coronal heights due to the magnetic buoyancy instability.

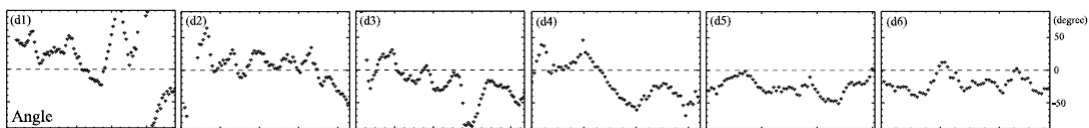


Figure 6.5: The angles between the horizontal magnetic fields and the PIL. Taken from O1, Figures (d1)-(d6).

6.5 Other signatures

The two signatures discussed in this chapter have been used by O1 and O2 to argue that they are observing the emergence of a twisted flux tube. These signatures are found in the model. However, the underlying physical mechanisms are different from those proposed by O1 and O2. The model produces other signatures to those discussed and, importantly, these can be checked in the observations.

6.5.1 Unsigned flux

If a flux rope rises to the photosphere, even if it does not fully emerge into the corona, there must be an increase in the unsigned vertical flux in the photosphere,

$$\Phi = \int \int |B_z| dx dy,$$

where the integral is evaluated in the plane of the magnetogram. For the model, the evolution of the vertical flux for negative polarities through time is displayed in Figure 6.6. The reason for only considering negative polarities is to facilitate a better comparison with observations since the positive polarities in NOAA AR

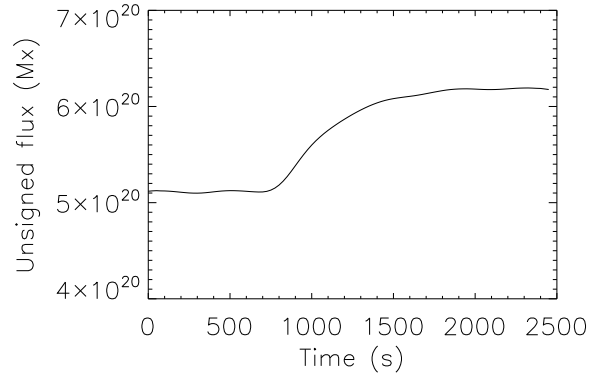


Figure 6.6: The evolution of the unsigned vertical flux from negative polarities for the duration of the simulation.

10953 are diffuse and difficult to track. In principle, however, either polarity could be chosen. Due to computational constraints, the dimensions of the flux systems in the model are smaller than those of NOAA AR 10953. This is common to most current dynamic simulations of the emergence of magnetic flux tubes (see Chapter 2). Hence, the absolute values on the axes of Figure 6.6 cannot be compared directly with the values from observations. However, it is the trend of the curve showing how the amount of unsigned flux changes in time that is important. It is now possible to calculate the flux as a function of time from the observations and compare the trend to that from the model.

6.5.2 Shear flows

One universal feature of flux emergence simulations that use a twisted flux tube for the initial magnetic field is that, upon emergence, shear flows develop along the PIL of the emerging region. These flows are driven by the Lorentz force and the underlying mechanism has been described in Chapter 4. In simulations they have been shown to be important for driving large-scale eruptions (see Chapter 5). Fang *et al.* (2010) include the effects of convective motions in their emerging flux tube simulation and find shearing flows of magnitudes up to 1.5 km/s on either side of the PIL. As shown in Chapter 4, changing the parameters of the initial condition (e.g. field strength) can alter the strength of the shear flows.

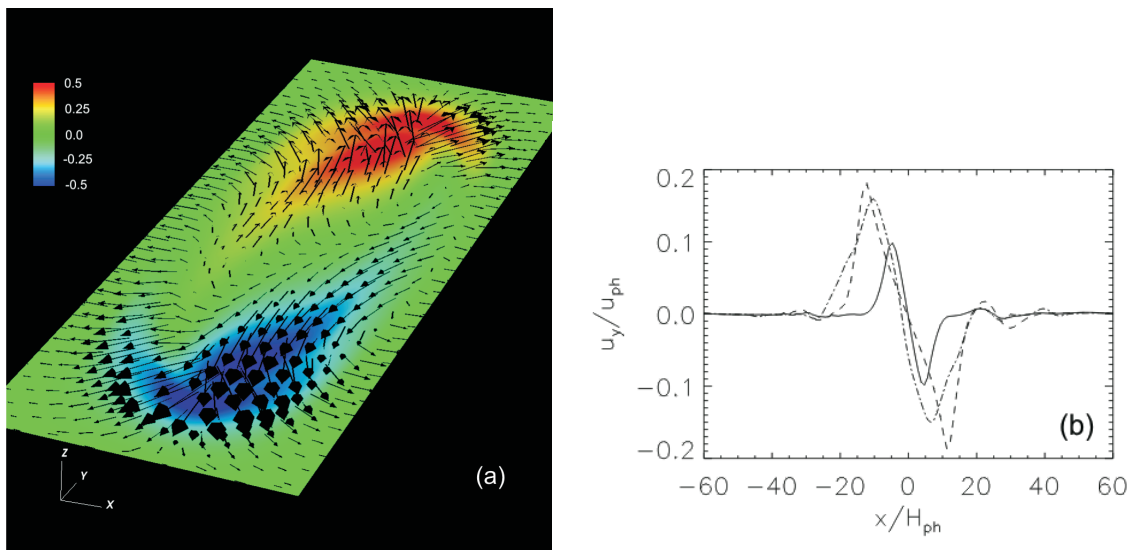


Figure 6.7: Shear flows at the PIL. (a) displays a slice, showing u_y at $t = 1050$ s, taken at the base of the photosphere in the model. The arrows are horizontal velocity vectors. The colour bar shows non-dimensional speed. (b) shows the shear profiles of a horizontal cut across the PIL at three different times. Key: $t = 900$ s (solid), $t = 1225$ s (single dash) and $t = 2200$ s (dot dash).

However, they are generally found to be a sizeable fraction of the photospheric sound speed ($u_{\text{ph}} \approx 6.8$ km/s).

O2 claim that they do not find any shear flows at the PIL, only granular flows. The body of evidence, however, of shear flows from emergence simulations suggests that they should be present in emerging solar active regions and are therefore a signature of flux emergence. Since the model (and others) predict their existence for twisted flux rope emergence, it is worth re-examining the observations for signs of them.

Figure 6.7 displays the shear flows that develop in the model in two ways. Figure 6.7 (a) shows a slice taken at the base of the photosphere in the model (the same slice used for calculation of the other signatures). The slice displays a colour map of speed u_y (the tube axis lies along the y -direction) and horizontal velocity vectors (u_x, u_y). This image is at a time of 1050 s. Comparing this with

the scale of Figure 6.6, it shows the early stage of the emergence of the flux tube. As the opposite polarities of the tube (blue and red regions in Figure 6.7 (a)) drift apart during emergence, a shear flow develops along the PIL. Taking a cut across the PIL at the centre of this slice, Figure 6.7 (b) shows the shear profile at three different times, during the ‘sliding doors’ effect. The solid curve, taken at $t = 900$ s, shows the shear flow across the PIL at the start of the broadening phase. It has a maximum speed of 0.68 km/s. The single dashed curve is at $t = 1225$ s and the broadening phase is nearly at its widest. The corresponding maximum speed is 1.29 km/s. Later, during the narrowing phase at $t = 2200$ s, the dot-dash curve shows a slightly reduced shear profile to the previous one, with a maximum speed of 1.09 km/s. Although there is some variation in the magnitude of the shear flows with time, the simulation shows that during the ‘sliding doors’ phase (i.e. the emergence phase), a robust shear profile exists.

6.6 Summary

In this chapter we have constructed a model to study the interaction of an emerging twisted flux tube with an overlying arcade. The motivation for this is based on observations of NOAA AR 10953, by O1 and O2, which they interpret as an example of the emergence of a twisted flux tube. This interpretation is based on two photospheric signatures. The first is the ‘sliding doors’ effect, the broadening and narrowing of the opposite polarities of the vertical magnetic field. The second is the change of direction of the horizontal magnetic field vectors, rotating from pointing in one direction across the PIL to pointing in the opposite direction. These signatures are found in the model but their explanations are not completely compatible with those of O1 and O2. The ‘sliding doors’ effect is found, in the model, to be caused by various stages of the emergence of the flux tube and not by the movement of the arcade as it is pushed aside. For the second signature, the axis of the tube, in the model, rises above the base of the photosphere and so the horizontal magnetic field vectors rotate to point across the PIL in the opposite direction. The axis, however, does not rise to the corona, as in the cartoon model of O1 and O2, but remains trapped in the photosphere.

So far, the results from the model can be used to argue both for and against the interpretation that a twisted flux rope emerges. The model, however, produces other signatures that can be tested in the observations. Since the model is of an emerging twisted flux tube, the discovery of these signatures in the observations would add considerable weight to the original interpretation of O1 and O2. The two extra signatures highlighted in this chapter are an increase in the unsigned flux at the photosphere and the presence of shear flows at the PIL.

Chapter 7

Final thoughts

In this thesis, we have explored many aspects of theoretical magnetic flux emergence through numerical simulations. Rather than repeat the contents of all the chapters here (which all have summaries with the exception of the literature review of Chapter 3), we shall discuss some trends that have appeared in the subject. We shall conclude by speculating what future directions the subject will take.

7.1 Trends and fashions

In applied mathematics and theoretical physics, the philosophy of modelling is to solve the simplest problem first, gain a deep understanding of this and then add further complexity. In this thesis, we have presented a ‘simple’ model for magnetic flux emergence. By this we mean that the plasma is modelled using only resistive MHD. This theory has allowed us (and others) to study a plethora of complex dynamical behaviour associated with flux emergence, resulting in real progress in the field. The next stage in the modelling process is to include extra physics, such as thermal conduction and radiative transfer. Ideally, these should be added one by one, and their individual effects studied in detail. In recent years, however, the trend has been to include as much physics as possible, namely resistive MHD with thermal conduction, convection, radiative transfer and partial ionization. Part of the reason for this is to produce synthetic observations to compare with actual observations. However, the primary goal of modelling is to understand the basic

physical processes behind flux emergence and models that include all of the extra physics mentioned above are difficult to interpret. It seems, however, that this trend is here to stay for the near future. Rather alarmingly, the term ‘realistic’ is generally attached to flux emergence simulations that use MHD plus the extra non-adiabatic thermodynamic terms. This has led to a distrust of simpler models. An example of this is available in [Lites *et al.* \(2010\)](#). Here they state,

“It should be noted that simulations of emergence of significantly twisted flux ([Manchester \(2007\)](#)) into the atmosphere produces shear flows parallel to the PIL that are driven by the Lorentz force. However, such flows are not a dominant feature of the more realistic simulations of [Cheung *et al.* \(2008\)](#) that embrace the details of the small-scale magneto-convection in the upper convection zone and photosphere.”

Here, shear flows found in a ‘simple’ model are dismissed because they are not present in a more ‘realistic’ one. The problem with this is that the model of [Cheung *et al.* \(2008\)](#) only extends to the photosphere. This means that the field cannot emerge and expand into the atmosphere and, hence, build up the Lorentz force required to drive shearing (see Chapter 4). This is not a criticism of [Cheung *et al.* \(2008\)](#) or, indeed, of the inclusion of non-adiabatic terms in the model. Rather it is a criticism of the misleading use of the label ‘realistic’. All models have advantages and limitations and the use of adjectives like ‘realistic’ is unhealthy for any scientific discipline (especially in light of Chapter 1). A more appropriate name for such models would be ‘detailed thermodynamic models’.

The MHD models of this thesis have shown that there is still much to gain from simpler models. An important example of this is the main result of Chapter 4. For years, researchers had used the same initial condition for a flux tube, namely, a twisted cylinder placed near the base of the photosphere. As described in Chapter 4, the axes of such tubes are unable to emerge into the upper atmosphere. This led to the belief that the axes of flux tubes could not emerge and resulted in the criticism of flux emergence simulations from certain quarters. It was not until [Hood *et al.* \(2009\)](#) suggested a different geometry for the initial flux tube that progress was made. We were able to show that this change of geometry enables sufficient draining to occur that allows the axis to fully emerge. With the inclusion of extra physics, this picture will become more complex. With a

relatively simple model, however, we have been able to isolate the key physical process.

7.2 Future directions

As stated in the previous section, the inclusion of more detailed thermodynamic terms in the energy equation will play an important role in flux emergence modelling in the near future. The relationship between emerging flux tubes and convection will be an interesting problem. This has started to be addressed by models that include convection (e.g. [Tortosa-Andreu & Moreno-Insertis \(2009\)](#)). Active regions are often areas of multiple flux emergence. As flux tubes are known to distort convection cells, it would be interesting to study how an active region sunspot is deformed by an emerging flux tube beneath it. An example of this is in [Harra *et al.* \(2010\)](#) where a flux tube emerges into the diffuse sunspot of a bipolar active region. The other sunspot is robust and not deformed by convection. It would be interesting to quantify how much of an effect the second flux tube has in deforming the sunspot above it. This problem is linked to that of the nature of the rising magnetic field in the convection zone.

One problem that currently faces all flux emergence simulations is that the evolution of the emerging tube occurs too quickly. There are several factors that may contribute to this. It is likely that the initial magnetic field is made too buoyant and so rises too quickly. The inclusion of extra physics may also affect the condition for the magnetic buoyancy instability. Although the time scale problem precludes direct comparison with observation time scales, it is believed that the underlying processes of flux emergence are described correctly.

Chapter 5 demonstrated the potential of flux emergence as a driver for multiple CMEs. Future study is likely to focus on such models with efforts concentrating on two important aspects of the eruptions. One is to extend the simulation domain to track the evolution of the erupting flux rope. The other is to study signatures that can be used to inform the prediction of CMEs.

As stated at the start of this thesis, the emergence period is only a small fraction of the lifetime of an active region. There are still many other problems related to flux emergence that need to be addressed. From the formation of flux

7.2 Future directions

tubes at the tachocline and their rise through the convection zone to the life and eventual decay of active regions. All these are linked via the solar dynamo. To understand this circular problem, each link must be understood in detail. This thesis represents an attempt to shed more light on the short but important link of magnetic flux emergence.

References

- ACHESON, D.J. (1979). Instability by magnetic buoyancy. *Solar Physics*, **62**, 23. [7](#), [12](#), [44](#)
- ANTIOCHOS, S.K., DEVORE, C.R. & KLIMCHUK, J.A. (1999). A Model for Solar Coronal Mass Ejections. *Astrophysical Journal*, **510**, 485. [79](#), [80](#), [82](#), [86](#)
- ARBER, T.D., LONGBOTTOM, A.W., GERRARD, C.L. & MILNE, A.M. (2001). A Staggered Grid, Lagrangian-Eulerian Remap Code for 3-D MHD Simulations. *Journal of Computational Physics*, **171**, 151. [15](#), [16](#), [27](#), [29](#)
- ARCHONTIS, V. & HOOD, A.W. (2010). Flux emergence and coronal eruption. *Astronomy & Astrophysics*, **514**, A56. [47](#), [105](#)
- ARCHONTIS, V. & TÖRÖK, T. (2008). Eruption of magnetic flux ropes during flux emergence. *Astronomy & Astrophysics*, **492**, L35. [15](#), [46](#), [47](#), [98](#), [103](#)
- ARCHONTIS, V., MORENO-INSERTIS, F., GALSGAARD, K., HOOD, A. & O'SHEA, E. (2004). Emergence of magnetic flux from the convection zone into the corona. *Astronomy & Astrophysics*, **426**, 1047. [12](#), [43](#), [44](#), [45](#), [47](#), [48](#), [51](#)
- ARCHONTIS, V., HOOD, A.W. & BRADY, C. (2007). Emergence and interaction of twisted flux tubes in the Sun. *Astronomy & Astrophysics*, **466**, 367. [39](#), [41](#), [83](#)
- BATEMAN, G. (1978). *MHD instabilities*. MIT Press. [99](#)
- BENZ, A.O. (1993). *Plasma astrophysics: Kinetic processes in solar and stellar coronae*. Kluwer Academic Publishers. [4](#)

REFERENCES

- BODENHEIMER, P., LAUGHLIN, G.P., RÓZYCZKA, M. & YORKE, H.W. (2007). *Numerical Methods in Astrophysics: An Introduction*. Taylor & Francis Group. 31
- BOYD, T.J.M. & SANDERSON, J.J. (1969). *Plasma dynamics*. London, Nelson, Series: Applications of mathematics. 4
- BOYD, T.J.M. & SANDERSON, J.J. (2003). *The Physics of Plasmas*. Cambridge University Press. 5, 6
- BRAGINSKII, S.I. (1965). Transport Processes in a Plasma. *Reviews of Plasma Physics*, **1**, 205. 4
- CARGILL, P.J., SCHMIDT, J., SPICER, D.S. & ZALESK, S.T. (2000). Magnetic structure of overexpanding coronal mass ejections: Numerical models. *Journal of Geophysical Research*, **105**, 7509. 15
- CARROLL, B.W. & OSTLIE, D.A. (1996). *An Introduction to Modern Astrophysics*. Addison-Wesley Publishing. viii, 2
- CHEUNG, M.C.M., SCHÜSSLER, M. & MORENO-INSERTIS, F. (2007). Magnetic flux emergence in granular convection: radiative MHD simulations and observational signatures. *Astronomy & Astrophysics*, **467**, 703. 47, 48
- CHEUNG, M.C.M., SCHÜSSLER, M., TARBELL, T.D. & TITLE, A.M. (2008). Solar Surface Emerging Flux Regions: A Comparative Study of Radiative MHD Modeling and Hinode SOT Observations. *Astrophysical Journal*, **687**, 1373. 118
- COWLING, T.G. (1946). The growth and decay of the sunspot magnetic field. *MNRAS*, **106**, 218. 2
- DENDY, R. (1993). *Plasma Physics: an Introductory Course*. Cambridge University Press. 4
- DEVORE, C.R. & ANTIOCHOS, S.K. (2008). Homologous Confined Filament Eruptions via Magnetic Breakout. *Astrophysical Journal*, **680**, 740. 80

REFERENCES

- EMONET, T. & MORENO-INSERTIS, F. (1998). The Physics of Twisted Magnetic Tubes Rising in a Stratified Medium: Two-Dimensional Results. *Astrophysical Journal*, **492**, 804. [38](#)
- FAN, Y. (2001). The Emergence of a Twisted Ω -Tube into the Solar Atmosphere. *Astrophysical Journal Letters*, **554**, L111. [41](#), [42](#), [43](#), [44](#), [45](#), [46](#), [48](#), [51](#), [53](#), [57](#)
- FAN, Y. (2009). The Emergence of a Twisted Flux Tube into the Solar Atmosphere: Sunspot Rotations and the Formation of a Coronal Flux Rope. *Astrophysical Journal*, **697**, 1529. [99](#)
- FANG, F., MANCHESTER, W., ABBETT, W.P. & VAN DER HOLST, B. (2010). Simulation of Flux Emergence from the Convection Zone to the Corona. *Astrophysical Journal*, **714**, 1649. [49](#), [113](#)
- FITT, A.D. (1996). Mixed systems of conservation laws in industrial mathematical modelling. *Surveys on Mathematics for Industry*, **6**, 21. [6](#)
- FORBES, T.G. (2000). A review on the genesis of coronal mass ejections. *Journal of Geophysical Research*, **105**, 23153. [79](#)
- FREIDBERG, J.P. (1987). *Ideal Magnetohydrodynamics*. Springer. [6](#)
- GALSGAARD, K., MORENO-INSERTIS, F., ARCHONTIS, V. & HOOD, A. (2005). A Three-dimensional Study of Reconnection, Current Sheets, and Jets Resulting from Magnetic Flux Emergence in the Sun. *Astrophysical Journal Letters*, **618**, L153. [45](#)
- GILMAN, P.A. (1970). Instability of Magnetohydrostatic Stellar Interiors from Magnetic Buoyancy. I. *Astrophysical Journal*, **162**, 1019. [7](#), [11](#)
- HARRA, L.K., MAGARA, T., HARA, H., TSUNETTA, S., OKAMOTO, T.J. & WALLACE, A.J. (2010). Response of the solar atmosphere to the emergence of ‘serpentine’ magnetic field. *Solar Physics*, **263**, 105. [105](#), [119](#)
- HOOD, A.W., ARCHONTIS, V., GALSGAARD, K. & MORENO-INSERTIS, F. (2009). The emergence of toroidal flux tubes from beneath the solar photosphere. *Astronomy & Astrophysics*, **503**, 999. [47](#), [50](#), [57](#), [118](#)

REFERENCES

- HORNIG, G. & PRIEST, E. (2003). Evolution of magnetic flux in an isolated reconnection process. *Physics of Plasmas*, **10**, 2712. [97](#)
- HUGHES, D.W. & CATTANEO, F. (1987). A new look at the instability of a stratified horizontal magnetic field. *Geophysical and Astrophysical Fluid Dynamics*, **39**, 65. [7](#), [11](#)
- JENSEN, E. (1955). On tubes of magnetic forces embedded in stellar material. *Annales d'Astrophysique*, **18**, 127. [2](#)
- KAISIG, M., TAJIMA, T., SHIBATA, K., NOZAWA, S. & MATSUMOTO, R. (1990). Nonlinear excitation of magnetic undular instability by convective motion. *Astrophysical Journal*, **358**, 698. [38](#)
- KLIEM, B. & TÖRÖK, T. (2006). Torus Instability. *Physical Review Letters*, **96**, 255002. [99](#)
- LANEY, C. (1998). *Computational Gasdynamics*. Cambridge University Press. [15](#), [26](#)
- LEAKE, J.E. & ARBER, T.D. (2006). The emergence of magnetic flux through a partially ionised solar atmosphere. *Astronomy & Astrophysics*, **450**, 805. [15](#), [40](#), [41](#), [44](#), [47](#)
- LI, Y. & LUHMANN, J. (2006). Coronal Magnetic Field Topology over Filament Channels: Implication for Coronal Mass Ejection Initiations. *Astrophysical Journal*, **648**, 732. [81](#)
- LITES, B.W., KUBO, M., BERGER, T., FRANK, Z., SHINE, R., TARBELL, T., TITLE, A., OKAMOTO, T.J. & OTSUJI, K. (2010). Emergence of Helical Flux and the Formation of an Active Region Filament Channel. *Astrophysical Journal*, **718**, 474. [118](#)
- LIU, J. & ZHANG, H. (2006). The magnetic field, horizontal motion and helicity in a fast emerging flux region which eventually forms a delta spot. *Solar Physics*, **234**, 21. [76](#)

REFERENCES

- LYNCH, B.J., ANTIOCHOS, S.K., DEVORE, C.R., LUHMANN, J.G. & ZURBUCHEN, T.H. (2008). Topological Evolution of a Fast Magnetic Breakout CME in Three Dimensions. *Astrophysical Journal*, **683**, 1192. [xi](#), [80](#), [81](#), [97](#)
- MACLEAN, R.C., PARNELL, C.E. & GALSGAARD, K. (2009). Is Null-Point Reconnection Important for Solar Flux Emergence? *Solar Physics*, **260**, 299. [96](#)
- MACNEICE, P., ANTIOCHOS, S.K., PHILLIPS, A., SPICER, D.S., DEVORE, C.R. & OLSON, K. (2004). A Numerical Study of the Breakout Model for Coronal Mass Ejection Initiation. *Astrophysical Journal*, **614**, 1028. [80](#)
- MAGARA, T. (2001). Dynamics of Emerging Flux Tubes in the Sun. *Astrophysical Journal*, **549**, 608. [38](#), [40](#), [42](#)
- MAGARA, T. & LONGCOPE, D.W. (2001). Sigmoid Structure of an Emerging Flux Tube. *Astrophysical Journal Letters*, **559**, L55. [42](#), [43](#)
- MAGARA, T. & LONGCOPE, D.W. (2003). Injection of Magnetic Energy and Magnetic Helicity into the Solar Atmosphere by an Emerging Magnetic Flux Tube. *Astrophysical Journal*, **586**, 630. [42](#), [43](#)
- MANCHESTER, W., IV (2007). Solar Atmospheric Dynamic Coupling Due to Shear Motions Driven by the Lorentz Force. *Astrophysical Journal*, **666**, 532. [118](#)
- MANCHESTER, W., IV, GOMBOSI, T., DEZEEUW, D. & FAN, Y. (2004). Eruption of a Buoyantly Emerging Magnetic Flux Rope. *Astrophysical Journal*, **610**, 588. [45](#), [49](#)
- MARTÍNEZ-SYKORA, J., HANSTEEN, V. & CARLSSON, M. (2008). Twisted Flux Tube Emergence From the Convection Zone to the Corona. *Astrophysical Journal*, **679**, 871. [48](#)
- MORENO-INSERTIS, F., GALSGAARD, K. & UGARTE-URRA, I. (2008). Jets in Coronal Holes: Hinode Observations and Three-dimensional Computer Modeling. *Astrophysical Journal Letters*, **673**, L211. [46](#)

REFERENCES

- MORTON, K.W. & MAYERS, D.F. (2005). *Numerical Solution of Partial Differential Equations*. Cambridge University Press. [18](#)
- MURRAY, M.J. (2007). *Solar Flux Emergence: A Three-Dimensional Numerical Study*. Ph.D. thesis, School of Mathematics and Statistics, University of St Andrews. [7](#)
- MURRAY, M.J. & HOOD, A.W. (2008). Emerging flux tubes from the solar interior into the atmosphere: effects of non-constant twist. *Astronomy & Astrophysics*, **479**, 567. [46](#)
- MURRAY, M.J., HOOD, A.W., MORENO-INSERTIS, F., GALSGAARD, K. & ARCHONTIS, V. (2006). 3D simulations identifying the effects of varying the twist and field strength of an emerging flux tube. *Astronomy & Astrophysics*, **460**, 909. [45](#), [48](#), [57](#), [59](#), [62](#), [69](#), [72](#), [73](#)
- NEWCOMB, W.A. (1961). Convective Instability Induced by Gravity in a Plasma with a Frozen-In Magnetic Field. *Physics of Fluids*, **4**, 391. [7](#)
- OKAMOTO, T.J., TSUNETA, S., LITES, B.W., KUBO, M., YOKOYAMA, T., BERGER, T.E., ICHIMOTO, K., KATSUKAWA, Y., NAGATA, S., SHIBATA, K., SHIMIZU, T., SHINE, R.A., SUEMATSU, Y., TARBELL, T.D. & TITLE, A.M. (2008). Emergence of a Helical Flux Rope under an Active Region Prominence. *Astrophysical Journal Letters*, **673**, L215. [105](#)
- OKAMOTO, T.J., TSUNETA, S., LITES, B.W., KUBO, M., YOKOYAMA, T., BERGER, T.E., ICHIMOTO, K., KATSUKAWA, Y., NAGATA, S., SHIBATA, K., SHIMIZU, T., SHINE, R.A., SUEMATSU, Y., TARBELL, T.D. & TITLE, A.M. (2009). Prominence Formation Associated with an Emerging Helical Flux Rope. *Astrophysical Journal*, **697**, 913. [105](#)
- PARKER, E.N. (1955). The Formation of Sunspots from the Solar Toroidal Field. *Astrophysical Journal*, **121**, 491. [2](#)
- RÜDIGER, G. & HOLLERBACH, R. (2004). *The magnetic universe: geophysical and astrophysical dynamo theory*. Wiley-VCH. [14](#)

REFERENCES

- SCHINDLER, K. (2006). *Physics of Space Plasma Activity*. Cambridge University Press. 79, 97
- SCHRIJVER, C.J. & ZWAAN, C. (2000). *Solar and Stellar Magnetic Activity*. Cambridge University Press. 1
- SHIBATA, K., TAJIMA, T., MATSUMOTO, R., HORIUCHI, T., HANAWA, T., ROSNER, R. & UCHIDA, Y. (1989a). Nonlinear Parker instability of isolated magnetic flux in a plasma. *Astrophysical Journal*, **338**, 471. 36, 37
- SHIBATA, K., TAJIMA, T., STEINOLFSON, R.S. & MATSUMOTO, R. (1989b). Two-dimensional magnetohydrodynamic model of emerging magnetic flux in the solar atmosphere. *Astrophysical Journal*, **345**, 584. 37
- SOENEN, A., ZUCCARELLO, F.P., JACOBS, C., POEDTS, S., KEPPENS, R. & VAN DER HOLST, B. (2009). Numerical simulations of homologous coronal mass ejections in the solar wind. *Astronomy & Astrophysics*, **501**, 1123. 80
- STEIN, R.F., LAGERFJÄRD, A., NORDLUND, Å. & GEORGOBIANI, D. (2010). Solar Flux Emergence Simulations. *Solar Physics*, 34. 49
- TÖRÖK, T. & KLIEM, B. (2007). Numerical simulations of fast and slow coronal mass ejections. *Astronomische Nachrichten*, **328**, 743. 99
- TORTOSA-ANDREU, A. & MORENO-INSERTIS, F. (2009). Magnetic flux emergence into the solar photosphere and chromosphere. *Astronomy & Astrophysics*, **507**, 949. 48, 49, 119
- TREFETHEN, L.N. (2000). *Spectral Methods in MATLAB*. SIAM. 14
- UGARTE-URRA, I., WARREN, H.P. & WINEBARGER, A.R. (2007). The Magnetic Topology of Coronal Mass Ejection Sources. *Astrophysical Journal*, **662**, 1293. 81
- VAN DER HOLST, B., JACOBS, C. & POEDTS, S. (2007). Simulation of a Break-out Coronal Mass Ejection in the Solar Wind. *Astrophysical Journal Letters*, **671**, L77. 80

REFERENCES

- VAN LEER, B. (1997). Towards the Ultimate Conservative Difference Scheme. *Journal of Computational Physics*, **135**, 229. [26](#)
- VRŠNAK, B. (2008). Processes and mechanisms governing the initiation and propagation of CMEs. *Annales Geophysicae*, **26**, 3089. [79](#), [98](#)
- ZHANG, Y., ZHANG, M. & ZHANG, H. (2008). On the Relationship between Flux Emergence and CME Initiation. *Solar Physics*, **250**, 75. [81](#)
- ZUCCARELLO, F.P., SOENEN, A., POEDTS, S., ZUCCARELLO, F. & JACOBS, C. (2008). Initiation of Coronal Mass Ejections by Magnetic Flux Emergence in the Framework of the Breakout Model. *Astrophysical Journal Letters*, **689**, L157. [82](#), [95](#)